MODE I, PLANE STRESS CRACK INITIATION AND GROWTH IN ELASTIC-PLASTIC SOLIDS: A FINITE ELEMENT ANALYSIS

Thesis by

Narasimhan Ramarathnam

In Partial Fulfillment of the Requirements
for the Degree of
Doctor of Philosophy

California Institute of Technology
Pasadena, California

1987

(Submitted November 7, 1986)

One should acquire the essence of higher learning to a consummate extent. After this has been accomplished, he should cherish all the values and principles that are symbolized by it.

-Thiruvalluvar (Tamil poet, First century A. D.)

To my Parents

ACKNOWLEDGEMENTS

I wish to express my sincere appreciation to my thesis advisor, Professor A. J. Rosakis, for his most valuable guidance and suggestions during the entire course of this investigation. I am also very grateful to Professor J. K. Knowles for his inestimable advice and encouragement. I am deeply indebted to Professor J. F. Hall for providing me with many helpful ideas and for stimulating discussions regarding the finite element method that was employed in this study. I am thankful to Mr. A. T. Zehnder for supplying his experimental results and for sharing his observations with me, which helped in interpreting some of the results of this numerical analysis.

This investigation was supported by the Office of Naval Research through ONR contract #N00014-85-K-0596. The computations were performed using the Supercomputer at Boeing Computer Services, Seattle. This was made possible through NSF contract #MEA-8307785. The above contracts and the facilities provided by Boeing Computer Services are gratefully acknowledged.

Finally, I wish to dedicate this thesis to my parents who, through all their endeavours, made me realize the importance and joys of higher learning. I also wish to thank all the other members of my family, particularly my sister Sasikala, for inspiring me during the course of my graduate study.

ABSTRACT

A detailed finite element analysis of crack initiation and stable crack extension is performed under Mode I plane stress, small-scale yielding conditions. A small strain, J_2 incremental plasticity theory is employed and both elastic-perfectly plastic materials and power law hardening materials are considered.

Some issues pertaining to the stationary plane stress crack problem, such as the range of dominance of the asymptotic stress and deformation fields and the amount of non-proportional loading near the crack tip are addressed. Special attention is devoted to the perfectly plastic idealization, by performing a separate singular finite element analysis, to clarify some details about the asymptotic fields near the stationary crack tip. The full-field numerical solution is used to simulate synthetic (optical) caustic patterns at different distances from the crack tip, which are compared with experimental observations and with asymptotic analytical results.

A nodal release procedure is used to simulate quasi-static crack extension. It is found that the asymptotic angular extent of the active plastic zone, surrounding the propagating crack tip, is from $\theta = 0$ to about $\theta = 45°$ for the perfectly plastic case. The near-tip angular stress distribution within the active plastic zone is in good agreement with the variation in a centered fan, as predicted by a preliminary asymptotic analysis by Rice, for the perfectly plastic case. It is also observed that the σ_{rr} stress component has a strong radial variation within the active plastic zone. The angular extent of active yielding around the moving tip increases with hardening, while its maximum radial extent ahead of the tip decreases. Clear evidence of an elastic unloading region following the active plastic zone is found, but no secondary (plastic) reloading along the crack flank has been numerically observed for any level of hardening.

The crack tip opening profile during growth is obtained for various levels of hardening. A ductile crack growth criterion is employed to investigate the nature of the J resistance curves under plane stress. Finally, the influence of hardening on the potential for stable crack growth is examined.

TABLE OF CONTENTS

TABLE OF CONTENTS (CONCLUDED)

CHAPTER I

INTRODUCTION

1.1 REVIEW OF PAST WORK

Stationary cracks under monotonic loading

In linear elastic fracture mechanics, the stress intensity factor which is a measure of the intensity of the singular stress and strain fields near the crack tip plays a central role in characterizing the onset of crack growth. However, an approach based on the stress intensity factor is limited, since most structural materials, particularly low to intermediate strength metals undergo plastic flow near the crack tip. The fact that yielding near the tip may take place over a large size scale has compelled investigators [2.8-2.10][1] to examine the continuum fields near a monotonically loaded stationary crack tip based on a plasticity theory.

The J integral [2.12] is a measure of the intensity of the near-tip fields from the small strain, deformation plasticity analyses of [2.8-2.10]. Thus, the earlier approach, based on the stress intensity factor, has been generalized in terms of the J integral for describing the onset of crack growth [2.25,2.26] under conditions that are largely unrestricted as to the extent of crack tip yielding. However, due to effects that are not modelled by a small strain deformation plasticity theory, the above approach could have serious limitations. This could be due to the presence of strong non-proportional loading and finite strain effects near the crack tip.

Several investigators who have addressed the above issues, primarily by using numerical methods, have focussed their attention on conditions of Mode I plane strain. Levy et al.[2.13], Rice and Tracey [2.2] and Tracey [2.16] investigated the

---

[1] Numbers in square brackets indicate References listed at the end of a particular chapter.

range of dominance of the singular fields of [2.8-2.10] for Mode I plane strain, by employing accurate finite element methods. While these analyses made use of a small strain, incremental plasticity theory, McMeeking [2.27] studied the above problem within the context of a finite strain theory. Shih and German [2.28] and McMeeking and Parks [2.29] have considered the dependence of specimen configuration on the dominance of the plastic singular fields. An important outcome of these studies was to provide crucial information to an experimentalist about the size requirements of specimens used in fracture toughness testing under plane strain conditions, to ensure J dominance.

As far as fracture under plane stress conditions is concerned, comparatively much less information is available in the literature regarding the above issues. A preliminary numerical investigation was conducted by Hilton and Hutchinson [2.30] under plane stress for both small- and large-scale yielding conditions, with the view of determining J or some equivalent plastic intensity factor directly from the numerical solution. Shih [2.14] applied the method of [2.30] to study combined Mode I and Mode II fracture problems under plane stress and plane strain. Both these studies employed a deformation plasticity theory and also enforced the plastic singular fields of [2.8-2.10] in a small circle near the tip, without an *a priori* knowledge of the range of validity of these fields.

Quasi-statically propagating cracks

The J integral has been applied by some investigators to analyze small amounts of quasi-static crack growth and to determine the point at which crack advance becomes unstable. The rationale for using such an approach stems from the substantial tearing resistance of most ductile materials, in the sense that appreciable increases in J are required for small amounts of crack growth. The above method is semiempirical and is limited in scope. A fundamental understanding of the asymptotic fields during quasi-static crack growth is required to deal with more extensive amounts of crack growth, by employing a near-tip fracture criterion [3.17,3.3].

The main progress in understanding the asymptotic fields at the tip of a growing crack has been limited to elastic-perfectly plastic materials and to anti-plane shear and plane strain conditions [3.19,3.3,3.4]. Rice et al.[3.3] proposed a ductile crack growth criterion, based on the attainment of a critical crack opening displacement, to examine the extent of stable crack growth under plane strain conditions. Subsequently, an experimental investigation by Hermann and Rice [3.28] has supported the validity of using such a fracture criterion.

Amazigo and Hutchinson [4.9], and more recently Castañeda [4.10], have performed asymptotic analyses for steady-state crack extension in a linear hardening solid under anti-plane shear and Mode I (and also Mode II) plane strain and plane stress. However, the use of a linear hardening law and certain complications in the perfectly plastic limit have curtailed the applicability of the results of [4.9] and [4.10]. Gao and Hwang [4.11] have conducted a preliminary investigation about the near-tip fields in a material governed by a more realistic power hardening law. They confined their attention to Mode I plane strain.

Finite element studies, simulating crack growth, have been useful in establishing the validity of the asymptotic results of such investigations as [3.3] and [3.19] for perfectly plastic materials and also in examining the influence of hardening on crack growth. Several investigators [3.10-3.15] have carried out finite element analyses for quasi-static crack growth under anti-plane shear and Mode I plane strain.

On the other hand, as far as plane stress crack growth is concerned, much less work has been performed. A preliminary investigation has been conducted by Rice [3.2], concerning the asymptotic nature of the stress and deformation fields near a growing crack tip in an elastic-perfectly plastic material under plane stress conditions. A complete asymptotic solution for this problem, however, has thus far remained elusive. A steady-state finite element analysis has been carried out by Dean [3.16] for plane stress crack growth in a linear hardening solid (including the perfectly plastic case).

1.2 MOTIVATION FOR PRESENT WORK

As the above review clearly indicates, our present knowledge of the mechanics of plane stress fracture is somewhat limited. Some important issues regarding the stationary crack problem, which were mentioned above, such as the range of dominance of the asymptotic fields and the amount of non-proportional loading near the tip, have not been examined in plane stress. This clearly warrants a detailed numerical analysis along the lines of [2.2,2.16] and [2.27-2.29] to firmly establish a conceptual understanding of plane stress fracture. The practical relevance of such an investigation, as far example to thin aircraft and spacecraft structures, provides further motivation.

In addition to the above considerations, a detailed numerical study of plane stress fracture is compelling because of the possibility of a direct comparison with optical experimental methods such as caustics. In recent years, this method has shown great promise towards applications in ductile fracture [2.17,2.22,2.23]. A knowledge of the plastic singular fields is of primary importance in facilitating a proper interpretation of the experimental data [2.23].

The issues pertaining to the quasi-static crack growth problem under plane stress are also not completely resolved. It is well known that stable crack growth can be particularly extensive in thin plates, as has been observed, for example, by Broek [3.25]. Nevertheless, the absence of an asymptotic solution in plane stress, similar to [3.19] or [3.3], has impeded a complete understanding of this important phenomenon. The numerical analysis by Dean [3.16] is not very detailed (see Chapter III), and certain issues pertaining to the near-tip fields have not been examined. This provides an impetus for a detailed numerical investigation, similar to [3.10] in plane strain, to study the asymptotic fields during plane stress crack growth.

1.3 OUTLINE OF PRESENT WORK

In this work, an elaborate finite element analysis, with a very fine mesh elucidating the details near the crack tip, is carried out to simulate Mode I plane stress, small-scale yielding conditions. Computations are performed for materials obeying a small strain, J_2 incremental plasticity theory with no hardening and an isotropic power law hardening.

In Chapter II, the analysis of a monotonically loaded stationary crack is performed. Detailed results are obtained for the plastic zones, stress and strain fields and crack opening displacements. Also, the path independence of the J integral is examined. Caustic patterns are simulated from the full-field numerical solution at a wide range of distances from the crack tip and are compared with experimental observations [2.23].

In Chapter III, the results obtained in Chapter II are used to simulate stable crack extension for an elastic-perfectly plastic material. Besides examining the extent of active yielding and the asymptotic fields, we plot stress characteristics near the tip from the finite element results, which could provide greater insight regarding the expected nature of the asymptotic solution for this problem. A ductile crack growth criterion [3.3] is used to investigate the nature of the J resistance curves under plane stress. These results corroborate experimental observations of a larger potential for stable crack growth under plane stress, as compared with plane strain.

In Chapter IV, the effect of isotropic power law hardening on the active plastic zone and near-tip fields is investigated, and comparisons are made with the results obtained in Chapter III for the perfectly plastic case. Also the influence of hardening on the potential for stable crack growth is examined.

CHAPTER II

MONOTONIC LOADING OF A STATIONARY CRACK UNDER PLANE STRESS

2.1 INTRODUCTION

The stress intensity factor is a measure of the intensity of the stress and strain fields near a crack tip in linear elastic fracture mechanics. However, fracture in most structural materials, particularly low and intermediate strength metals is often accompanied by plastic flow near the crack tip, invalidating the assumptions of linear elasticity theory. Under certain circumstances, the stress intensity factor can still be used to characterize the onset of crack growth, provided that the plastic zone is contained well within the region of dominance of the singular elastic field. This situation is often referred to as "small-scale yielding." But when plastic flow takes place over large size scales, one is compelled to seek continuum solutions for crack problems within the context of an elastic-plastic theory.

Hutchinson [2.8,2.9] and Rice and Rosengren [2.10] performed the asymptotic analysis for stress and deformation fields near a monotonically loaded stationary crack tip in a power law hardening material obeying a deformation plasticity theory. The fact that the value of the J integral [2.12] provides a measure of the intensity of the near-tip field in this asymptotic solution has prompted some investigators [2.25,2.26] to propose a criterion for the onset of crack growth based on the attainment of a critical value for J. This proposal has been complemented by a wide range of experimental data [2.25,2.26].

In order to characterize fracture initiation based on this single macroscopic parameter, it is imperative that the plastic singular fields of [2.8-2.10] should dominate over a length scale that is large as compared to the fracture process zone. In this region, microstructural processes such as void nucleation and growth, microcracking, etc. take place. The fracture process zone is often believed to coincide with the region near the tip, wherein finite strain effects are significant. In addition to the above issues, another important factor that has to be considered is the possibility of non-proportional loading near the tip, which would render the deformation plasticity theory (on which the analysis of [2.8-2.10] is based) to be physically inappropriate.

The above issues have been examined by several investigators through numerical methods predominantly under the tensile plane strain mode of fracture. Accurate finite element studies with crack tip elements making use of special interpolation functions to account for the plastic strain singularity of [2.8-2.10] were conducted by Levy et al.[2.13] and Rice and Tracey [2.2] for the perfectly plastic case and by Tracey [2.16] for hardening materials. These studies modelled Mode I plane strain, small-scale yielding conditions and employed an incremental plasticity theory. They confirmed the validity of the dominant fields of [2.8-2.10] in a region quite close to the crack tip. McMeeking [2.27] performed a finite element calculation to model crack tip blunting based on a finite strain incremental plasticity theory under plane strain, small-scale yielding conditions. He observed that finite strain effects become important only for distances from the tip of the order of 2 or 3 times the crack opening displacement δ_t (which will be defined in Sec.(2.4)). Strong path dependence of the J integral was also noticed within this region.

Shih and German [2.28] investigated the range of dominance of the plastic singular fields of [2.8-2.10] for a wide variety of specimen configurations and material properties from contained yielding to fully plastic conditions. They employed a small strain incremental plasticity theory and confined their attention to Mode I plane strain. McMeeking and Parks [2.29] also investigated configuration dependence within the context of a finite strain theory similar to [2.27] under large scale yielding. Thus, substantial work under Mode I plane strain conditions has been performed to provide a better understanding of the mechanics of crack tip state and also to specify size requirements for specimens used in fracture toughness testing to ensure J dominance.

However, very little information is available in the literature pertaining to the above issues under Mode I plane stress, despite its practical importance to structural problems. A preliminary numerical investigation was carried out by Hilton and Hutchinson [2.30] under plane stress, small- (and large-) scale yielding conditions in which the singular fields of [2.8-2.10] were imposed in a small circle near the crack tip. The value of J or some other equivalent plastic intensity factor was determined along with the nodal displacements from the finite element solution. Shih [2.14] applied the method of [2.30] to study combined Mode I and Mode II fracture problems under both plane strain and plane stress. Both these studies [2.30,2.14] employed a deformation plasticity theory and considered power-hardening materials. Also, the validity of the asymptotic solution of [2.8-2.10] was assumed over a length scale, which was not known apriori, although this was contained well within the plastic zone in these numerical simulations.

Some of the issues mentioned above, pertaining to the range of dominance of the asymptotic fields and the amount of non-proportional loading near the tip, which have received considerable attention in the plane strain problem, have not been examined in plane stress. Thus, detailed numerical work along the lines of [2.2,2.16] and [2.27-2.29] is required to firmly establish a conceptual understanding of fracture under plane stress conditions. This is usually more complex than in plane strain, primarily because the equations of plane stress plasticity are somewhat more involved [2.11].

In addition to the above considerations, a detailed numerical study of plane stress fracture is important because of the possibility of a direct comparison with optical experimental methods such as caustics. This method, which has been employed to determine the stress intensity factor in linear elastic fracture problems [2.20], has recently been extended to applications in ductile fracture [2.17,2.22]. A knowledge of the range of dominance of the plastic singular fields is of primary importance to facilitate a proper interpretation of experimental data [2.23]. Also, information from full-field numerical solutions would be crucial in analysing the caustics obtained in regions outside the range of dominance of any particular asymptotic field.

In this work, an elaborate finite element investigation, with a very fine mesh elucidating the details near the crack tip, is undertaken to simulate Mode I plane stress, small-scale yielding conditions. No attempt has been made in this part of the work to incorporate the expected singularity in the strains by using special crack tip elements. Computations have been performed for materials obeying an incremental plasticity theory with no hardening and with a power-law hardening. In Sec.(2.2), the numerical formulation, the finite element scheme, etc. is outlined. In Sec.(2.3), stationary crack tip fields under plane stress [2.8-2.10] are reviewed. In Sec.(2.4), detailed results are presented for the plastic zones, stress and strain distributions, and crack opening displacement. Also, the path independence of the J integral is examined.

In Sec.(2.5), caustic patterns are simulated from the numerical solution at a wide range of distances from the crack tip and are compared with experimental observations [2.23] and asymptotic results [2.17,2.21]. In Sec.(2.6), an additional numerical analysis, employing singular elements near the crack tip, is performed for the perfectly plastic case in order to examine the asymptotic stress and deformation fields. The issue of sensitivity of the numerical results to the near-tip mesh design is thus investigated. It is found that the dominant strain field near the tip for perfect plasticity is completely different from the limit of the singular solution of [2.8-2.10] for materials with low hardening. On the other hand, the numerical results for the near-tip stress field are in good agreement with the slip line solution of Hutchinson [2.9]. In the light of this observation, it is suggested that the configuration dependence of crack tip deformation should be investigated under plane stress in the spirit of [2.27-2.29]. Such an analysis could be complemented by experimental results based on caustics.

2.2 NUMERICAL ANALYSIS

Formulation

The Mode I plane stress, small-scale yielding problem [2.1] was modelled by considering a crack in a domain R, which was entirely represented by finite elements as shown in Figs. 2.1*a* and *b*. Only the upper half-plane was considered because of Mode I symmetry. All field quantities are referred to with respect to an orthonormal frame $\{\underset{\sim}{e}_1, \underset{\sim}{e}_2, \underset{\sim}{e}_3\}$ centered at the crack tip. The leading term in the displacements of the linear elastic asymptotic solution,

$$u_\alpha = K_I \sqrt{\frac{r}{2\pi}} \hat{u}_\alpha(\theta) , \tag{2.2.1}$$

was specified as boundary conditions on the outermost boundary S of the domain.[1] The loading was applied through the Mode I stress intensity factor K_I, which occurs as an amplitude factor in Eqn.(2.2.1).

The maximum extent of the plastic zone surrounding the crack tip was at all times within $\frac{1}{30}$ of the radius of the outermost contour S, so that the small-scale yielding condition was preserved. All plastic deformation was confined within the

---

[1] Throughout this chapter, Greek subscripts will have the range 1,2, while Latin subscripts will take values 1,2,3.

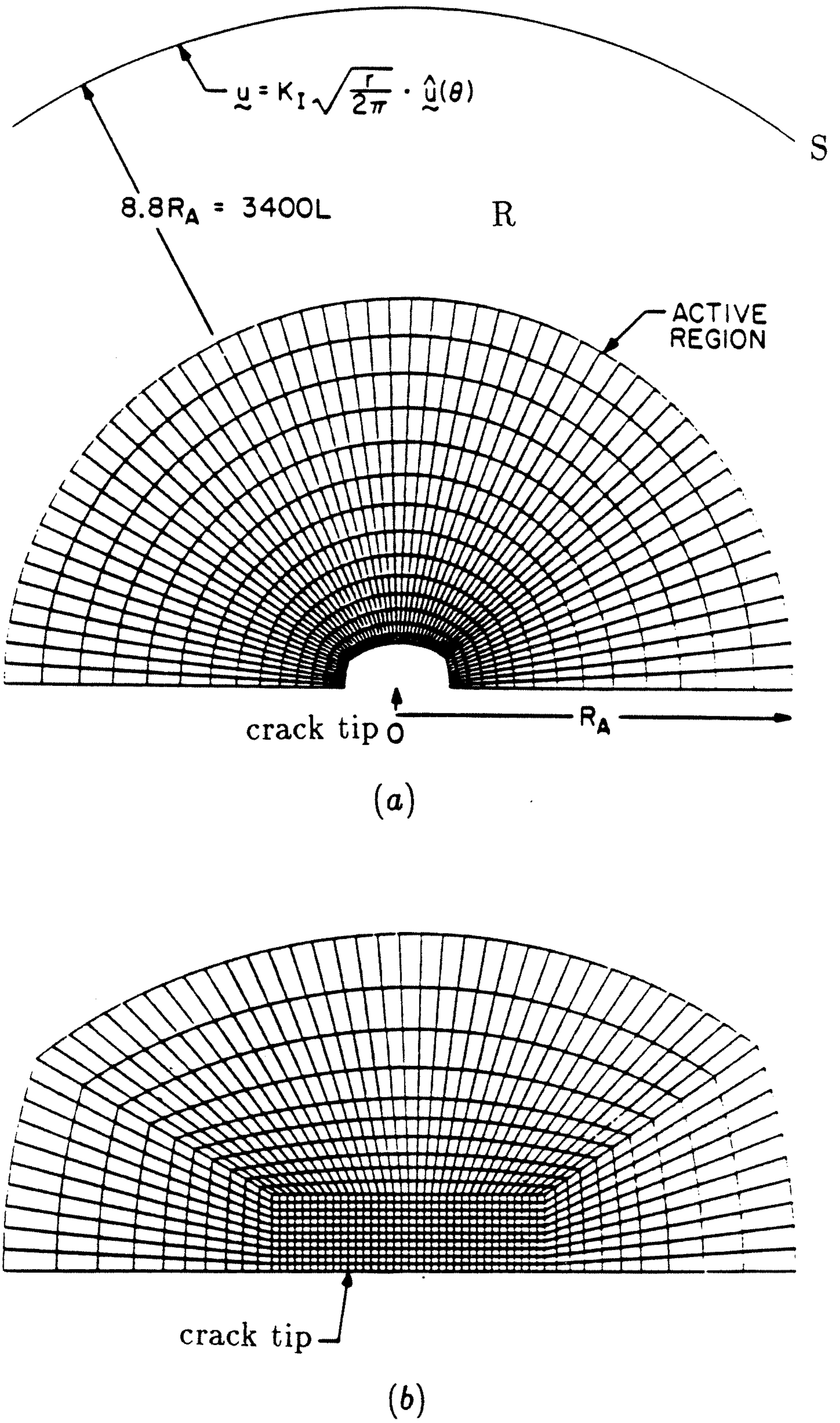

Figure 2.1. *Finite element mesh: a) Outer mesh b) Fine mesh near the crack tip.*

active region shown in Fig. 2.1*a*, which has a total of 1704 four-noded elements and 3549 degrees of freedom. The large region surrounding this active mesh has a total of 40 rings with 56 elements in each ring and remained elastic throughout the entire computation. The constant stiffness of this region was statically condensed using a ring-by-ring static condensation procedure that involved a partial forward Gauss reduction at each stage.

The cutout in Fig. 2.1*a* is a fine mesh region near the crack tip, which is shown in detail in Fig. 2.1*b*. This mesh was designed to have small rectangular elements parallel to the crack plane instead of being focussed at the crack tip. No attempt has been made to incorporate the singularity of the plastic strains by using special crack tip elements in this analysis (see Sec.(2.6) and Rice and Tracey [2.2]). This was because the stress and strain fields at the end of the stationary load history were used as initial conditions for simulating stable crack extension, which will be reported in Chapters IIIand IV. The radius R_A of the active mesh and the radius of the outermost boundary S are about 385 times and 3400 times the size L of the smallest element near the crack tip, respectively.

The Mode I symmetry conditions that are given by

$$\left.\begin{aligned} \sigma_{12}(x_1, x_2 = 0) = 0 \\ u_2(x_1, x_2 = 0) = 0 \end{aligned}\right\}, \qquad x_1 \geq 0\,, \tag{2.2.2}$$

were imposed by attaching stiff springs in the x_2 direction to the nodes ahead of the crack tip. Traction-free conditions were imposed on the crackflank.

The type of element used was the four noded isoparametric quadrilateral, which was formed from four constant strain triangles with static condensation of the internal node. This element was suggested by Nagtegaal et al.[2.3] to relieve artificial mesh-locking effects that occur under nearly incompressible conditions in plane strain. However, this problem does not arise in plane stress because there is a non-zero out-of-plane strain component ϵ_{33}, which is determined in terms of the in-plane strain components $\epsilon_{\alpha\beta}$.

Material Idealization

The materials that were numerically modelled were the elastic-perfectly plastic solids and isotropic power-hardening solids. A small strain incremental plasticity theory was employed along with the Huber-Von Mises yield condition and the associated flow rule. The Huber-Von Mises yield condition for isotropic hardening takes the form,

$$\mathrm{f}(\underline{\sigma}, \bar{\epsilon}^{\mathrm{p}}) = \mathrm{F}(\underline{\sigma}) - \bar{\sigma}^2(\bar{\epsilon}^{\mathrm{p}})\,, \tag{2.2.3}$$

where $\mathrm{F}(\underline{\sigma}) = \frac{3}{2}\underline{\mathrm{S}}\,.\,\underline{\mathrm{S}}$ and $\bar{\epsilon}^p = \int \left(\frac{2}{3}\dot{\epsilon}^p_{ij}\dot{\epsilon}^p_{ij}\right)^{1/2} dt$ is the accumulated equivalent plastic strain. In the above, $\underline{\mathrm{S}}$ is the deviatoric stress tensor and $\bar{\sigma}(\bar{\epsilon}^{\mathrm{p}})$ is defined by the following power hardening rule:

$$\frac{\bar{\epsilon}^p}{\epsilon_0} = \left(\frac{\bar{\sigma}}{\sigma_0}\right)^n - \frac{\bar{\sigma}}{\sigma_0}\,. \tag{2.2.4}$$

For the elastic-perfectly plastic case, $\bar{\sigma}$ takes the constant value of σ_0, the yield stress in uniaxial tension. In Eqn.(2.2.4), ϵ_0 is the yield strain in uniaxial tension.

Within the context of the small strain flow theory of plasticity, the total strain rate tensor can be decomposed into elastic and plastic parts:

$$\dot{\underline{\epsilon}} = \dot{\underline{\epsilon}}^{\mathrm{e}} + \dot{\underline{\epsilon}}^{\mathrm{p}}. \tag{2.2.5}$$

The stress rate tensor $\dot{\underline{\sigma}}$ is related to the elastic strain rate tensor $\dot{\underline{\epsilon}}^{\mathrm{e}}$ through a constant, isotropic, positive definite elasticity tensor $\underline{\mathrm{C}}$ as,

$$\dot{\underline{\sigma}} = \underline{\mathrm{C}}\,\dot{\underline{\epsilon}}^{\mathrm{e}}\,. \tag{2.2.6}$$

The plastic strain rate tensor $\dot{\underline{\epsilon}}^{\mathrm{p}}$ is normal to the yield surface and the flow rule takes the form,

$$\dot{\underline{\epsilon}}^{\mathrm{p}} = \frac{\dot{\lambda}}{3}\mathrm{F}_{\underline{\sigma}} = \dot{\lambda}\underline{\mathrm{S}}\,, \tag{2.2.7}$$

where $\dot{\lambda} \geq 0$.

By using Eqns.(2.2.3)-(2.2.7) the constitutive law for material currently experiencing elastic-plastic deformation can be obtained as,

$$\dot{\sigma}_{ij} = C^{*}_{ijkl}\dot{\epsilon}_{kl} = \left[C_{ijkl} - \frac{C_{ijpq}S_{pq}S_{mn}C_{mnkl}}{S_{rt}C_{rtuv}S_{uv} + \frac{4}{9}\bar{\sigma}^{2}H} \right] \dot{\epsilon}_{kl} \ . \tag{2.2.8}$$

In the above, $H = \frac{d\bar{\sigma}}{d\bar{\epsilon}^{p}}$ and can be obtained from (2.2.4) for hardening solids and is set equal to zero for perfect plasticity.

In the present analysis, (2.2.3) and (2.2.8) were used along with the plane stress constraint, which requires

$$\sigma_{3i} \equiv 0 \ . \tag{2.2.9}$$

By using (2.2.9) in (2.2.8), we can obtain an expression for $\dot{\epsilon}_{33}$ in terms of $\dot{\epsilon}_{\alpha\beta}$.

Finite Element Scheme

A displacement based finite element method was employed in the analysis. The finite element equations were derived from the principle of virtual work. At a time (t + Δt) this takes the form,

$$\int_{\mathrm{R}} \underline{\sigma}(\mathrm{t}+\Delta\mathrm{t}) \,.\, \delta\underline{\epsilon}\mathrm{dA} = \int_{\partial\mathrm{R}} \underline{\mathrm{T}}(\mathrm{t}+\Delta\mathrm{t}) \,.\, \delta\underline{\mathrm{u}}\mathrm{ds} \ . \tag{2.2.10}$$

Here $\underline{\sigma}(\mathrm{t}+\Delta\mathrm{t})$ represents the Cauchy stress tensor, which satisfies equilibrium at time (t + Δt) and $\underline{\mathrm{T}}(\mathrm{t}+\Delta\mathrm{t})$ the imposed traction vector on the boundary ∂R. Also, $\delta\underline{\mathrm{u}}$ represents the virtual displacement vector that vanishes on the part of the boundary where the displacements are specified and $\delta\underline{\epsilon}$ is the associated small strain tensor.

After linearizing about the equilibrium configuration at time t and introducing the finite element approximation, we obtain the following incremental equilibrium equations in matrix form (Bathe et al.[2.4]):

$$\underline{\mathrm{K}}_{\mathrm{T}}\Delta\underline{\mathrm{U}} = \underline{\mathrm{F}}(\mathrm{t}+\Delta\mathrm{t}) - \underline{\mathrm{P}}(\mathrm{t}) \ . \tag{2.2.11}$$

Here $\Delta \underline{U} = \underline{U}(t+\Delta t) - \underline{U}(t)$ is the vector of nodal point displacement increments. Also, $\underline{K}_T = \int_R \underline{B}^T \underline{D}\,\underline{B} dA$ is the tangent stiffness matrix corresponding to the configuration at time t, $\underline{B}$, the strain displacement matrix ($\underline{\epsilon} = \underline{B}\,\underline{U}$) and $\underline{D}$, the material constitutive matrix. $\underline{D}$ will be equal to $\underline{C}$ for purely elastic response and $\underline{C}^*$ for elastic-plastic material response. $\underline{F}(t+\Delta t)$ is the vector of externally applied nodal point loads at time $(t+\Delta t)$ and $\underline{P}(t) = \int_R \underline{B}^T \underline{\sigma}(t) dA$ is the vector of nodal point forces equivalent to the element stresses at time t.

In the present analysis, time is only a convenient variable that represents different levels of load intensities. An iterative Newton-Raphson procedure [2.4-2.6] was employed in the solution of the incremental equilibrium equations (2.2.11). This method is summarized in Appendix A.

Stress Computation

As was observed above, the finite element scheme solves the displacement equations of equilibrium in an incremental fashion. Hence, the constitutive laws presented earlier that deal with stress and strain rates were used approximately to relate small finite increments in stresses and strains. An explicit integration procedure also known as the Tangential Predictor-Radial Return method was employed to integrate the incremental stress-strain law. As shown by Schreyer et al.[2.7], this method, if used with subincrementation (as in the present analysis), is very accurate for plane stress conditions.

It is important to recall that the requirement of plane stress imposes a constraint for the out-of-plane strain increment $\Delta\epsilon_{33}$ in terms of the in-plane strain increments $\Delta\epsilon_{\alpha\beta}$. Due to this constraint, it is more convenient to perform computations with stress and strain tensors instead of with their deviatoric parts as is normally done in plane strain. The method of stress computation is outlined in Appendix A.

Solution Strategy

As noted earlier, the loading was applied through the Mode I stress intensity factor K_I, which enters the far-field displacement boundary condition (2.2.1). An initial load step was performed in which K_I was small enough to ensure that all the elements remained elastic. K_I was then scaled to cause incipient yielding in the element nearest to the crack tip.

Subsequent load steps were performed by increasing K_I by 5-10% of the incipient value at a time and iterating for convergence to equilibrium. Each load step required typically 3-4 iterations before converging to an accepted equilibrium configuration. Yielding was continued till the plastic zone surrounding the crack tip had a maximum extent of about 50 or 100 times the smallest element size L in order to guarantee sufficient resolution near the crack tip.

2.3 STATIONARY CRACK TIP FIELDS

Power-Hardening Solids

Hutchinson [2.8,2.9] and Rice and Rosengren [2.10] investigated the asymptotic stress and strain fields near a monotonically loaded stationary crack tip in an elastic-plastic solid. The dominant singular term of their analysis will be referred to as HRR in the sequel. In their work, a J_2 deformation plasticity theory and a power-law hardening idealization similar to (2.2.4) were assumed.

The HRR analysis employs a small strain formulation and assumes a separable form in polar coordinates r and θ, for the dominant term of the solution, to obtain,

$$\left.\begin{aligned} \sigma_{ij} &\sim \sigma_0 \left[\frac{J}{\sigma_0 \epsilon_0 I_n r}\right]^{\frac{1}{n+1}} \tilde{\sigma}_{ij}(\theta, n) \\ \epsilon^p_{ij} &\sim \epsilon_0 \left[\frac{J}{\sigma_0 \epsilon_0 I_n r}\right]^{\frac{n}{n+1}} \tilde{\epsilon}^p_{ij}(\theta, n) \end{aligned}\right\}, \qquad r \to 0 . \tag{2.3.1}$$

In (2.3.1), σ_0 and ϵ_0 are the yield stress and strain in uniaxial tension and n is the hardening exponent. The angular factors $\tilde{\sigma}_{ij}(\theta,n)$ and $\tilde{\epsilon}^p_{ij}(\theta,n)$ depend on the mode of loading and on the hardening exponent. The dimensionless quantity I_n, which is defined in [2.8], decreases from 5 for n = 1 to about 2.6 for $n \to \infty$ under plane stress. J in (2.3.1) is the value of Rice's [2.12] J integral.

For plane deformations, the J integral is defined for any path of integration Γ by [2.12],

$$J = \int_{\Gamma} (W\nu_1 - \nu_i\sigma_{ij}u_{j,1})ds \, , \tag{2.3.2}$$

where W is the local stress work density, ν_i a unit vector normal to Γ and u_i is a particle displacement vector. For our purposes, Γ will denote an open contour surrounding the crack tip. The integral (2.3.2) has the well-known property of path independence for a wide class of solids, including materials that obey the deformation theory of plasticity. Under small-scale yielding conditions, J can be evaluvated from contours taken in the far-field (K dominated) elastic region as,

$$J = \frac{K_I^2}{E} \tag{2.3.3}$$

for plane stress. It is important to note that J enters (2.3.1) as an amplitude factor and hence provides a unique measure for characterizing fracture initiation at the crack tip.

The main limitation of the HRR analysis is the unknown range of dominance (e.g., with respect to maximum extent of the plastic zone) of the singular solution. This issue is important since this range of dominance should be large as compared with the fracture process zone and the region near the crack tip where the small strain plasticity theory breaks down. From the experimental standpoint, this information is crucial in the proper interpretation of experimental data based on optical measurements [2.17,2.23].

Also, the discrepancy between the deformation theory and the more appropriate incremental theory of plasticity has to be assessed from the context of crack tip fields. In addition, another serious limitation that will be pointed out later occurs when the limit n → ∞ is taken. This is associated with the change in nature of the governing equations in the limit as the perfect plasticity case is approached.

The above issues will be investigated from the point of view of the plane stress full-field numerical solution presented here. This solution simulates small-scale yielding conditions and employs an incremental plasticity theory.

Perfectly Plastic Solids: Stress Field

For perfectly plastic solids, the following important assumptions regarding the asymptotic nature of the stress field are usually made,

$$\left.\begin{aligned} \sigma_{ij}(r,\theta) &\sim \sigma^{\circ}_{ij}(\theta) \\ \frac{\partial \sigma_{ij}(r,\theta)}{\partial \theta} &\sim \sigma'_{ij}(\theta) = \frac{d\sigma^{\circ}_{ij}}{d\theta} \\ r\frac{\partial \sigma_{ij}}{\partial r} &\sim o(1) \end{aligned}\right\}, \qquad r \to 0\,. \tag{2.3.4}$$

It is important to bear in mind that the field equations for perfect plasticity are hyperbolic [2], while those for hardening solids are elliptic.

Equation (2.3.4) can be used to obtain asymptotic forms of equilibrium equations and the Von Mises yield condition (Rice and Tracey [2.2]). These can be employed to show that only two types of asymptotic plastic sectors can exist near the crack tip. These are as follows for plane stress.

i) Centered Fan Sector

In this sector, radial lines are stress characteristics and the asymptotic stress field has the following form,

$$\left.\begin{aligned} \sigma^{\circ}_{rr}(\theta) &= \tau_0\cos(\theta-\theta_0) \\ \sigma^{\circ}_{\theta\theta}(\theta) &= 2\tau_0\cos(\theta-\theta_0) \\ \sigma^{\circ}_{r\theta}(\theta) &= \tau_0\sin(\theta-\theta_0) \end{aligned}\right\}, \tag{2.3.5}$$

---

[2] For perfectly plastic solids *under plane stress*, the governing equations for the stresses could be hyperbolic, parabolic or elliptic [2.11].

where θ_0 is an arbitrary constant angle and τ_0 is the yield stress in pure shear.

ii) Constant Stress Sector

In this sector, the Cartesian components of the stresses are constant,

$$\overset{\circ}{\sigma}_{\alpha\beta}(\theta) = b_{\alpha\beta} \ . \tag{2.3.6}$$

The constants $b_{\alpha\beta}$ are related by the yield condition. Straight lines along which the direct components of the stress deviator $\overset{\circ}{S}_{\alpha\beta}$ vanish are stress characteristics (Hill [2.11]).

Hutchinson [2.9] assembled a solution for the near-tip field comprising of a combination of the above sectors as shown in Fig. 2.2. The region marked A is a centered fan sector extending from $\theta = 0°$ to $\theta = 79.7°$, while the regions B and C are two constant stress sectors, which occupy the angles from $\theta = 79.7°$ to $\theta = 180°$. The stresses in Sector A are as given by (2.3.5) with $\theta_0 = 0$. In particular, it should be noted that the stresses ahead of the crack tip ($\theta = 0$) are given by

$$\overset{\circ}{\sigma}_{11} = \tau_0 \qquad \overset{\circ}{\sigma}_{22} = 2\tau_0 \qquad \overset{\circ}{\sigma}_{12} = 0 \ . \tag{2.3.7}$$

There is also a discontinuity in the σ_{rr} stress component between the two constant stress sectors B and C, which is admissible as long as the crack remains stationary.

Perfectly Plastic Solids: Deformation fields

As noted by Rice [2.12] in the case of plane strain, singularities in strains result when slip lines focus at a point as in centered fan sectors. The displacements u_i (or the rates $\dot{u}_i$ in a proper incremental formulation [2.11]) are functions of angle θ as the crack tip is approached within centered fan sectors resulting in a discrete crack opening displacement at the tip. The following assumptions are often made [2.2]

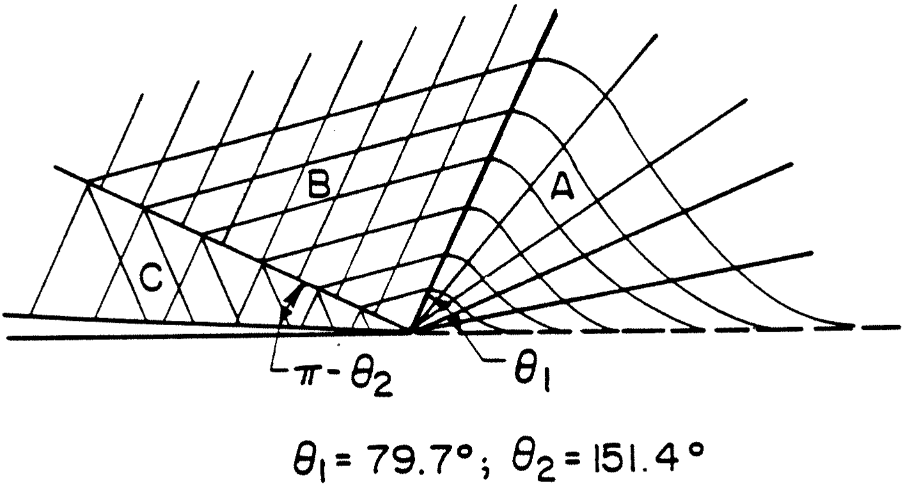

Figure 2.2. *Analytical asymptotic field near a stationary crack tip in a perfectly plastic solid under plane stress represented by stress characteristics.*

about the displacements u_i (or the rates $\dot{u}_i$) within centered fan sectors,

$$\left.\begin{aligned} u_i(r,\theta) &\sim u_i^\circ(\theta) \\ \frac{\partial u_i(r,\theta)}{\partial\theta} &\sim u_i'(\theta) = \frac{du_i^\circ}{d\theta} \\ r\frac{\partial u_i}{\partial r} &\sim o(1) \end{aligned}\right\}, \qquad r \to 0\,. \tag{2.3.8}$$

Since radial lines are stress characteristics in the fan, ϵ^p_{rr} is nonsingular while $\epsilon^p_{\theta\theta}$ (or $\dot{\epsilon}^p_{\theta\theta}$) and $\epsilon^p_{r\theta}$ (or $\dot{\epsilon}^p_{r\theta}$) are singular as $O(\frac{1}{r})$ when the crack tip is approached within the fan. Thus, it is possible to write

$$\left.\begin{aligned} \epsilon^p_{\theta\theta} &\sim \epsilon_0\frac{\hat{\epsilon}^p_{\theta\theta}(\theta)}{r} \\ \epsilon^p_{r\theta} &\sim \epsilon_0\frac{\hat{\epsilon}^p_{r\theta}(\theta)}{r} \end{aligned}\right\}, \qquad r \to 0 \tag{2.3.9}$$

within fan sectors. The angular factors $\hat{\epsilon}^p_{\theta\theta}(\theta)$ and $\hat{\epsilon}^p_{r\theta}(\theta)$ are *non unique* and cannot be determined from a local analysis. They depend on a solution to the entire boundary value problem. However, from the flow rule ,

$$\dot{\epsilon}^p_{ij} = \left(\frac{\dot{\epsilon}^p_{kl}\dot{\epsilon}^p_{kl}}{2}\right)^{\frac{1}{2}}\frac{S_{ij}}{\tau_0}\,, \tag{2.3.10}$$

the following relation can be obtained between $\dot{\epsilon}^p_{\theta\theta}$ and $\dot{\epsilon}^p_{r\theta}$,

$$\dot{\epsilon}^p_{r\theta} = \dot{\epsilon}^p_{\theta\theta}\frac{S_{r\theta}}{S_{\theta\theta}}\,, \tag{2.3.11}$$

provided $S_{\theta\theta} \neq 0$. Although this equation strictly applies for the strain rates in an incremental theory, it can be used to relate the total strains if the stresses remained constant at a material point from the time it was enveloped by the plastic zone. Hence, it is expected to hold approximately between the asymptotic angular strain factors $\hat{\epsilon}^p_{\theta\theta}(\theta)$ and $\hat{\epsilon}^p_{r\theta}(\theta)$.

The dominant HRR solution for the stresses (2.3.1) approaches the limiting slipline distribution of perfect plasticity as the hardening exponent $n \to \infty$. But as has been observed by Levy et al.[2.13] and Rice and Tracey [2.2] for plane strain, one cannot in general expect the HRR singular solution for the strains as n → ∞ to be the dominant solution for perfect plasticity because of the non-uniqueness noted earlier.

On the other hand, the strain components are (in general) non-singular in the constant stress sectors and the same displacement results if the crack tip is approached along different radial lines in these sectors.

An expression for the near-tip J integral can be obtained from the asymptotic form (2.3.9) following Rice's [2.12] plane strain analysis. Taking the contour Γ in (2.3.2) to be a circle of radius r, one can write (2.3.2) as,

$$J = r\int_{-\pi}^{\pi}\Big\{W\cos\theta - \sigma_{rr}\big[\epsilon_{rr}\cos\theta - (\epsilon_{r\theta}-\omega)\sin\theta\big] - \sigma_{r\theta}\big[(\epsilon_{r\theta}+\omega)\cos\theta - \epsilon_{\theta\theta}\sin\theta\big]\Big\}d\theta\ . \tag{2.3.12}$$

In the above equation, ω is the rotation, and

$$\omega = -\epsilon_{r\theta} + o\left(\frac{1}{r}\right), \qquad r\to 0\ . \tag{2.3.13}$$

Also,

$$\left.\begin{aligned} \epsilon_{rr} &= o\left(\frac{1}{r}\right) \\ W &= W^p + o\left(\frac{1}{r}\right) \end{aligned}\right\}, \qquad r\to 0\ , \tag{2.3.14}$$

where

$$W^p = \int_0^{\bar\epsilon^p}\bar\sigma\, d\bar\epsilon^p = \sigma_0\bar\epsilon^p \approx \sigma_0\left(\frac{2}{3}\epsilon^p_{ij}\epsilon^p_{ij}\right)^{1/2}\ .$$

Taking r → 0 in (2.3.12) and using the asymptotic equations (2.3.5), (2.3.9), (2.3.13) and (2.3.14), one obtains

$$J_{tip} = \left(\frac{2\sigma_0^2}{\sqrt{3}E}\right)\int_0^{\theta^*}\Big\{2\big[(\hat\epsilon^p_{r\theta})^2 + (\hat\epsilon^p_{\theta\theta})^2\big]^{1/2}\cos\theta + \hat\epsilon^p_{r\theta}\sin 2\theta + \hat\epsilon^p_{\theta\theta}\sin^2\theta\Big\}d\theta\ , \tag{2.3.15}$$

where θ^* is the maximum angular extent of the fan.

2.4 RESULTS AND DISCUSSION

The computations were performed for two levels of power hardening, $n = 5$ and 9 and also for the elastic-perfectly plastic case, which is referred to as $n = \infty$ in the following discussion of the results. It should, however, be noted that the elastic-perfectly plastic calculation was performed with $H = \frac{d\bar{\sigma}}{d\bar{\epsilon}^p} \equiv 0$ in the constitutive Equation (2.2.8). The ratio of the Young's modulus to the yield stress in pure shear (E/τ_0) was taken as 1400 for the two cases of power hardening and as 350 for the elastic-perfectly plastic calculation. The Poisson's ratio was taken as 0.3 for all cases.

Plastic Zones

The plastic zone surrounding the crack tip is shown in Fig. 2.3 for the three values of hardening exponent n. The crack tip is situated at the origin of the coordinate axes that have been made dimensionless by the parameter $(K_I/\sigma_0)^2$. This parameter has the unit of length and also contains a measure of the far-field loading. Hence, the size of the plastic zone is expected to scale with respect to this parameter under small-scale yielding conditions. A point in the figure represents a yielded integration station within an element. It should be noted that the plastic zone becomes less rounded and spreads more ahead of the crack tip with decreasing hardening (increasing n).

These plastic zones agree well in shape but are slightly smaller in size as compared with the results of Shih [2.14], who employed a deformation plasticity theory and used a singular element near the crack tip. The maximum extent of the plastic zone that occurs ahead of the crack tip ($\theta = 0$) is about $r_p = 0.22(K_I/\sigma_0)^2$, $0.25(K_I/\sigma_0)^2$ and $0.29(K_I/\sigma_0)^2$ for $n = 5$, 9 and ∞, respectively. For comparison, Shih's [2.14] calculation indicates an r_p of about $0.32(K_I/\sigma_0)^2$ for $n = 25$, and Tada et al.[2.15] report $r_p = \frac{1}{\pi}(K_I/\sigma_0)^2$ for $n = \infty$

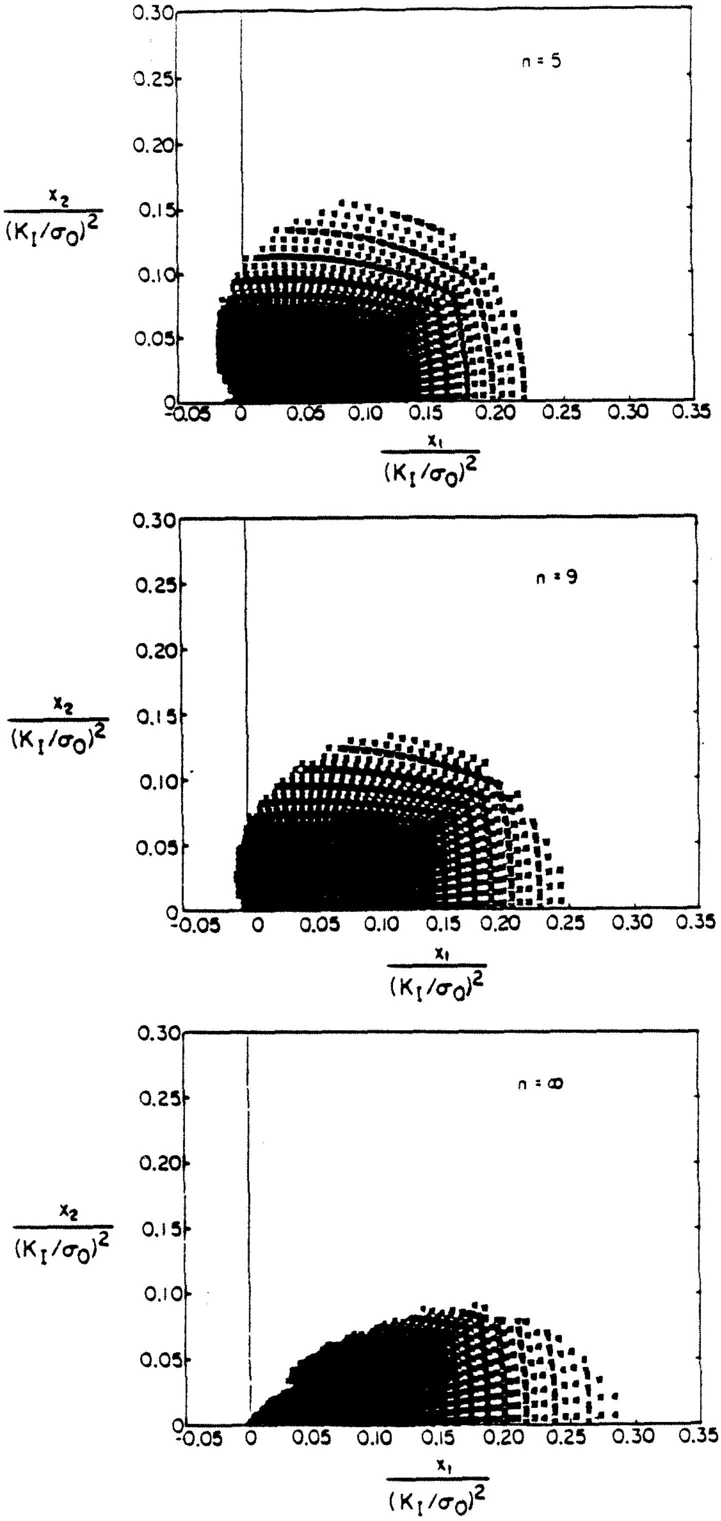

Figure 2.3. *Plastic zones surrounding the crack tip for three levels of hardening: n=5,9 and ∞.*

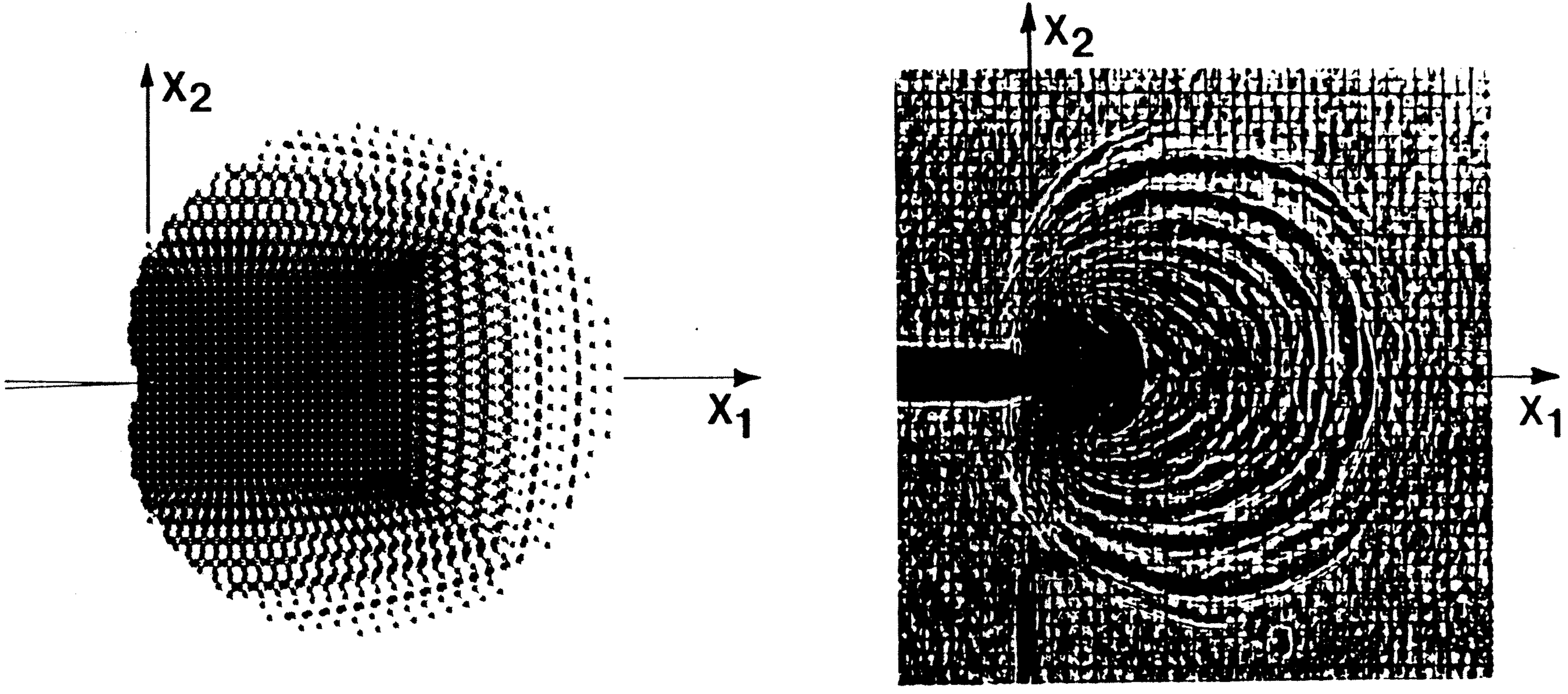

(*a*) (*b*)

Figure 2.4. *Comparison of a) numerical with b) experimental plastic zones for material with* n = 9.

based on an approximate calculation. The slightly larger size of the plastic zone obtained by Shih could be due to the imposition of the HRR singular solution in a small circle around the crack tip in his analysis. The present computation introduces no such *a priori* constraint.

In Fig. 2.4 the numerically obtained plastic zone for $n = 9$ is compared with the visual evidence of permanent plastic deformation observed on the surface of a thin compact tension specimen [2.23]. The material used in this experiment was a 4340 carbon steel with a power-hardening exponent of 9 in uniaxial tension. The experimental and numerical plastic zones agree well in shape and also in size when the load levels in the experiment were small and there were no boundary interaction effects (contained yielding).

Radial Distribution of Stresses

The distribution of the normalized opening stress, σ_{22}/τ_0, along the x_1 axis ahead of the crack tip and within the plastic zone is shown in Fig. 2.5. The centroidal values of stress in the row of elements ahead of the the crack tip have been used in making this plot. Advantage has again been taken of the self-similarity noted earlier, with the distance from the crack tip being measured in terms of the dimensionless variable $x_1/(K_I/\sigma_0)^2$. The finite element results agree to within 1% with the HRR asymptotic stress distribution (2.3.1), which is shown by the solid lines in the figure, in the range $0 < x_1 < 0.08(K_I/\sigma_0)^2$. For example, at $x_1 = 0.018(K_I/\sigma_0)^2$, the ratio of the finite element to the HRR asymptotic stress is 3.13/3.14, 2.66/2.67 and 1.999/2.0 for $n = 5, 9$ and ∞, respectively.

The values given by the HRR distribution for σ_{22} are higher than their finite element counterparts by about 8% at the elastic-plastic boundary. This is in marked contrast to the corresponding result in plane strain [2.16], where strong deviation of the finite element solution from the HRR distribution was reported even for small

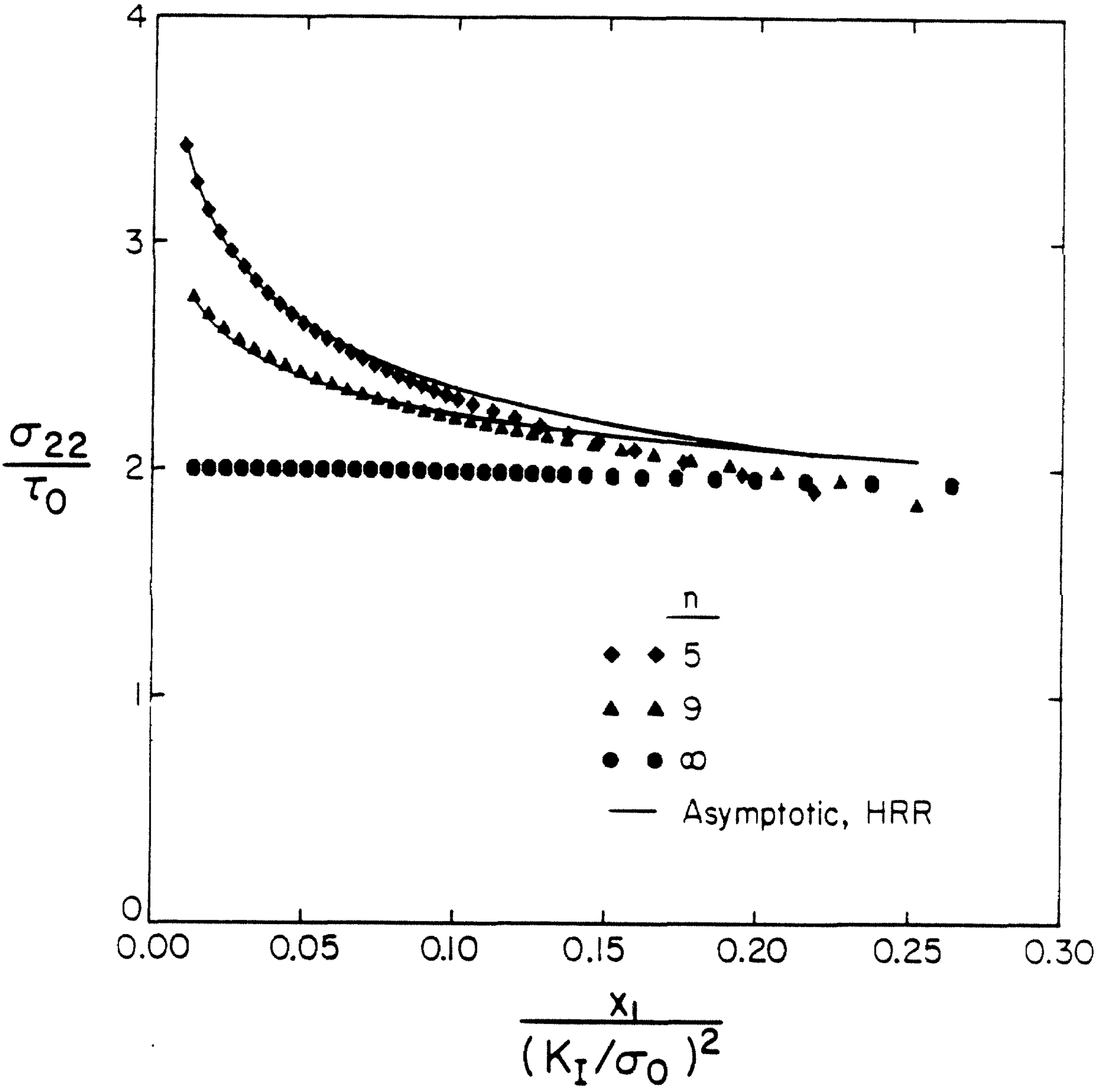

Figure 2.5. *Radial distribution of opening stress ahead of the crack tip. The solid lines represent the HRR asymptotic distribution.*

distances from the crack tip. Also, it should be observed from Fig. 2.5 that there is only slight dependence of σ_{22} on n for $x_1 > 0.15(K_I/\sigma_0)^2$. The finite element values differ by less than 10% (with respect to n) in this range.

The radial variation of all the normalized stress components ahead of the crack tip within the plastic zone for the elastic-perfectly plastic case is shown in Fig. 2.6. The finite element values near the crack tip are in excellent agreement with the asymptotic slipline solution of Hutchinson (Fig. 2.2). At $x_1 = 0.01(K_I/\sigma_0)^2$, σ_{11} and σ_{22} are $0.98\tau_0$ and $1.999\tau_0$, respectively, which compares very closely with the values of τ_0 and $2\tau_0$ given by the slipline solution (Eqn.(2.3.7)). Also Fig. 2.6 indicates that the σ_{11} stress component has a strong radial variation ahead of the crack tip, with a value at the elastic-plastic boundary of about $1.40\tau_0$. This suggests curving of the leading boundary of the fan at moderate distances from the tip.

The plane-stress Huber-Von Mises yield surface can be represented by an ellipse in principal stress space in the following parametric form [2.11],

$$\left.\begin{aligned} \sigma_1 &= 2\tau_0 \cos(\omega - \frac{\pi}{6}) \\ \sigma_2 &= 2\tau_0 \cos(\omega + \frac{\pi}{6}) \\ \omega &= \omega(r,\theta) \end{aligned}\right\} . \qquad (2.4.1)$$

For $\sigma_1 \geq \sigma_2$, the angle ω varies in the range $0 \leq \omega \leq \pi$. The governing equations for the stresses are hyperbolic if $\frac{\pi}{6} < \omega < \frac{5\pi}{6}$, parabolic if $\omega = \frac{\pi}{6}$ or $\frac{5\pi}{6}$, and elliptic if $0 \leq \omega < \frac{\pi}{6}$ or $\frac{5\pi}{6} < \omega \leq \pi$. The value of $\omega(r \to 0,0)$ corresponding to the asymptotic stresses (2.3.7) is $\frac{\pi}{6}$, whereas the stresses at the elastic-plastic boundary ahead of the crack tip give $\omega(r_p,0) \approx \frac{\pi}{12}$. Thus, while the stress state ahead of the crack is parabolic near the tip, it appears to be elliptic at the elastic-plastic boundary.

It is important from the viewpoint of optical experimental methods (such as caustics) [2.17,2.23] to determine the effect of the crack tip plastic zone on the stress

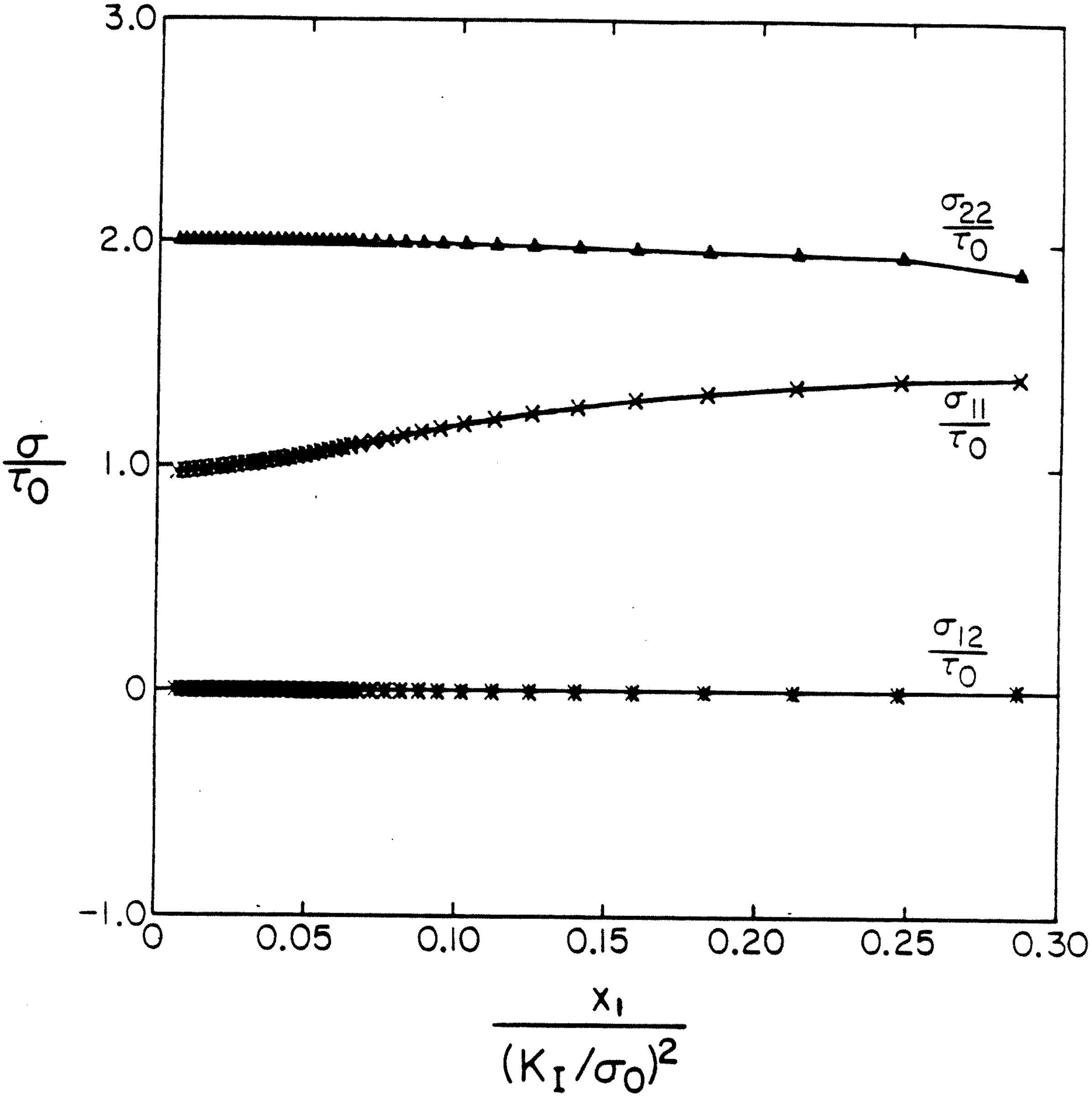

Figure 2.6. *Radial stress distribution ahead of the crack tip for the perfectly plastic case.*

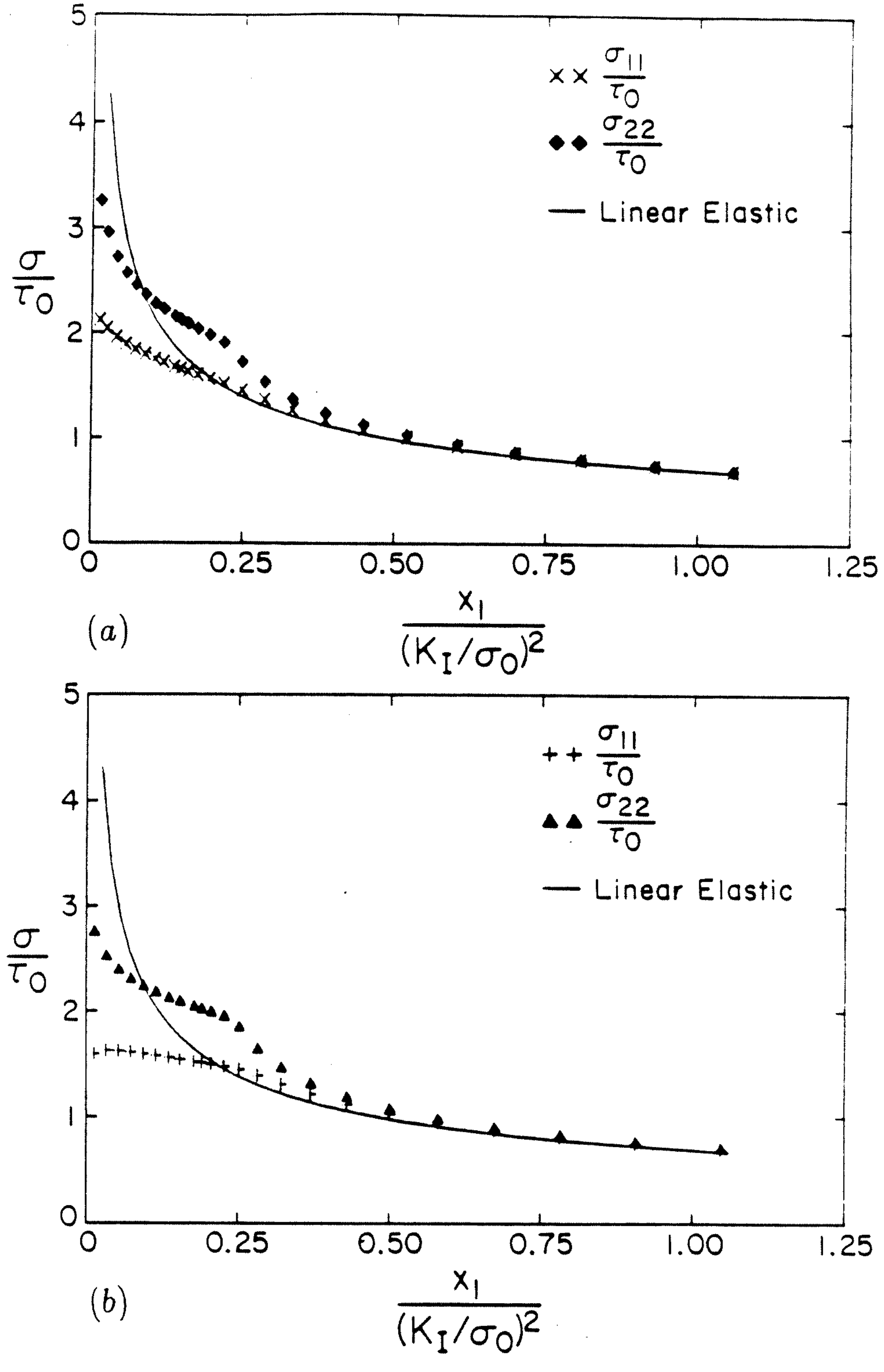

Figure 2.7. *Comparison of the radial stress distribution ahead of the tip as given by the K_I field (solid line) with the finite element solution for materials with a) n=5 and b) n=9.*

and deformation fields in the surrounding elastic region, in order to properly interpret the experimental data. To examine this effect, we show the radial distribution of stresses in the ray ahead of the crack tip on an expanded scale in Fig. 2.7 for the two levels of hardening, $n = 5$ and 9. The stresses given by the singular elastic solution (K_I field) are shown for comparison by the solid line in the figure. It is found that the σ_{22} stress component obtained from the numerical solution is higher than that given by the singular elastic field at the elastic-plastic boundary ($r = r_p$) by more than 30%. However, the stress distribution undergoes a rapid transition outside the plastic zone and differs from the K_I field by less than 8% for $r > 1.5r_p$. Also, the stress distribution in the surrounding elastic region seems to be quite insensitive to the hardening level.

Radial Distribution of Plastic Strains

The radial variation of the normalized plastic strains $\epsilon_{22}^p/\epsilon_0$ and $\epsilon_{33}^p/\epsilon_0$ with respect to normalized distance ahead of the crack tip is shown in Fig. 2.8 for the two levels of power hardening. The HRR solution for the asymptotic strain distribution (Eqn.(2.3.1)) is shown by the solid lines in the figure. The finite element solution, although slightly smaller than the HRR distribution near the crack tip, appears to indicate the correct singular behaviour in the range $r < 0.3r_p$. It should be recalled that a very detailed mesh was used near the crack tip (Fig. 2.1*b*), and that the plastic zone was quite large as compared with the smallest element size (at least 50 times) at the stage when these results were taken. These factors compensate to some extent for the incorrect modelling of the singularity (2.3.1) by our using linear shape functions for the crack tip elements.

The radial variation of the normalized plastic strains ahead of the crack tip for the elastic-perfectly plastic case is shown in Fig. 2.9. The solid line in the figure is the limit of the HRR dominant singular solution for $\epsilon_{22}^p/\epsilon_0$ for large n, which is

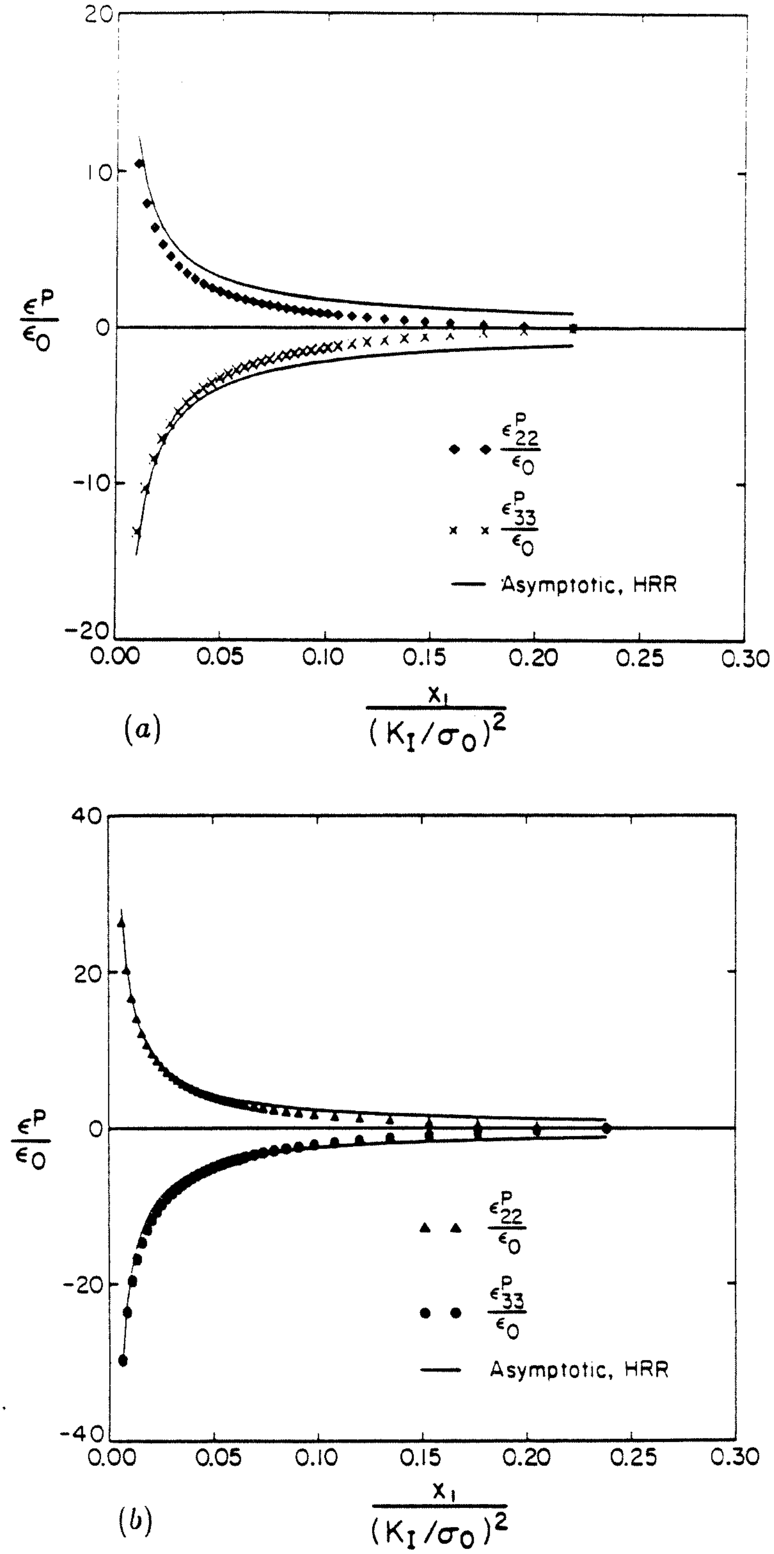

Figure 2.8. *Radial variation of the plastic strains ahead of the crack tip for materials with a) n=5 and b) n=9 and comparison with HRR solution (solid lines).*

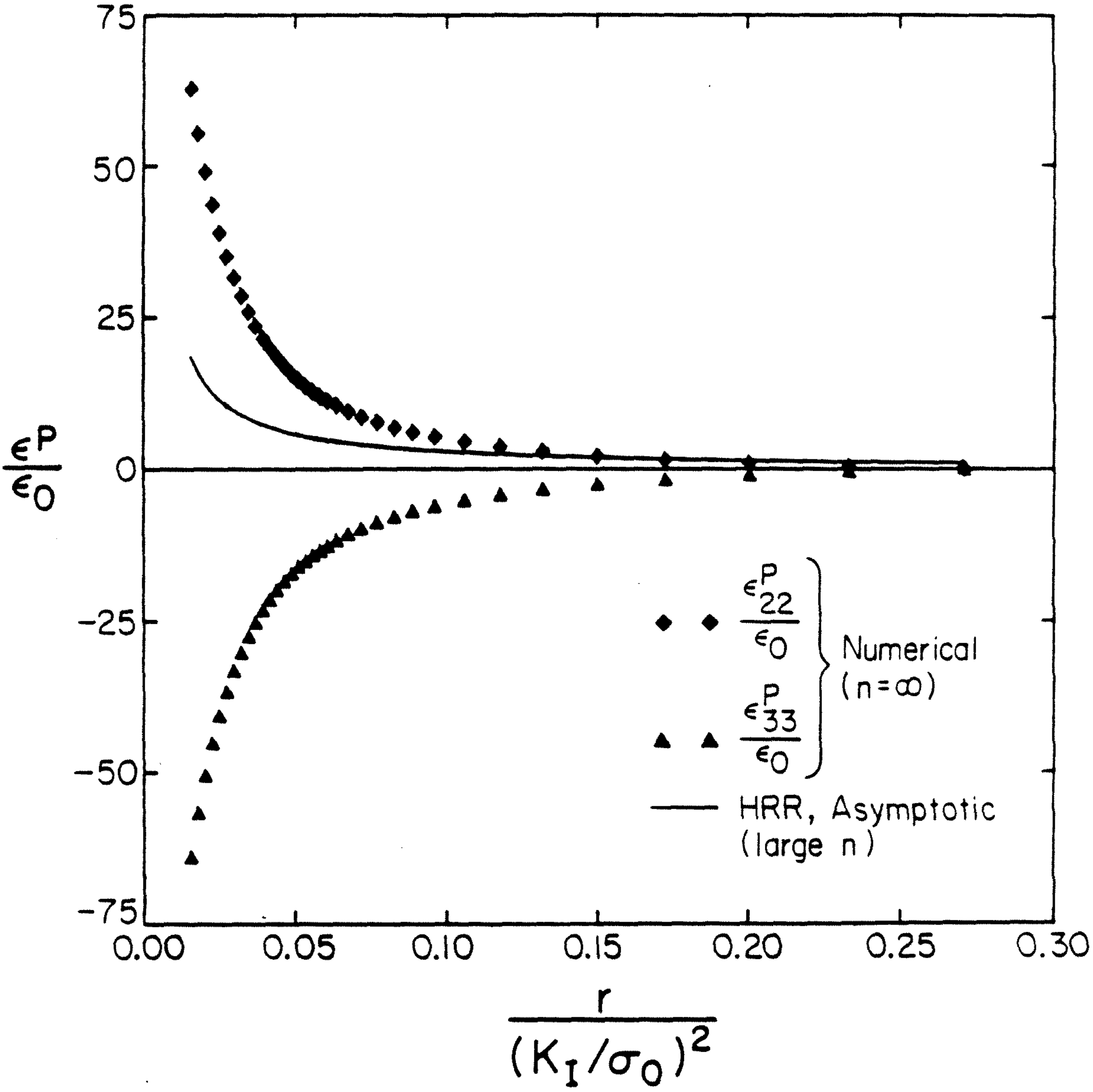

Figure 2.9. *Radial variation of plastic strains ahead of tip for perfectly plastic case. A vast discrepancy with the HRR singular solution for large n [2.14,2.17] is observed.*

given by [2.14,2.17],

$$\left.\frac{\epsilon_{22}^{p}}{\epsilon_0}\right|_{n\to\infty}^{HRR} \approx \frac{0.9\tilde{r}_p}{r}, \qquad \theta = 0, \quad r \to 0\,, \tag{2.4.2}$$

where

$$\tilde{r}_p = \frac{1}{\pi}\left(\frac{K_I}{\sigma_0}\right)^2 .$$

The finite element solution for the strains seems to indicate the correct $\frac{1}{\mathrm{r}}$ variation near the crack tip ($\mathrm{r} < 0.04(\mathrm{K_I}/\sigma_0)^2$) but is about 3.3 times the values given by (2.4.2).

As has already been noted in Sec.(2.3), the HRR singular strain solution as $\mathrm{n} \to \infty$, cannot (in general) be expected to provide the dominant solution for perfect plasticity because of the non-uniqueness in strains associated with the non-hardening case. This discrepancy has also been observed in Mode I plane strain by Levy et al.[2.13] and Rice and Tracey [2.2]. In this connection, it should also be mentioned that Knowles [2.18], in working on the finite anti-plane shear field near a crack tip in an incompressible elastic solid, with a similar power law behaviour has made an important observation. He found that the first- and second-order terms in the asymptotic expansion for the displacements tend to become of equal importance, as one approaches the equivalent of the "perfectly plastic" case in such solids. This raises the question of whether the limit as $\mathrm{n} \to \infty$ of the most singular term in the asymptotic solution can be considered separately, without examining the limiting behaviour of the higher-order terms of the expansion.

In order to resolve the issue further, a separate finite element calculation for the perfectly plastic case was performed under plane stress, small-scale yielding conditions using a focussing mesh with singular elements near the crack tip, similar to the work of Rice and Tracey [2.2]. The results of this investigation will be reported in Sec.(2.6). Finally, it should be noted that the region ahead of the crack tip, wherein the $\frac{1}{r}$ variation of the plastic strains was observed ($r < 0.04(K_I/\sigma_0)^2$), corresponds to the region of dominance of the asymptotic stress field (see Fig. 2.6). Beyond this range, the front boundary of the fan may tend to curve and the $\frac{1}{r}$ variation for the plastic strains may no longer be valid [2.1,2.7].

Crack Opening Displacement

The opening displacement between the crack faces as a function of position along the crack flank is shown in Fig. 2.10 in the nondimensional form, $\delta/(J/\sigma_0)$ versus $x_1/(K_I/\sigma_0)^2$, for the three cases, $n = 5, 9$ and ∞. The linear elastic solution corresponding to $n = 1$ is also plotted for comparison. J in this plot is the far-field value given by (2.3.3). From the figure, it can be observed that the amount of blunting at the crack tip increases with decreasing hardening (or increasing n). There is a discrete opening displacement at the tip for the perfectly plastic idealization because of reasons stated in Sec.(2.3).

On the other hand, the near-tip crack opening profile for the hardening cases, computed on the basis of the HRR analysis, has the form [2.8,2.10],

$$\delta = 2u_2(r,\pi) \sim \left(2r(\delta_t)^n\right)^{\frac{1}{n+1}}, \qquad r \to 0 . \tag{2.4.3}$$

In this expression, δ_t, which can be written as

$$\delta_t = \frac{J}{\sigma_0}\tilde{\delta}_t(\epsilon_0, n) , \tag{2.4.4}$$

can be approximately interpreted as the opening distance between the intercept of two 45° lines drawn back from the crack tip to the deformed profile. This definition was suggested by Tracey [2.16] as a measure of the crack tip displacement for a hardening material, since $\delta(r = 0) = 0$ in this case, as can be seen from (2.4.3). Shih [2.19] has obtained the values for $\tilde{\delta}_t(\epsilon_0, n)$ from the HRR solution for both plane stress and plane strain. It is found [2.19] that $\tilde{\delta}_t$ is strongly dependent on

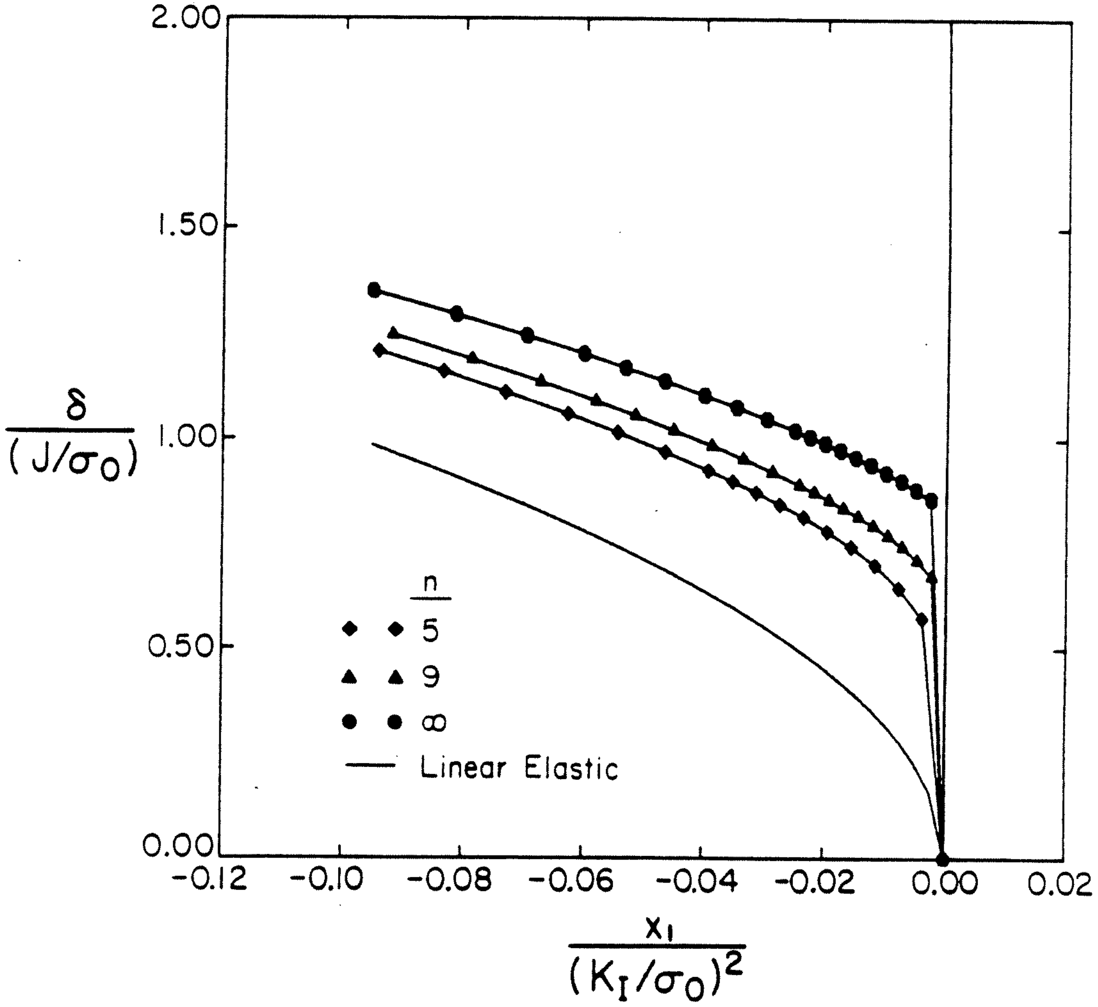

Figure 2.10. *Normalized crack opening profiles for several values of hardening.*

n and weakly on ϵ_0. Also, as $n \to \infty$, $\tilde{\delta}_t$ becomes independent of ϵ_0 and takes the value of 1.0 for plane stress.

From the present finite element calculation, the value of $\delta_t/(J/\sigma_0)$ was obtained by extrapolating the near-tip crack profile to $r = 0$ for the non-hardening case and by fitting the form (2.4.3) to the near-tip profile for the hardening cases. Shih [2.19] has also computed the values of $\delta_t/(J/\sigma_0)$ for several values of n from his finite element solution of [2.14], which as noted earlier employed a deformation plasticity theory. These results are summarized in the following table.

Table 2.1: Values of $\delta_t/(J/\sigma_0)$ for plane stress

	σ_0/E	$n = 5$	$n = 9$	$n = 25$	$n = \infty$
HRR	0.0012	0.40	0.63	0.89	1.0*
Present Solution	0.0012	0.37	0.57		0.85
Shih [2.14,2.19]		0.38		0.86	

*(extrapolated)

The slightly smaller values for $\delta_t/(J/\sigma_0)$ obtained by the present solution, as compared to HRR for the hardening cases, can be accounted partially by some discrepancy between flow theory and deformation theory as explained below. But the difference between the present perfect plasticity calculation and the HRR non-hardening limit is because the latter is unable to provide complete information regarding the most singular term for the strains in the asymptotic solution for perfect plasticity, as described above. This discrepancy has also been observed in plane strain. The published numerical results [2.19] for $\delta_t/(J/\sigma_0)$ under plane strain, small-scale yielding conditions for the perfectly plastic case range from 0.63-0.66, whereas the HRR non-hardening limit is 0.78.

J integral calculations

In order to assess the difference between the present incremental formulation and the deformation plasticity theory, we checked the path independence of the J integral. The J integral (2.3.2) was computed for the hardening materials along several contours surrounding the crack tip, which passed through the centroids of the elements. The near-tip contours enclosing the crack tip were rectangular, while the far-field contours were circular, in keeping with the structure of the mesh (Fig. 2.1). The integrand in (2.3.2) was calculated, using the averaged values of stresses and strains at the centroids of the elements lying in the contour path, and the integration was carried out numerically using Gauss quadrature. It was found that very near the crack tip ($r < 0.04r_p$) there was a small amount of path dependence. However, after some distance away from the crack tip, the calculated J value was virtually indistinguishable from the remotely applied value (2.3.3).

For a contour with an average radius $\bar{r} = 0.012(K_I/\sigma_0)^2$, the ratio of the calculated J value to the remotely applied J was 0.96 and 0.95 for $n = 5$ and 9, respectively. For contours with average radius $\bar{r} > 0.05(K_I/\sigma_0)^2$, the calculated J value was smaller than the applied J by less than 1%. While the 5% difference for the near-tip contours is within the realm of errors in the discretization procedure and in the numerical integration of (2.3.2), it also suggests small amounts of non-proportional loading experienced by a material particle from the time it was enveloped by the plastic zone. For the elastic-perfectly plastic material, our accurate numerical solution of Sec.(2.6) was used to estimate the near-tip J integral, and its discussion will be deferred till then.

In order to further check for discrepancy between the two plasticity theories, we calculated $\epsilon_{22}^p/\epsilon_0$ for the hardening materials at the centroids in the row of elements ahead of the crack tip by substituting the averaged stresses in these elements into the expression given by the J_2 deformation theory. The plastic strain given by the J_2 deformation theory was about 5% higher at $r = 0.012(K_I/\sigma_0)^2$ than the corresponding value given by the incremental formulation that was reported earlier (Fig. 2.8). This difference progressively diminished as the distance from the crack tip increased, and it was less than 1% for $r > 0.1(K_I/\sigma_0)^2$.

2.5 NUMERICAL SIMULATION OF CAUSTICS

Introduction

The optical experimental method of caustics has been applied to the study of linear elastic fracture problems and to the direct measurement of the stress intensity factors [2.31,2.20,2.21]. This method was recently extended to the measurement of the J integral in ductile fracture [2.17,2.22] on the basis of the validity of the plane stress, HRR asymptotic solution.

Under conditions of small-scale yielding, the singular elastic field dominates well outside the plastic zone. Inside the plastic zone, very near the crack tip, the HRR field dominates. In the transition region between these two fields, no analytical solution is available. This limits the applicability of caustics, and the conditions under which the results reported in [2.17,2.22] are valid are uncertain. Also, errors may be caused in the measurement of K_I based on the caustics obtained from the elastic region surrounding the plastic zone. This is because the crack tip plastic zone affects the caustic patterns, and an analysis based on the K_I field may be erroneous.

In this section, the full-field numerical solution under small-scale yielding is used to generate simulated caustic patterns. The numerical caustics are compared with the corresponding patterns observed from experiments [2.23]. The analysis of caustics based on the numerical results is not limited by the assumption of the validity of any particular asymptotic field. Finally, qualitative and quantitative comparisons of the simulated caustics, obtained at various distances from the crack tip, are made with the corresponding results based on the near-tip HRR analysis and the remotely applied K_I field.

The Method of Caustics

Consider a set of parallel light rays normally incident on a planar, reflective specimen that has been deformed by tensile loading. Due to the deformed shape of the specimen, an envelope in space called the "caustic surface" is formed by the virtual extension of the reflected light rays (Fig. 2.11). The intersection of this surface with a plane located at a distance z_0 behind the specimen is called the "caustic curve," and it bounds a dark region called the "shadow spot."

Let (x_1, x_2) be a coordinate system on the specimen surface centered at the crack tip and (X_1, X_2), a system translated by a distance z_0 behind the specimen surface. Then the mapping of a point (x_1, x_2) on the specimen surface to a point (X_1, X_2) on the plane at z_0 due to reflection of a light ray may be described by [2.21],

$$X_\alpha = x_\alpha + 2z_0 \frac{\partial u_3(x_1, x_2)}{\partial x_\alpha} \ . \tag{2.5.1}$$

The locus of points on the specimen surface at which the Jacobian determinant of the mapping (2.5.1) vanishes is called the "initial curve." While points on the initial curve map onto the caustic curve, all points both inside and outside the initial curve map outside the caustic. The position of the initial curve may be varied by changing z_0.

For a stationary crack under small-scale yielding conditions, if the initial curve is chosen to fall well outside the plastic zone and within the region of validity of the K_I field (large values of z_0), then the resulting caustic curve will be an epicycloid (Fig. 2.12*a*). In such a case, K_I is related to the caustic diameter D (which is the

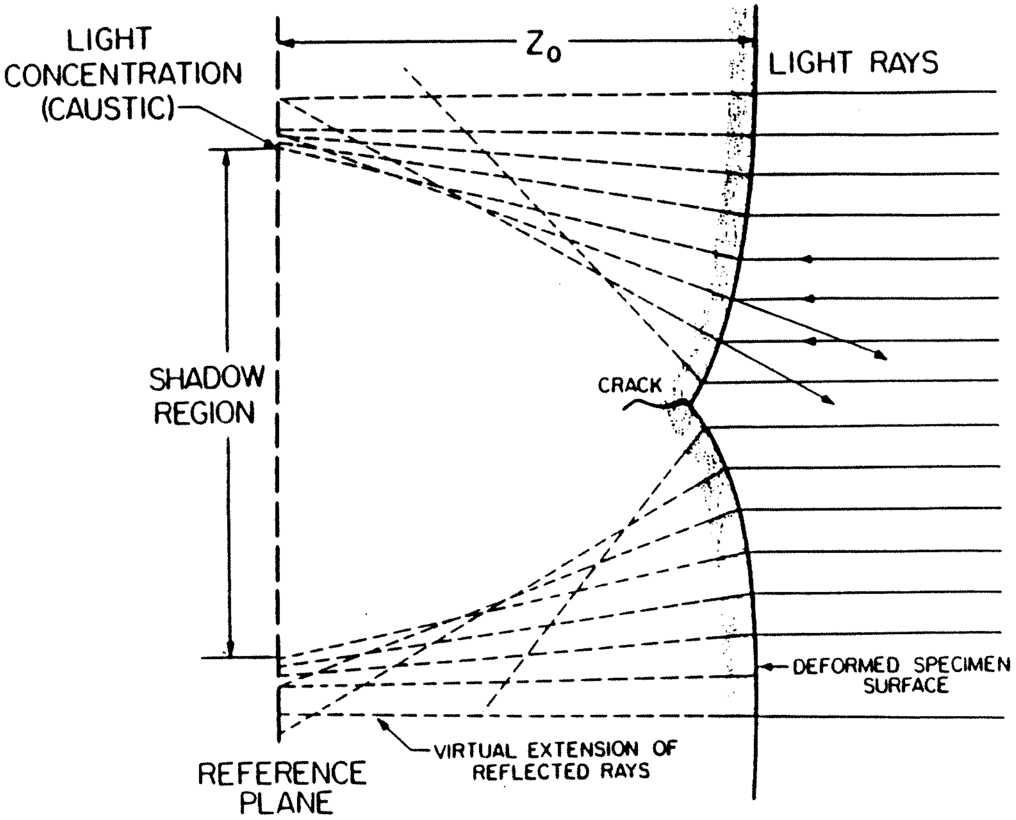

Figure 2.11. *Formation of caustic due to reflection of light from a polished, deformed specimen surface.*

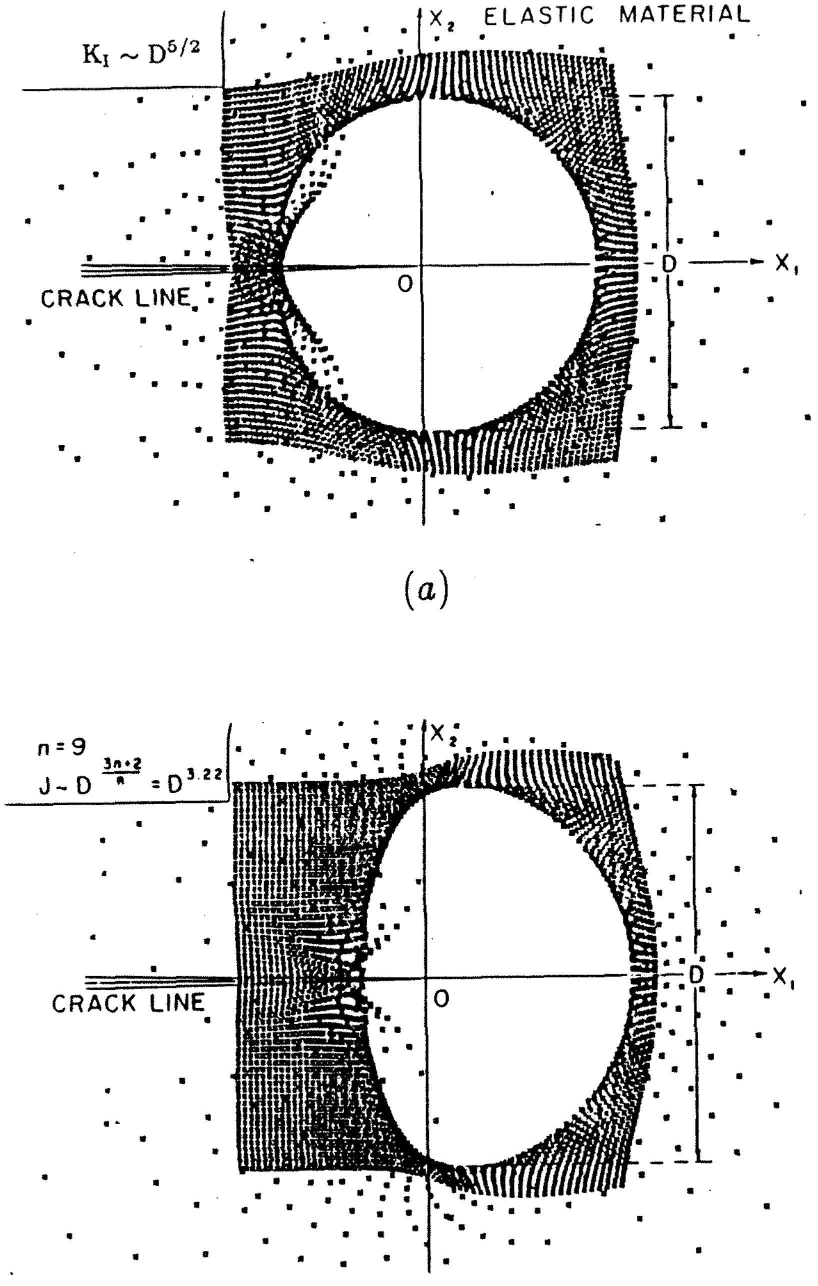

(a)

(b)

Figure 2.12. *Predicted caustic shapes based on a) K_I field and b) HRR asymptotic field for n=9.*

maximum width of the caustic in the X_2 direction) by [2.20,2.21],

$$K_I = \frac{ED^{5/2}}{10.7 z_0 \nu h}, \qquad (2.5.2)$$

where h is the specimen thickness. The initial curve is circular and its radius r_0 is given by

$$r_0 = 0.316D. \qquad (2.5.3)$$

On the other hand, if the initial curve is chosen to fall well inside the plastic zone and within the region of dominance of the HRR field (very small values of z_0), then its shape as deduced in [2.17] will no longer be circular. In such a case, the radius r_0 of the point on the initial curve that maps to the maximum value of X_2 on the caustic curve is given by

$$r_0 = 0.385D \qquad (2.5.4)$$

for a hardening exponent n of 9. Also, the value of the J integral may be obtained from the caustic diameter D as [2.17],

$$J = S_n \frac{\sigma_0^2}{E} \left[\frac{E}{\sigma_0 z_0 h} \right]^{\frac{n+1}{n}} D^{\frac{3n+2}{n}}, \qquad (2.5.5)$$

where S_n is a numerical factor dependent on n. Caustic curves thus obtained from the HRR field for several values of the hardening exponent are given in [2.17]. A typical caustic for n=9 is shown in Fig. 2.12*b*.

Results and Discussion

The discrete values of the out-of-plane displacement u_3 obtained from the numerical solution at the centroids of the elements were smoothed using a least-squares finite element scheme as advocated by Hinton and Campbell [2.24]. The surface thus generated is shown in Fig. 2.13 for a material with a hardening exponent of

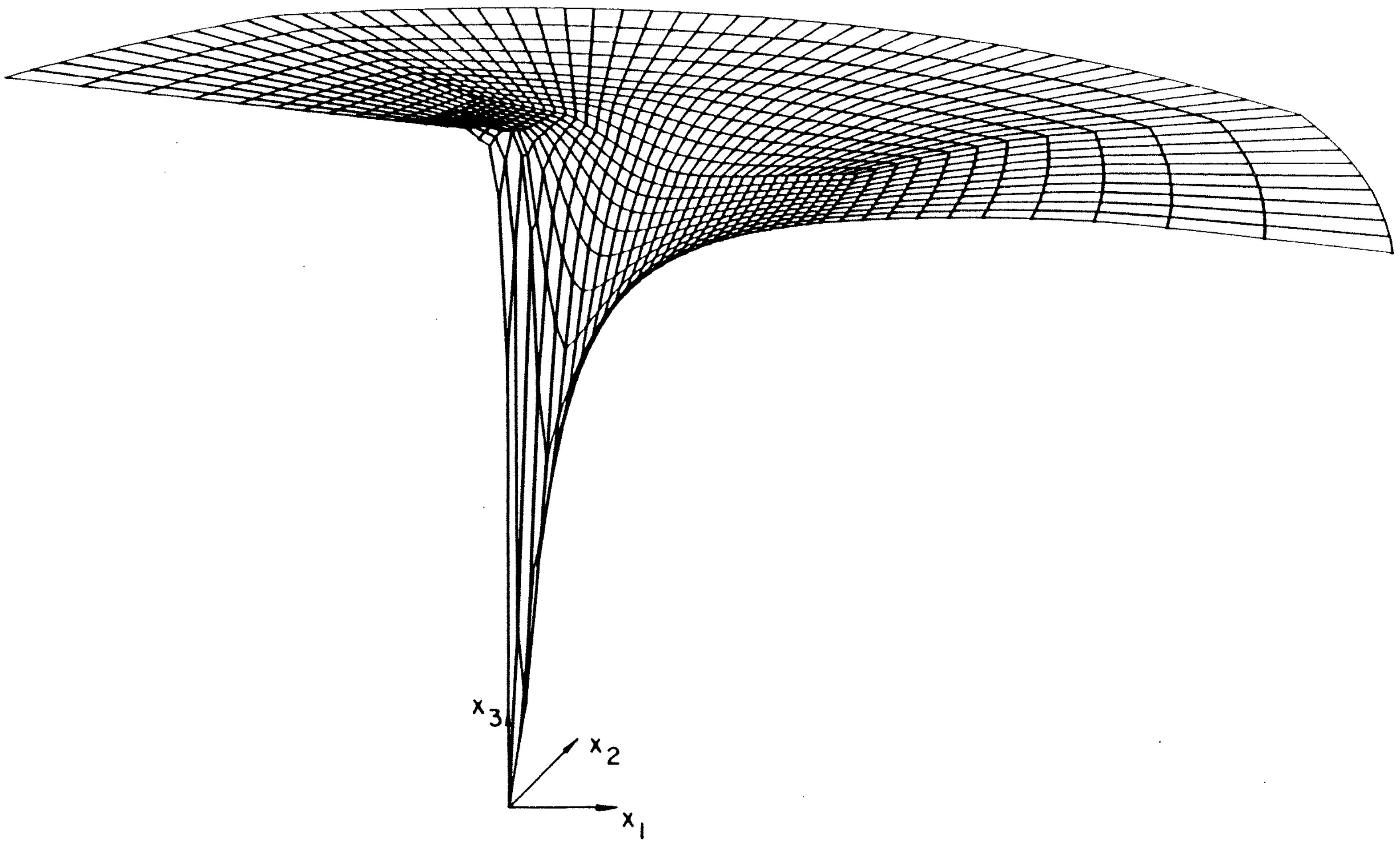

Figure 2.13. *Smoothed out-of-plane displacement field for n=9.*

9. Caustic patterns were simulated by mapping light rays point by point from this smoothed surface using Equation (2.5.1) for different values of z_0.

The sequence of caustics simulated from the finite element solution for different values of z_0 is shown in Fig. 2.14 for a material with $n = 9$. The parameter r_0/r_p in the figure is the ratio of the initial curve size to the maximum plastic zone extent. The initial curve size r_0 was estimated approximately by using Equation (2.5.4) for caustics from within the plastic zone and by Equation (2.5.3) for caustics from outside the plastic zone. It is seen from the figure that for $r_0/r_p = 0.19$, the simulated caustic agrees in shape with the caustic predicted by the HRR field, which is shown in Fig. 2.12*b*. When $r_0/r_p = 1.3$, the numerically simulated caustic, Fig. 2.14*f*, agrees with the caustic predicted using the elastic, K_I field (Fig. 2.12*a*).

A sequence of photographs of caustics [2.23] obtained from the tensile loading of a thin compact tension specimen of 4340 carbon steel is shown in Fig. 2.15. The experimental details, specimen dimensions, etc. are described in [2.23]. On comparing Figs. 2.14 and 2.15 we see that in both cases there is a transition from an "HRR caustic" to an "elastic caustic" as $\frac{r_0}{r_p}$ goes from 0.19 to 1.4. The transition away from the HRR caustic appears to take place slightly sooner in the numerical model (around $\frac{r_0}{r_p} = 0.3$) than in the experiment (around $\frac{r_0}{r_p} = 0.35$). However, the general trend is similar in both cases.

It is found that both the numerical and experimental caustics retain the shape predicted by the K_I field even for r_0/r_p as small as 1.0. Thus, the effect of the plastic zone cannot be judged by mere observation of the caustic shape. The reason for the invariance in shape of the caustics is explained by examining the angular variation of the sum $(\sigma_{11} + \sigma_{22})$, of the direct stress components (as given by the numerical solution), at different distances outside the plastic zone as shown in Fig. 2.16. It is seen that the sum $(\sigma_{11} + \sigma_{22})$ generally follows the angular distribution given by the

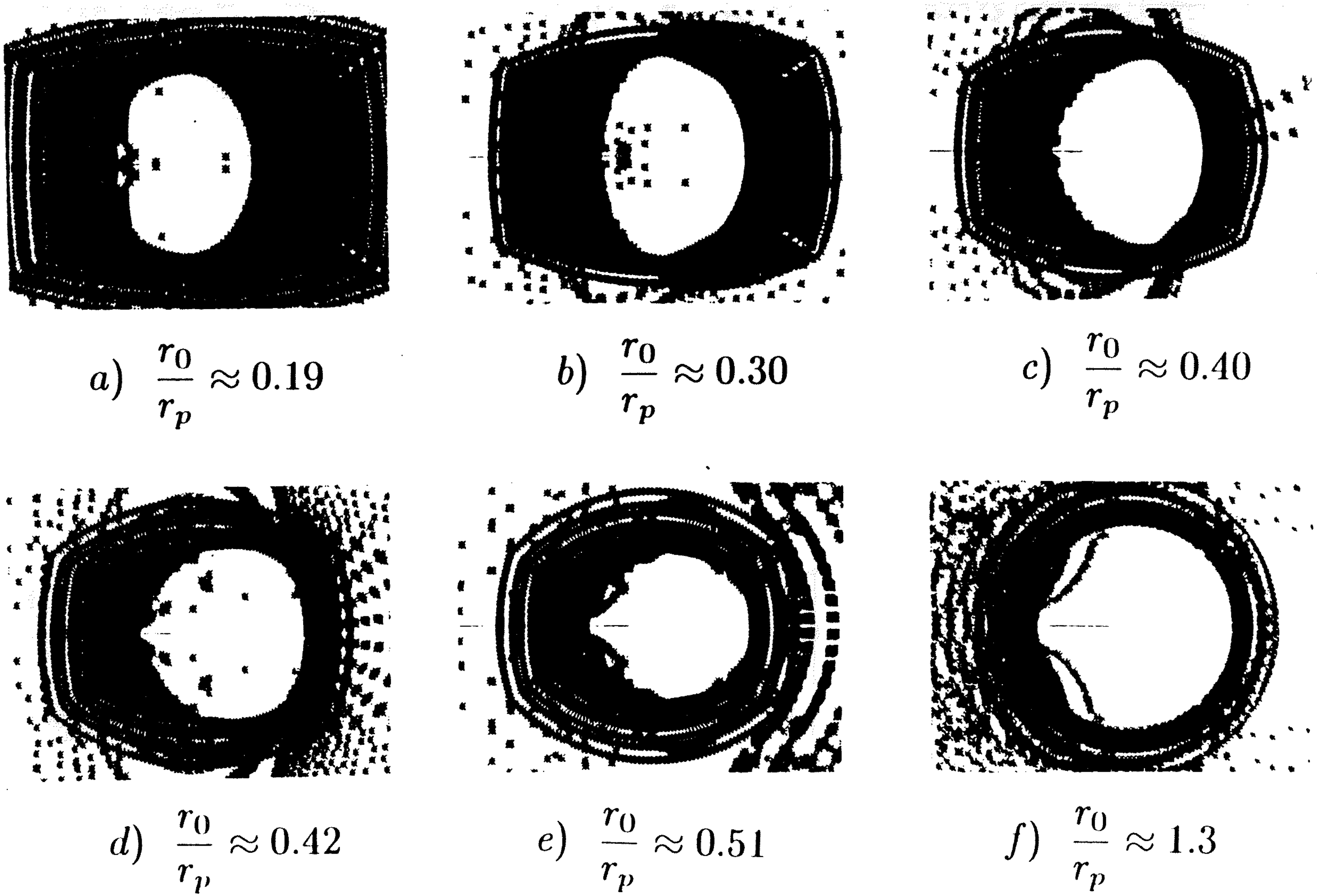

a) $\frac{r_0}{r_p} \approx 0.19$ b) $\frac{r_0}{r_p} \approx 0.30$ c) $\frac{r_0}{r_p} \approx 0.40$

d) $\frac{r_0}{r_p} \approx 0.42$ e) $\frac{r_0}{r_p} \approx 0.51$ f) $\frac{r_0}{r_p} \approx 1.3$

Figure 2.14. *Sequence of caustics simulated from the numerical solution.*

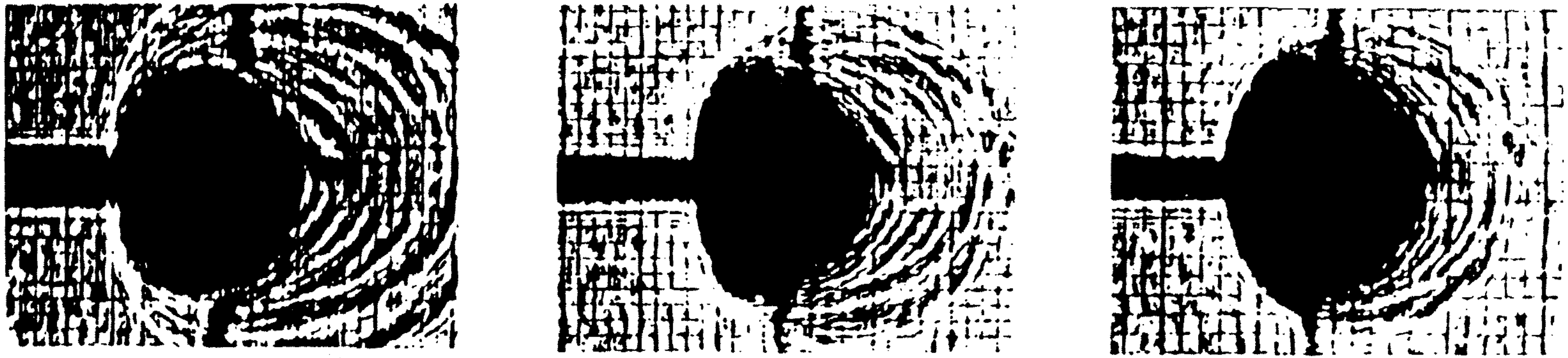

$a)\ \frac{r_0}{r_p} \approx 0.26$ $b)\ \frac{r_0}{r_p} \approx 0.35$ $c)\ \frac{r_0}{r_p} \approx 0.45$

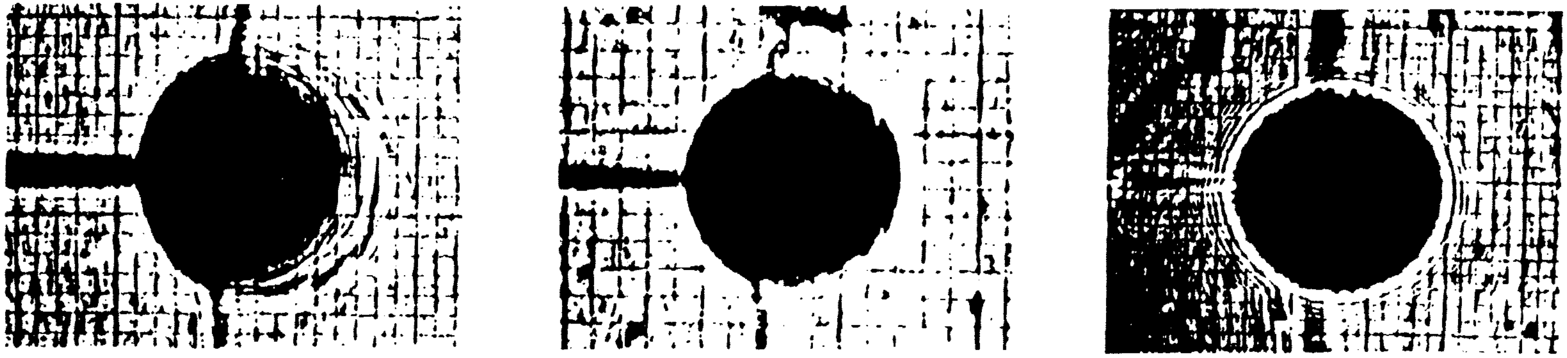

$d)\ \frac{r_0}{r_p} \approx 0.52$ $e)\ \frac{r_0}{r_p} \approx 0.70$ $f)\ \frac{r_0}{r_p} \approx 1.4$

Figure 2.15. *Sequence of caustics obtained from experiments [2.23].*

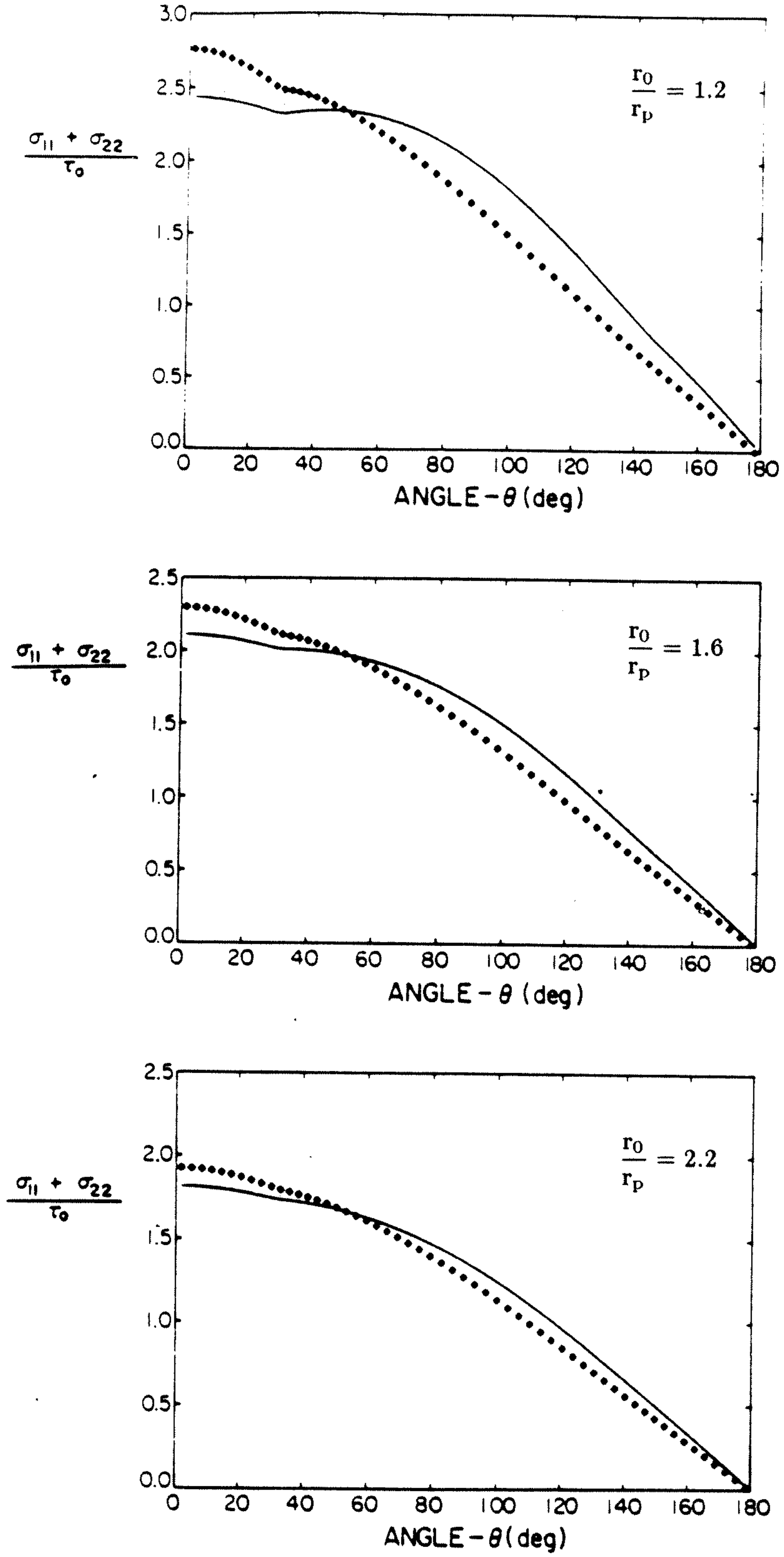

Figure 2.16. *Angular distribution of* $(\sigma_{11} + \sigma_{22})$ *for different distances from the tip. The solid line is the distribution given by the* K_I *field.*

K_I field, which is shown by the solid line in the figure even for r_0/r_p as small as 1.2. However, the individual stress components show more deviation from those of the K_I field for small values of r_0/r_p. This observation is important, since the caustic shape depends on the angular variation of the out-of-plane displacement component u_3, which in the elastic region, is proportional to $(\sigma_{11} + \sigma_{22})$ under plane stress. Thus, it is not surprising that the caustic shape resembles the "elastic caustic" for r_0/r_p as small as 1.0.

The numerical caustics were simulated for a fixed value of K_I (or the far-field value of J as given by (2.3.3)) by varying z_0 in the optical mapping Equation (2.5.1). The relationship between the diameter D of the simulated caustics and the remotely applied J value is shown in non-dimensional form in Fig. 2.17. The inverse of the abscissa in the figure is an indication of the initial curve size or the distance from the crack tip at which the information about the deformation field is being scrutinized. Thus, a very small abscissa value (large z_0 or small J) implies that the initial curve is far away from the tip. A very large abscissa value, on the other hand, implies that the curve is very near the tip, probably within the range of dominance of the HRR field. The bars on the numerical results indicate the uncertainty in determining the initial curve due to discretization of the finite elements.

The solid line in the figure represents the variation of caustic size in the K_I dominated region as given by (2.5.2) with $\nu = 0.3$. The dashed line gives the relationship for the caustics from the HRR-dominated region (2.5.5). As can be observed from this figure, the numerical results approach the elastic relation (2.5.2) for small abscissa values and the relation (2.5.5) obtained from the HRR solution for large values of the abscissa. In the intermediate region there is a transition from one distribution to the other.

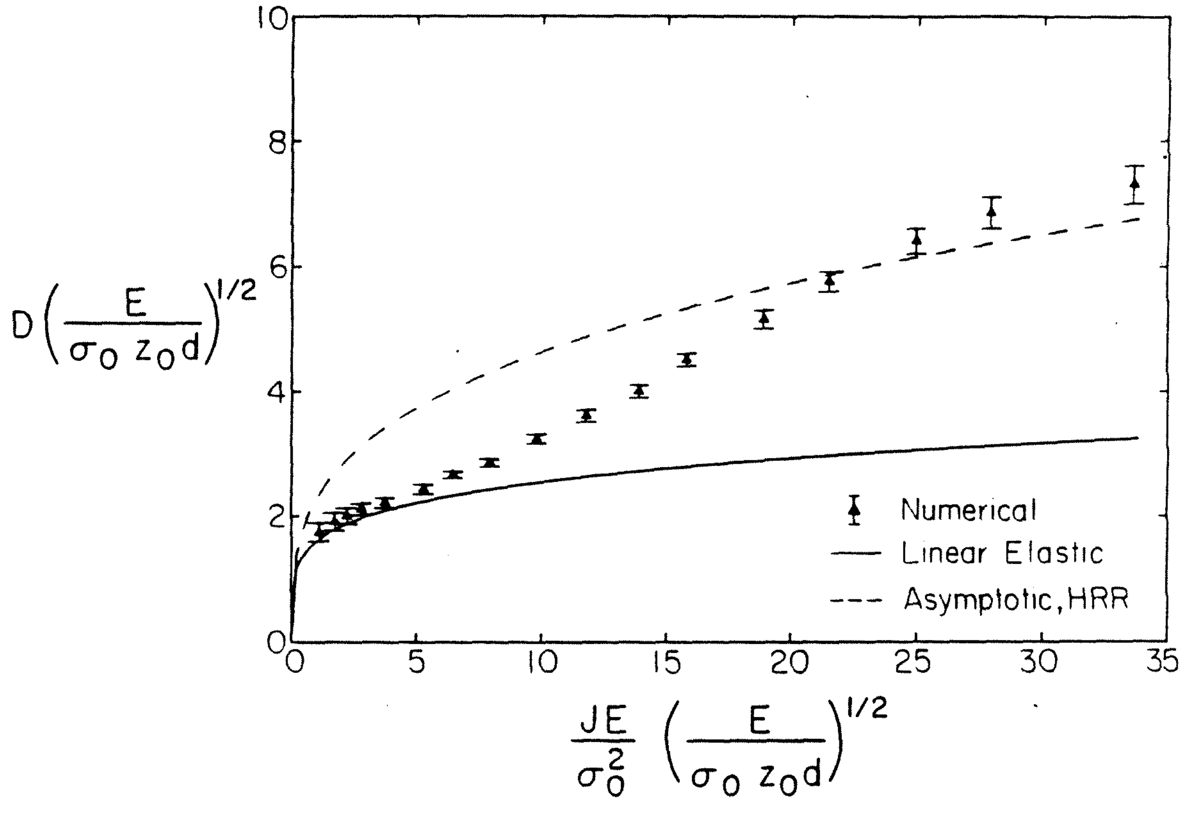

Figure 2.17. *Relationship between caustic diameter and the J integral as obtained from the numerically simulated caustics.*

2.6 SINGULAR FINITE ELEMENT ANALYSIS

Introduction

In this section, a detailed investigation of the perfectly plastic case will be presented, with the view of examining closely the discrepancy between the numerical results for the near-tip strains and the corresponding term of the HRR solution (non-hardening limit), which was noted in Sec.(2.4). For this purpose, a singular finite element analysis similar to the plane strain work of Rice and Tracey [2.2] was carried out under Mode I plane stress, small-scale yielding conditions. A ring of focussed isosceles triangular-shaped elements was used near the crack tip in this computation. This mesh design is different from the fine mesh employed in the earlier analysis (Fig. 2.1*b*). Thus, the issue of sensitivity of the numerical results presented earlier in Sec.(2.4) to the near-tip mesh design was also examined through this section of the present chapter.

Numerical Scheme

The near-tip elements that were employed here provide a capability for non-uniqueness of displacement at the crack tip [2.2,2.13], which is the fundemental feature of the 1/r plastic strain singularity within centered fan regions (Sec.(2.3)). This was acheived by treating the triangular elements at the crack tip as degenerate isosceles trapezoids that have a total of four nodes (one at each vertex) with two nodes coinciding at the crack tip (Fig. 2.18). The coincident nodes at the crack tip were constrained to move as a single point till the load level at which incipient yielding was detected in one of the near-tip elements. A special shape function [2.2] was used up to this load level to provide the crack tip elements the capability to model the $1/\sqrt{r}$ dominant elastic strain singularity. Subsequently, the coincident nodes were allowed to move independently and the crack tip elements modelled the 1/r plastic strain singularity.

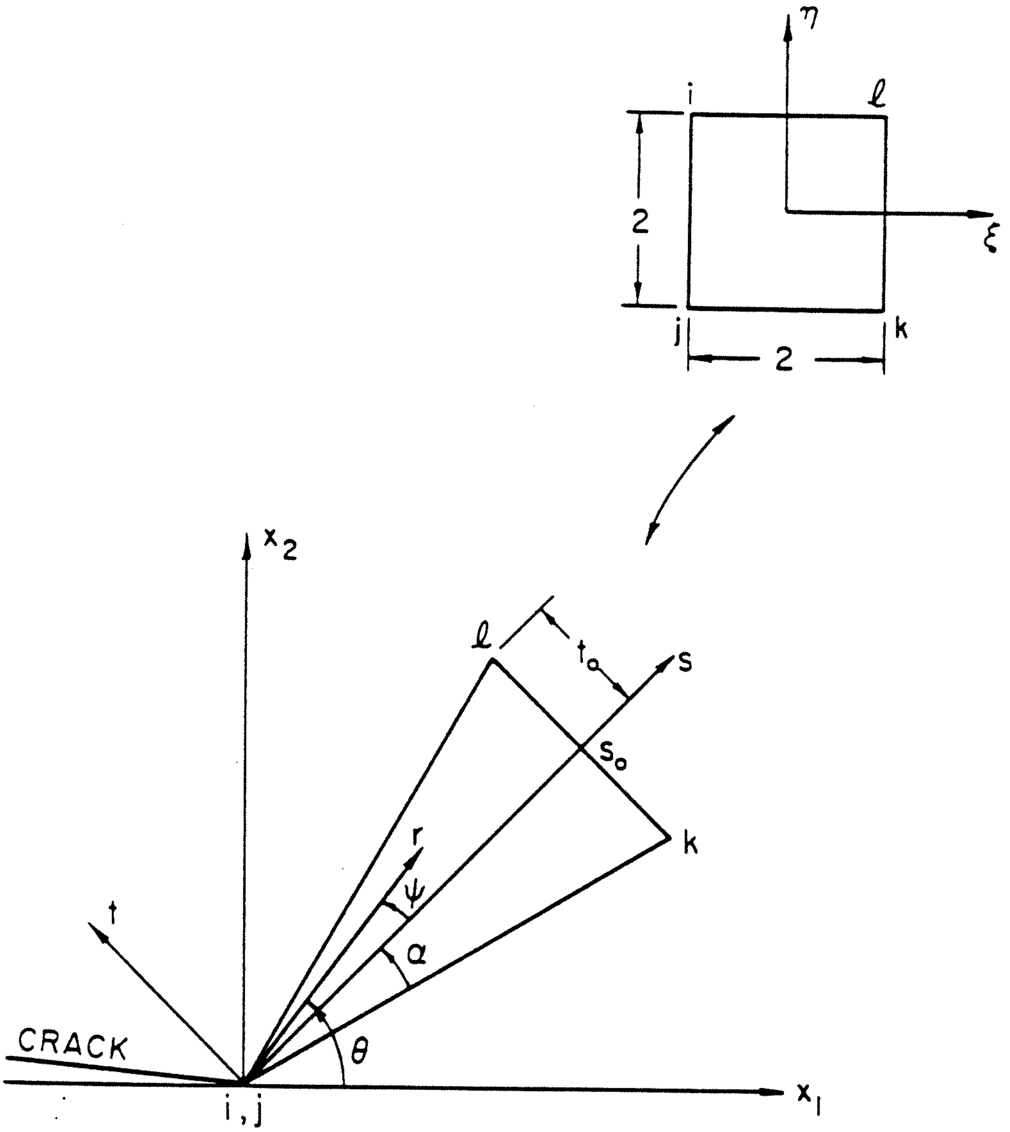

Figure 2.18. *Typical near-tip element used in the singular finite element analysis.*

The mapping of a four-noded rectangle to a triangle (Fig. 2.18) can be described by

$$\underline{x} = \underline{x}^{i}\frac{(1-\xi)(1+\eta)}{4} + \underline{x}^{j}\frac{(1-\xi)(1-\eta)}{4} + \underline{x}^{k}\frac{(1+\xi)(1-\eta)}{4} + \underline{x}^{l}\frac{(1+\xi)(1+\eta)}{4}\,, \tag{2.6.1}$$

with the constraint $\underline{x}^{i} = \underline{x}^{j}$. Here (ξ, η) is the natural coordinate system for the element and (x_1, x_2) is a global coordinate system centered at the crack tip. The inverse mapping of (ξ, η) in terms of a local Cartesian coordinate system (s,t), and a local polar coordinate system (r, ψ) for the element is given by (Fig. 2.18),

$$\left.\begin{aligned} \xi &= \frac{2s}{s_0} - 1 \\ \eta &= \frac{t/s}{(t_0/s_0)} = \frac{\tan\psi}{\tan\alpha} \end{aligned}\right\} . \tag{2.6.2}$$

The elastic singularity element has the shape function [2.2],

$$\underline{u} = \underline{u}^{ij}\left(1 - \sqrt{\frac{1+\xi}{2}}\right) + \underline{u}^{k}\frac{(1-\eta)}{2}\sqrt{\frac{1+\xi}{2}} + \underline{u}^{l}\frac{(1+\eta)}{2}\sqrt{\frac{1+\xi}{2}}\,. \tag{2.6.3}$$

Here $\underline{u}^{ij}$ represents the unique displacement of the crack tip nodes i and j. The above element correctly models the $\sqrt{r}$ variation in the leading term for the displacements of the linear elastic solution. Also, displacement compatibility is satisfied along the edges i-l and j-k ($\eta = \pm 1$) with the adjacant singular elements and along the edge l-k ($\xi = 1$) with the conventional four-noded isoparametric element that is joined there.

As was first pointed out by Levy et al.[2.13], the mapping of any four-noded isoparametric element to a triangle leads to a 1/r strain variation provided that the coincident nodes are permitted to have different displacements. The crack tip displacement for such an element is given by (Fig. 2.18),

$$\underline{u}(-1, \eta) = \frac{(\underline{u}^{i} + \underline{u}^{j})}{2} + \eta\frac{(\underline{u}^{i} - \underline{u}^{j})}{2}\,. \tag{2.6.4}$$

Following the notation of (2.3.9) and neglecting the elastic strains that are bounded, it can be shown from (2.6.4) that

$$\left.\begin{aligned}\hat{\epsilon}^{p}_{\theta\theta} &= \frac{E}{\sigma_0}\left(\frac{\sec\psi}{2\tan\alpha}\right)\left[-(u^{i}_{s}-u^{j}_{s})\tan\psi+(u^{i}_{t}-u^{j}_{t})\right] \\ \hat{\epsilon}^{p}_{r\theta} &= \frac{E}{\sigma_0}\left(\frac{\sec\psi}{4\tan\alpha}\right)\left[(u^{i}_{s}-u^{j}_{s})+(u^{i}_{t}-u^{j}_{t})\tan\psi\right]\end{aligned}\right\}, \tag{2.6.5}$$

where u_s and u_t are the displacement components in the local (s,t) Cartesian coordinate system and ψ is the angle measured in the local (r,ψ) polar coordinate system (Fig. 2.18) for the element. It should be noted that the right-hand side of (2.6.5) is a first-order finite difference approximation to $\hat{\epsilon}^{p}_{\theta\theta}(\psi)$ and $\hat{\epsilon}^{p}_{r\theta}(\psi)$. Also, it should be noted that if the two coincident nodes displace as a single point, so that $\underline{u}^{i}=\underline{u}^{j}$, then this element behaves as an ordinary constant strain triangle.

The mesh employed in this analysis was similar to the one used by Levy et al.[2.13]. Only the upper half-plane was considered because of symmetry. The active mesh consisted of 20 rings with radii of $L, (1.5)^2L, (2.0)^2L, \ldots, (9.5)^2L, (10.0)^2L$ and 115L. These were divided by 25 rays at equal angular intervals of 7.5°, giving a total of 525 nodes (including 25 coincident crack tip nodes) and 480 elements in the active mesh. The region outside consisted of 14 rings with 24 elements in each ring and always remained elastic. Static condensation was employed in this region as described in Sec.(2.2). The radius of the outermost boundary S on which the displacement boundary condition (2.2.1) was specified was 645L. The loading process was stopped when the maximum plastic zone extent was about $\frac{1}{15}$ of the radius of the outermost boundary S, so that the small-scale yielding condition was preserved. The symmetry condition (2.2.2) on the $\theta=0$ ray and the traction-free condition on the $\theta=\pi$ ray were enforced.

Every near-tip element was composed of three subelements [2.2], each extending to one-third of the height of the element. A nine-point numerical integration scheme was employed to integrate the element stiffness matrix, with integration stations at ($\xi, \eta = -\frac{2}{3}, 0, \frac{2}{3}$) and weighting factors of $\frac{1}{9}$ of the area of the element. For the isoparametric elements outside the innermost ring, the two-by-two Gauss quadrature scheme was used. The solution strategy was the same as that described in Sec.(2.2) with the additional modifications mentioned earlier in this section.

Results and Discussion

It can be shown by substituting the dominant term of the elastic solution for the stresses into the plane stress Von Mises yield condition that incipient yielding will occur at an angle of $\arccos(\frac{1}{3}) \approx 70.5°$. Also, the value of the load parameter, $K_I^\circ/(\sigma_0\sqrt{2\pi r_y})$, calculated from the analytical solution is 0.866 for initial yielding at a radius of r_y. Incipient yielding occurred in the present finite element computation in the subelement between 67.5° and 75° with a mean angle of 71.25°. The value of $K_I^\circ/(\sigma_0\sqrt{2\pi r_y})$ was 0.83, which is in good agreement with the analytical prediction.

The radial distribution of stresses along the ray ahead of the crack tip at incipient yield is shown in Fig. 2.19 in the nondimensional form, σ/τ_0 versus $r/(K_I/\sigma_0)^2$. The stresses given by the finite element solution are in excellent agreement with the dominant elastic solution, which is shown by the solid line in the figure. Also, the angular distribution of stresses within the crack tip elements compared closely with the analytical solution.

The plastic zone at the end of the stationary load history is shown in nondimensional coordinates in Fig. 2.20. This compares very well, in overall features, with the plastic zone obtained in the earlier analysis (Fig. 2.3). The maximum plastic zone extent is about $r_p = 0.28(K_I/\sigma_0)^2$ ahead of the crack tip. In the subelements nearest to the crack tip, yielding spread only from $\theta = 0$ to 75°, which is in approximate agreement with the centered fan region of Fig. 2.2.

The radial stress distribution ahead of the crack tip within the plastic zone also

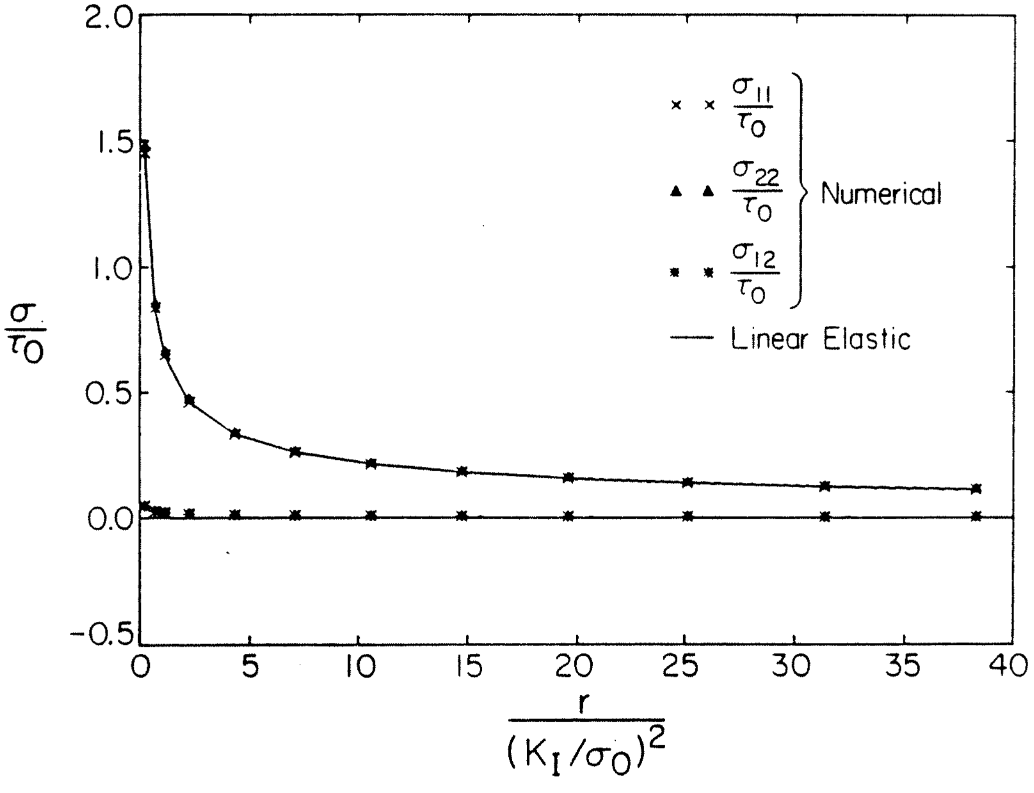

Figure 2.19. *Radial distribution of stresses ahead of crack tip at incipient yielding. Solid line is the singular elastic solution.*

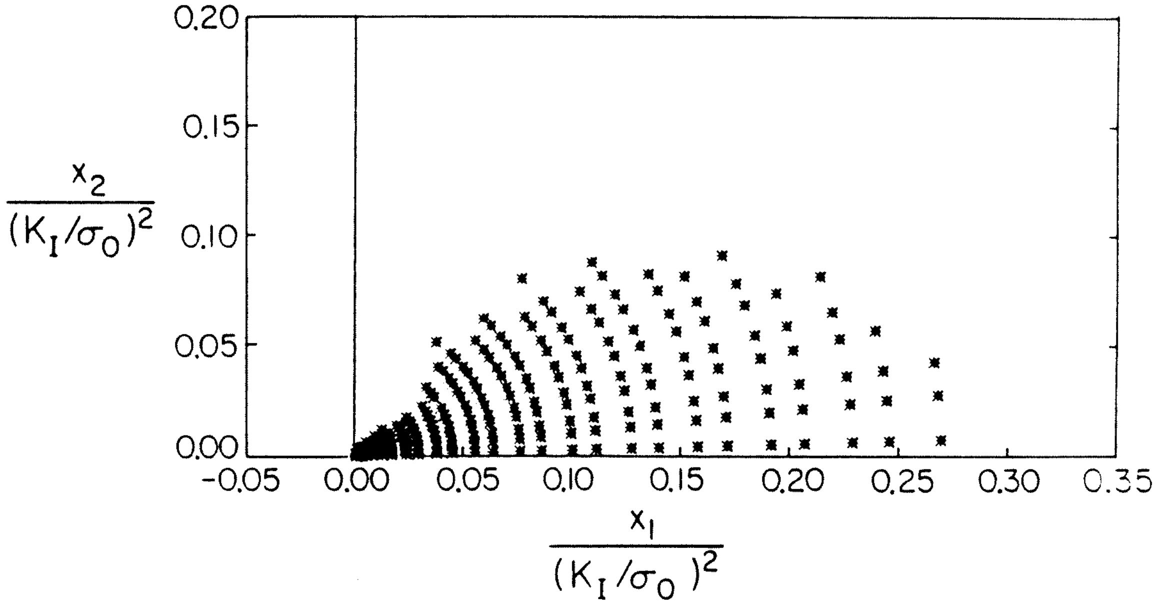

Figure 2.20. *Plastic zone for the perfectly plastic case obtained from the singular finite element analysis.*

appeared similar to the variation reported earlier in Fig. 2.6. In the subelement nearest to the crack tip that occupies the angular range from $\theta = 0$ to 7.5°, the stresses σ_{11} and σ_{22} reached the constant values $0.99\tau_0$ and $1.999\tau_0$, respectively, which agrees very well with the analytical asymptotic limit (2.3.7). Once again, a strong radial variation in the σ_{11} stress component was observed along the $\theta = 0$ ray, with a value at the elastic-plastic boundary of $1.40\tau_0$.

The angular distribution of the normalized stress component $\sigma_{\theta\theta}/\tau_0$, within the subelements nearest to the tip, is shown in Fig. 2.21 along with the slip line solution (solid line) of Hutchinson [2.9]. The finite element solution shows good agreement with the analytical distribution in the angular range $0 < \theta < 80°$, which corresponds to the centered fan region in Fig. 2.2. This was typical of the other two stress components $\sigma_{r\theta}$ and σ_{rr} as well, with σ_{rr} showing more deviation from the analytical solution as $\theta \rightarrow 80°$. This result is consistent with the fact that the two constant stress sectors in Fig. 2.2 were not detected by the finite element solution. Also, the numerical result suggests that within the fan, the focussing of the slip lines may occur very close to the crack tip in the angular range $65° < \theta < 80°$.

The normalized crack tip opening displacement $\delta_t/(J/\sigma_0)$, where J is the remotely applied value of the J integral, was calculated based on the crack tip node lying on the $\theta = \pi$ ray. It increased from zero at incipient yield ($K_I = K_I^\circ$) to a constant value of 0.84 at $K_I \approx 3.5K_I^\circ$. This value did not change during the subsequent part of the loading process. The variation in $\delta_t/(J/\sigma_0)$ during the initial phase of the loading process occurred since the plastic zone was not fully developed. It should be noted that this quantity is in excellent agreement with the value reported in Table 2.1, which was calculated on the basis of the earlier analysis.

The displacements of the crack tip nodes were substituted into Eqn.(2.6.5), with $\psi = 0$ (corresponding the mean angle of the near-tip element), to determine

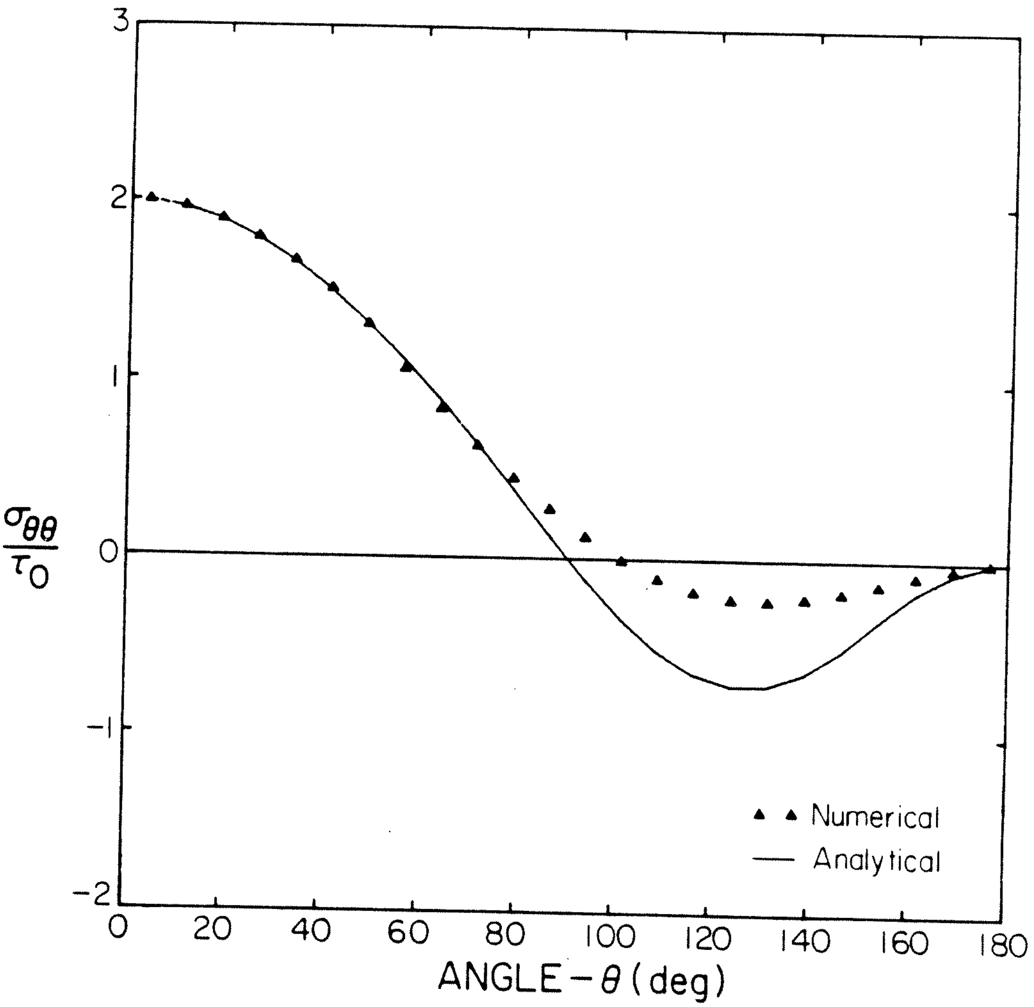

Figure 2.21. *Angular distribution of* $\sigma_{\theta\theta}/\tau_0$ *within sub-elements closest to the crack tip at the end of the loading process. Solid line is the analytical, asymptotic solution [2.9].*

the angular factors $\hat{\epsilon}^p_{\theta\theta}(\theta)$ and $\hat{\epsilon}^p_{r\theta}(\theta)$ of the dominant 1/r strain singularity (2.3.9). In order to compare with the dimensionless angular factors $\tilde{\epsilon}^p_{ij}(\theta, n)$ given by the HRR analysis (Eqn.(2.3.1)) for large n, we normalized the functions $\hat{\epsilon}^p_{\theta\theta}(\theta)$ and $\hat{\epsilon}^p_{r\theta}(\theta)$ obtained from the present finite element calculation for the perfectly plastic case as follows,

$$\left.\begin{aligned} \tilde{\epsilon}^p_{\theta\theta}(\theta) &= \frac{\hat{\epsilon}^p_{\theta\theta}(\theta)}{(K_I/\sigma_0)^2} I_n \\ \tilde{\epsilon}^p_{r\theta}(\theta) &= \frac{\hat{\epsilon}^p_{r\theta}(\theta)}{(K_I/\sigma_0)^2} I_n \end{aligned}\right\} . \tag{2.6.6}$$

Here I_n is taken as 2.6 corresponding to n → ∞ in the HRR solution. The functions thus obtained are shown along with the HRR distribution for n=25 (which is given in [2.14]) in Fig. 2.22. It can be seen that the two angular functions are completely different. It is interesting to note that the numerical solution for the perfectly plastic case under small-scale yielding conditions gives vanishingly small values for the angular factors of the dominant $\frac{1}{r}$ strain singularity for $\theta > 45°$, although the slip line solution of Fig. 2.2 shows a centered fan extending from $\theta = 0$ to about 80°.

It is found that the angular factors $\hat{\epsilon}^p_{\theta\theta}$ and $\hat{\epsilon}^p_{r\theta}$, obtained from the numerical solution, satisfy almost exactly the following relation,

$$\hat{\epsilon}^p_{r\theta}(\theta) = \hat{\epsilon}^p_{\theta\theta}(\theta)\frac{\sin\theta}{\cos\theta} , \tag{2.6.7}$$

which is analogous to Eqn.(2.3.11), as applied to the accumulated near-tip plastic strains. Also, as was observed from the near-tip strain distribution (Fig. 2.9) of the earlier analysis, it is again found from the present computation (Fig. 2.22) that $\tilde{\epsilon}^p_{\theta\theta}(\theta = 0)$ for the perfectly plastic case is about 3.3 times the corresponding value given by the HRR analysis for large n.

The near-tip value of the J integral was calculated by substituting $\hat{\epsilon}^p_{\theta\theta}(\theta)$ and $\hat{\epsilon}^p_{r\theta}(\theta)$ obtained above into Eqn.(2.3.15). The integral in (2.3.15) was estimated

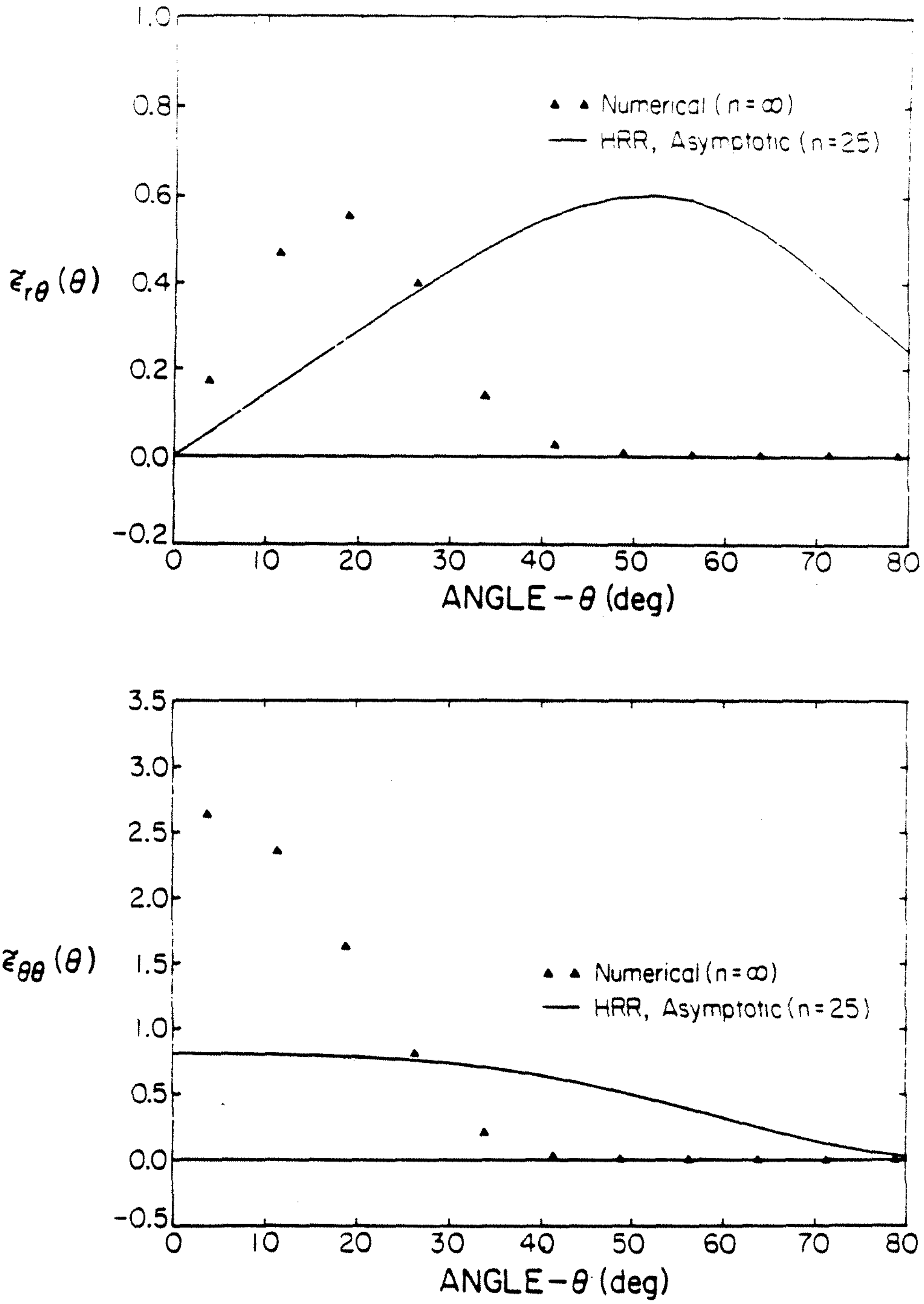

Figure 2.22. *The angular factors of the 1/r plastic strain singularity obtained from the numerical solution on the basis of the non-unique crack tip displacement. Solid line is the variation given by the HRR solution for n=25 [2.14].*

numerically, and it was found that J_{tip} is about 0.95 times the remotely applied J value. This is somewhat different from the development in plane strain where Tracey [2.16] reported J_{tip} to be about 0.8 times the applied J value. But later, Shih [2.19] found J_{tip} to be 0.96 times the applied J from his finite element calculation under plane strain, small-scale yielding conditions for the perfectly plastic case based on a different type of singular element.

If the near-tip J computed above from the present analysis is used to normalize the crack tip displacement δ_t, it is found that $\delta_t = 0.88(J_{tip}/\sigma_0)$. Hence, it is concluded that $\delta_t/(J/\sigma_0)$ for the perfectly plastic case under plane stress, small-scale yielding conditions could vary from 0.84-0.88.

In closing, it is observed that all the results given above by the present accurate numerical computation are in good agreement, in every respect, with the earlier analysis, which employed a nonfocussing mesh with nonsingular elements near the crack tip. The earlier analysis relied purely on the fineness of the mesh and a large plastic zone to the smallest element size ratio to provide sufficient resolution near the crack tip.

CHAPTER REFERENCES

2.1. Rice, J. R. (1968), "Mathematical Analysis in Mechanics of Fracture," *Fracture: An Advanced Treatise*, H. Liebowitz ed. , Academic Press, New York, Vol. 2, pp. 191-311.

2.2. Rice, J. R. and Tracey, D. M. (1973), "Computational Fracture Mechanics," *Numerical Methods in Structural Mechanics*, S. J. Fenves ed. , Academic Press, New York, pp. 585-623.

2.3. Nagtegaal, J. C. , Parks, D. M. , and Rice, J. R. (1974), "On Numerically Accurate Finite Element Solutions in the Fully Plastic Range," *Computer Methods* *in Applied Mechanics and Engineering*, Vol. 4, 153-177.

2.4. Bathe, K. J. , Snyder, M. D. , Cimento, A. P. and Rolph, W. D. (1980), "On Some Current Procedures and Difficulties in Finite Element Analysis of Elastic-Plastic Response," *Computers and Structures*, Vol. 12, 607-624.

2.5. Bathe, K. J. and Cimento, A. P. (1980), "Some Practical Procedures for the Solution of Nonlinear Finite Element Equations," *Computer Methods in Applied Mechanics and Engineering*, Vol. 22, 59-85.

2.6. Bathe, K. J. (1982), *Finite Element Procedures in Engineering Analysis*, Prentice Hall, Englewood Cliffs, New Jersey.

2.7. Schreyer, H. L. , Kulak, R. F. and Kramer, J. M. (1979), "Accurate Numerical Solutions for Elastic-Plastic Models," *Journal of Pressure Vessel Technology*, Vol. 101, 226-234.

2.8. Hutchinson, J. W. (1968), "Singular Behaviour at the End of a Tensile Crack in a Hardening Material," *Journal of Mechanics and Physics of Solids*, Vol. 16, 13-31.

2.9. Hutchinson, J. W. (1968), "Plastic Stress and Strain Fields at a Cracktip," *Journal of Mechanics and Physics of Solids*, Vol. 16, 337-347.

2.10. Rice, J. R. and Rosengren, G. F. (1968), "Plane Strain Deformation near a Cracktip in a Power law Hardening Material," *Journal of Mechanics and Physics of Solids*, Vol. 16, 1-12.

2.11. Hill, R. (1983), *The Mathematical Theory of Plasticity*, Clarendon Press, Oxford, Paperback.

2.12. Rice, J. R. (1968), "A Path Independent Integral and the Approximate Analysis of Notches and Cracks," *Journal of Applied Mechanics*, Vol. 35, 379-386.

2.13. Levy, N. , Marcal, P. V. , Ostergren, W. J. and Rice, J. R. (1971), "Small-Scale yielding near a Crack in Plane Strain: A Finite Element Analysis," *International Journal of Fracture Mechanics*, Vol. 7, 143-156.

2.14. Shih, C. F. (1973), "Elastic-Plastic Analysis of Combined Mode Fracture Problems," Ph. D. dissertation, Harvard University.

2.15. Tada, H. , Paris, P. and Irwin, G. (1973), *The Stress Analysis of Cracks Handbook*, Del Research Corporation, Hellertown, PA.

2.16. Tracey, D. M. (1976), "Finite Element Solutions for Crack-Tip Behaviour in Small-Scale Yielding," *Journal of Engineering Materials and Technology*, Transactions of ASME, Vol. 98, 146-151.

2.17. Rosakis, A. J. , Ma, C. C. and Freund, L. B. (1983), "Analysis of the Optical Shadow Spot Method for a Tensile Crack in a Power Law Hardening Material," *Journal of Applied Mechanics*, Vol. 50, 777-782.

2.18. Knowles, J. K. (1977), "The Finite Anti-Plane Shear Field near the Tip of a Crack for a Class of Incompressible Elastic Solids," *International Journal of Fracture*, Vol. 13, 611-639.

2.19. Shih, C. F. (1981), "Relationships between the J Integral and Crack Opening Displacement for Stationary Cracks," *Journal of Mechanics and Physics of Solids*, Vol. 29, 305-326.

2.20. Beinert, J. and Kalthoff, J. F. (1981), "Experimental Determination of Dynamic Stress Intensity Factors by the Method of Shadow Patterns," *Mechanics of Fracture*, G. Sih ed. , Sijthoff and Noordhoff, Vol. VII.

2.21. Rosakis, A. J. and Zehnder, A. T. (1985), "On the Method of Caustics: An Exact Analysis based on Geometrical Optics," *Journal of Elasticity*, Vol. 15, 347-367.

2.22. Rosakis, A. J. and Freund, L. B. (1982), "Optical Measurement of the Plastic Strain Concentration at a Cracktip in a Ductile Steel Plate," *Journal of Engineering Materials and Technology*, Transactions of ASME, Vol. 104, 115-120.

2.23. Zehnder, A. T. , Rosakis, A. J. and Narasimhan, R. (1986), "Measurement of J Integral with Caustics: An Experimental and Numerical Investigation," Caltech Report SM 86-8.

2.24. Hinton, E. and Campbell, J. S. (1974), "Local and Global Smoothing of Discontinuous Finite Element Functions using a Least Squares Method," *International Journal of Numerical Methods in Engineering*, Vol. 8, 461-480.

2.25. Begley, J. A. and Landes, J. D. (1972), "The J Integral as a Fracture Criterion," *Fracture Toughness*, ASTM STP 514, Philadelphia, pp. 1-23.

2.26. Landes, J. D. and Begley, J. A. (1972), "The Effect of Specimen Geometry on J_{IC}," *Fracture Toughness*, ASTM STP 514, Philadelphia, pp. 24-39.

2.27. McMeeking, R. M. (1977), "Finite Deformation Analysis of Crack Tip Opening in Elastic-Plastic Materials and Implications for Fracture," *Journal of Mechanics and Physics of Solids*, Vol. 25, 357-381.

2.28. Shih, C. F. and German, M. D. (1981), "Requirements for a One Parameter Characterization of Crack Tip Fields by the HRR Singularity," *International Journal of Fracture*, Vol. 17, 27-43.

2.29. McMeeking, R. M. and Parks, D. M. (1979), "On Criteria for J Dominance of Crack Tip Fields in Large Scale Yielding," *Elastic Plastic Fracture*, ASTM STP 668, pp. 175-194.

2.30. Hilton, P. D. and Hutchinson, J. W. (1971), "Plastic Intensity Factors for Cracked Plates," *Engineering Fracture Mechanics*, Vol. 3, 435-451.

2.31. Theocaris, P. S. and Gdoutos, E. E. (1972), "An Optical Method for Determining Opening-Mode and Edge-Mode Stress Intensity Factors," *Journal of Applied Mechanics*, Vol. 39, 91-97.

CHAPTER III

STABLE PLANE STRESS CRACK GROWTH IN ELASTIC-PERFECTLY PLASTIC SOLIDS

3.1 INTRODUCTION

A slow, stable crack extension phase is often observed [3.25-3.28] in elastic-plastic materials prior to catastrophic failure during which a steady increase in applied load is required to propagate the crack. The primary reason for this is the reduced singularity in the strains that results when the crack propagates into material that has already deformed plastically. Unlike the case of elastic materials, a complete refocussing of the strains at the tip of the extended crack is prevented in elastic-plastic materials, due to the permanence of plastic deformation.

Several investigators have contributed in providing an understanding of the mechanics and the practical implications of stable crack growth by using both analytical and numerical techniques. Problems that have received wide attention are crack extension in elastic-perfectly plastic materials under the conditions of anti-plane shear and Mode I plane strain. Chitaley and McClintock [3.19] constructed an asymptotic analytical solution for steady, quasi-static crack growth under anti-plane shear conditions. Following preliminary investigations by Rice [3.1,3.7], Rice et al.[3.3] assembled an asymptotic solution for cracks growing in an incompressible elastic-perfectly plastic material under Mode I plane strain. The solution for this problem was also found independently by Slepyan [3.23] and Gao [3.24]. Finally, the asymptotic analysis of Drugan et al.[3.4] accounted for crack growth under Mode I plane strain in elastic-perfectly plastic materials without the restriction of elastic incompressibility.

However, by contrast not many asymptotic solutions are available for cracks growing in strain-hardening materials, primarily due to the difficulty involved in the analytical treatment of the governing equations. Amazigo and Hutchinson [3.20] performed an asymptotic analysis for steady-state crack extension in a linear hardening material under anti-plane shear and Mode I plane strain and plane stress. Castañeda [3.18] has recently extended the analysis of [3.20] to include the possibility of secondary reloading and has also treated Mode II plane strain and plane stress. Nevertheless, some questions pertaining to Mode I plane strain and plane stress, in the limit as the perfect plasticity case is approached, are left unanswered by [3.18] (see for example Sec.(3.4) of the present chapter).

Finite element studies simulating crack growth, by using a nodal release procedure, were conducted by Sorensen [3.15] under anti-plane shear and by Sorensen [3.14] and Sham [3.10] under Mode I plane strain. Dean and Hutchinson [3.11] and Lam and McMeeking [3.12] have used a Eulerian finite element formulation to study steady-state crack advance in the above cases. The effects of anisotropic hardening and corner formations on the yield surface were also included in the investigations of [3.11] and [3.12].

On the other hand, remarkably little work has been performed regarding crack growth under Mode I plane stress, notwithstanding its practical importance, as, for example, to thin aircraft structures. Also, a study of plane stress crack growth is compelling, because of the possibility of direct comparison with experiments based on the optical method of caustics, which in recent years has showed great promise towards applications in ductile fracture [3.29,3.30]. A preliminary analysis has been performed by Rice [3.2], concerning the asymptotic nature of the stress and deformation fields near a growing crack tip in an elastic-perfectly plastic material under plane stress conditions. A complete (all-round) asymptotic solution for this problem has thus far remained elusive. Achenbach and Dunayevsky [3.31] have recently investigated the variation of the plastic strain field along a ray ahead of the tip, based on the assumption of the validity of the asymptotic value for the stress field [3.2] up to the elastic-plastic boundary (see Sec.(3.4) for further discussion).

As far as numerical modelling is concerned, a steady-state Eulerian finite element study has been conducted recently by Dean [3.16] for plane stress crack growth following the approach of [3.11]. However, as noted in Sec.(3.4) of this chapter, the analysis of [3.16] is not very detailed, and certain issues pertaining to the near-tip stress and deformation fields, which would provide greater insight about the underlying mechanics, have not been examined.

In the present investigation, a very detailed finite element study that provides great resolution near the crack tip, has been carried out to model stable plane stress crack growth under continuous increase in external load, by using the nodal release procedure [3.10,3.14]. Attention is restricted to elastic-perfectly plastic materials in the present analysis. This is a continuation of an earlier work [3.9] (see Chapter II), which analyzed the monotonic loading of a stationary crack under plane stress, small-scale yielding conditions.

In Sec.(3.2), the numerical technique used in [3.9] is summarized and the numerical simulation of crack growth is described. In Sec.(3.3) the results of the analytical investigations for plane strain crack growth are reviewed and the differences with plane stress are noted. In Sec.(3.4) detailed numerical results for the near-tip stress and deformation fields, plastic zone, etc. are presented and comparisons are made with existing analyses mentioned earlier. Also, stress characteristics near the crack tip are plotted from the finite element results, which could provide some clues regarding the expected nature of the analytical solution to this problem.

In Sec.(3.5) an effort is made to fit a known asymptotic form [3.2,3.3] to the numerically obtained crack profile. Also, the critical displacement criterion introduced by Rice and Sorensen [3.13] and Rice et al.[3.3] for continued crack growth is employed to predict the nature of the J resistance curves under plane stress. It is observed that stable crack growth under plane stress could be far more extensive than plane strain.

3.2 NUMERICAL ANALYSIS

Formulation

The numerical modelling of the Mode I plane stress, small scale yielding problem was discussed in detail in [3.9] (see Chapter II), where the analysis of a monotonically loaded stationary crack was performed. In the present investigation, the results obtained in [3.9] will be used as initial conditions to simulate stable crack extension. Some of the features about the numerical analysis that were described in [3.9] will be briefly outlined in this section. In the present chapter $\{\underset{\sim}{e}_1, \underset{\sim}{e}_2, \underset{\sim}{e}_3\}$ will represent an orthonormal frame centered at the crack tip and translating with it, while $\{\underset{\sim}{e}_1{}', \underset{\sim}{e}_2{}', \underset{\sim}{e}_3{}'\}$ will be a fixed orthonormal frame situated at the position of the stationary crack tip.

The upper half of a domain R containing a crack and represented entirely by finite elements is shown in Figs. 3.1*a* and *b*. The leading term in displacements of the linear elastic asymptotic solution,

$$u_\alpha = K_I \sqrt{\frac{r}{2\pi}}\, \widehat{u}_\alpha(\theta)\,, \tag{3.2.1}$$

was specified as a boundary condition on the outermost contour S of the domain.[1] The loading was applied through the Mode I stress intensity factor K_I or equivalently through the far-field value of the J integral. All plastic deformation was contained within a distance from the crack tip, which was less than $\frac{1}{30}$ of the radius of S.

---

[1] Throughout this chapter, Greek subscripts will have range 1,2, while Latin subscripts will take values 1,2,3.

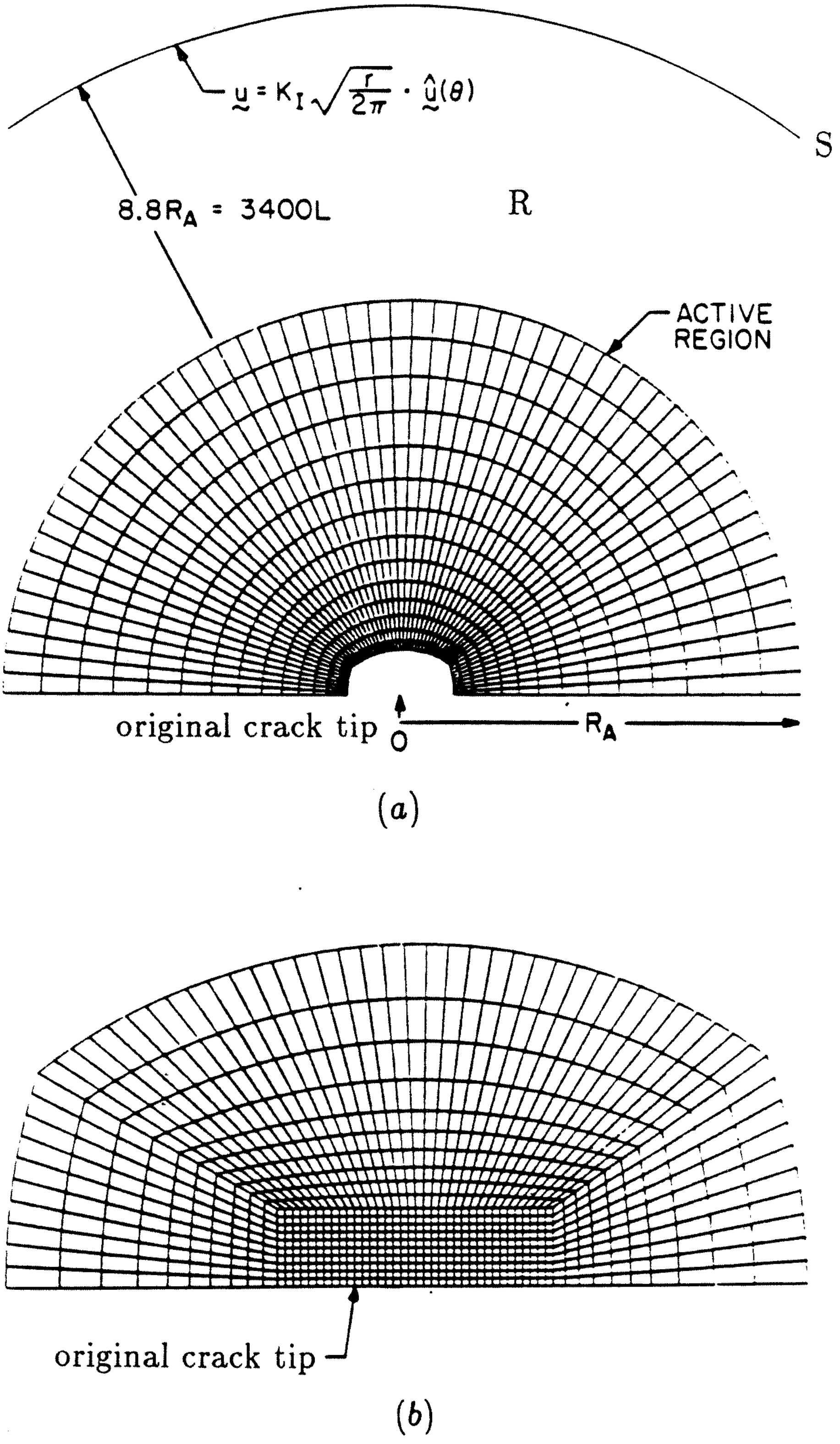

Figure 3.1. *Finite element mesh:* a) *Outer mesh* b) *Fine mesh near the crack tip.*

The active region of Fig. 3.1*a* has a total of 1704 four noded quadrilateral elements and 3549 degrees of freedom. The quadrilaterals were formed from four constant strain triangles with static condensation of the internal node. Static condensation was also employed in the large region surrounding the active mesh, which always remained elastic. The cutout of Fig. 3.1*a*, which is a fine mesh region near the crack tip, is shown in detail in Fig. 3.1*b*. The small square elements near the crack tip have a size L, which is about $\frac{1}{385}$ of the radius R_A of the active region and about $\frac{1}{3400}$ of the radius of S.

Constitutive Assumptions

The material model that was considered here was that of an isotropic elastic-perfectly plastic solid. A small strain incremental plasticity theory was employed along with the Huber-Von Mises yield condition and the associated flow rule. The total strain rate tensor is assumed to be decomposed into elastic and plastic parts, and the constitutive law for material currently experiencing plastic deformation is given by [3.9],

$$\dot{\sigma}_{ij} = C^{*}_{ijkl}\dot{\epsilon}_{kl} = \left[C_{ijkl} - \frac{C_{ijpq}S_{pq}S_{mn}C_{mnkl}}{S_{rt}C_{rtuv}S_{uv}} \right] \dot{\epsilon}_{kl} \ . \qquad (3.2.2)$$

Here C_{ijkl} is the isotropic, positive definite elasticity tensor, and S_{ij} is the deviatoric stress tensor. In the present analysis, the yield criterion and the constitutive law (3.2.2) were used along with the plane stress condition,

$$\sigma_{3i} \equiv 0 \ . \qquad (3.2.3)$$

On using Eqn.(3.2.3) in Eqn.(3.2.2) a constraint for $\dot{\epsilon}_{33}$ in terms of $\dot{\epsilon}_{\alpha\beta}$ can be obtained. The ratio of the Young's modulus to the yield stress in pure shear (E/τ_0) was taken as 350 and the Poisson's ratio (ν) as 0.3 in the computation.

Finite Element Scheme

A displacement based finite element method was employed and inertia effects were neglected in the analysis. The incremental finite element equilibrium equations were derived from the principle of virtual work by linearization [3.21]. These equations were solved for each time step using the iterative Newton-Raphson method which is summarized in Appendix A. An explicit integration procedure also known as the Tangential Predictor-Radial Return method was employed together with subincrementation to integrate the incremental stress-strain law. (See Appendix A for details.)

Solution Strategy

The plastic zone at the end of the stationary load history in [3.9] had a maximum extent, which occurred ahead of the crack tip, of about 100 times the smallest element size L. Subsequently, twenty one-element crack growth steps were simulated using the nodal release procedure [3.10,3.15], as described below. The stiff spring that was attached to the crack tip node in the x_2 direction, in order to enforce the symmetry condition ($u_2 = 0$), was removed and was replaced by the point load acting on it. This point load was subsequently relaxed to zero in twenty increments, at the end of which a traction-free element surface emerged, and the crack advanced by one element length L.

The externally applied load through the far-field J integral (or $\mathrm{K_I}$) was increased simultaneously during the above nodal release procedure (as in [3.10]), in order to model stable crack extension in a continuous manner. For this purpose, a simple J versus crack growth (Δa) history with a constant slope as shown in Fig. 3.2 was used. In this figure, the value of J has been made dimensionless by the amount $\mathrm{J_I}$, which caused incipient yielding in the element nearest to the crack tip during the monotonic loading of the stationary crack [3.9]. Also, $\mathrm{T} \equiv \frac{\mathrm{E}}{\sigma_0^2} \frac{\mathrm{dJ}}{\mathrm{da}}$ is

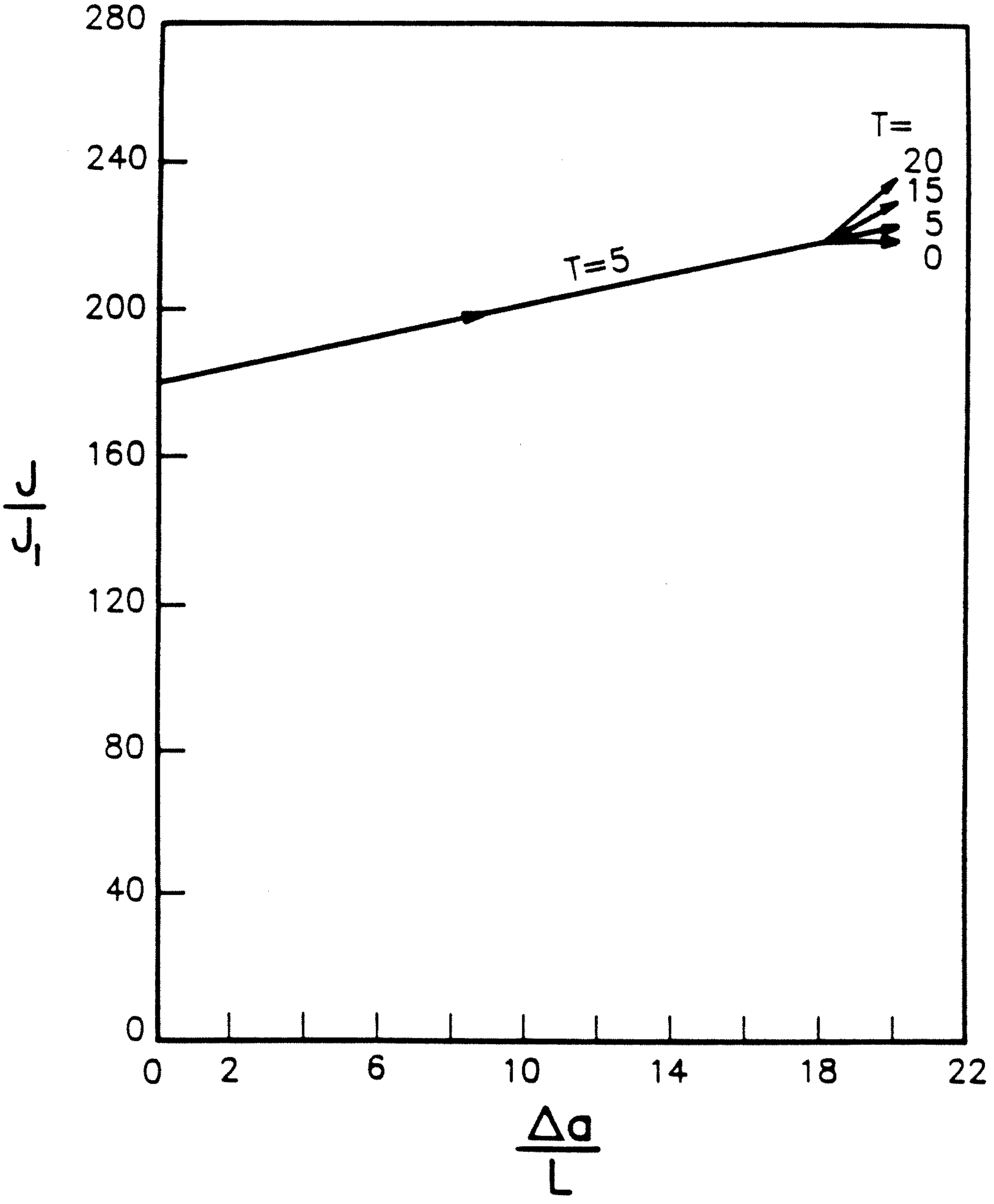

Figure 3.2. *J versus crack growth history.*

the nondimensional Paris tearing modulus. Following eighteen one-element crack growth steps at T=5, two crack growth steps at four different T values of 0, 5, 15 and 20 were simulated. The last two steps were thus carried out in order to study the effect of different rates of increase of external load on crack displacement increment, as will be discussed in Sec.(3.5).

3.3 ASYMPTOTIC FIELDS NEAR PROPAGATING CRACK TIPS

General Considerations

For elastic-perfectly plastic materials the following assumptions are often made [3.1-3.4] about the asymptotic nature of the stress field,

$$\left.\begin{aligned} \sigma_{ij}(r,\theta) &\sim \sigma^{\circ}_{ij}(\theta) \\ \frac{\partial \sigma_{ij}(r,\theta)}{\partial \theta} &\sim \sigma'_{ij}(\theta) = \frac{d\sigma^{\circ}_{ij}}{d\theta} \\ r\frac{\partial \sigma_{ij}}{\partial r} &\sim o(1) \end{aligned}\right\} , \qquad r \to 0 \, . \tag{3.3.1}$$

Asymptotic forms of equilibrium equations and yield condition can be obtained by using the assumption (3.3.1). These in turn can be employed to ascertain the types of plastic sectors which compose the near-tip deformation field.

The asymptotic stress distribution $\sigma^{\circ}_{ij}(\theta)$ within these sectors can be derived completely except for some unknown constants [3.2]. These may be determined when an all-round asymptotic solution is sought by assembling plastic and elastic unloading sectors appropriately satisfying continuity conditions [3.5,3.6], boundary conditions and material stability postulates. A detailed discussion of the continuity conditions across quasi-statically propagating surfaces in elastic-plastic solids under plane stress [3.6] is presented in Appendix C. The movement of the asymptotic stress field through the material with the advancing crack tip induces an elastic strain increment that is incompatible. Thus, a plastic strain increment is induced as well. Rice [3.1] demonstrated that the associated displacement increments (or material particle velocities) have a log(r) singularity as the crack tip is approached.

Plane Strain

Rice et al.[3.3] assembled a near-tip solution for quasi-static crack advance under plane strain in an incompressible material ($\nu = 0.5$). This solution is essentially the Prandtl field [3.7] together with an elastic unloading sector following the centered fan. This was added to eliminate the negative plastic work that would otherwise occur at the trailing boundary of the fan. The asymptotic form of the deformation rates within the fan is summarized below [3.2],

$$\left.\begin{aligned} v_r &\sim (5-4\nu)\frac{\tau_0}{E}\dot{a}\sin\theta\ln\left(\frac{\bar{R}}{r}\right) \\ v_\theta &\sim -(5-4\nu)\frac{\tau_0}{E}\dot{a}\left[\frac{1}{\sqrt{2}}-\cos\theta\right]\ln\left(\frac{\bar{R}}{r}\right) \\ D^p_{r\theta} &\sim \frac{(5-4\nu)}{\sqrt{2}}\frac{\tau_0}{E}\frac{\dot{a}}{2r}\ln\left(\frac{\bar{R}}{r}\right) \end{aligned}\right\}, \qquad r \to 0 . \tag{3.3.2}$$

Here v_r and v_θ are the material particle velocities and D^p_{ij} is the plastic part of the strain rate tensor. Also, $\dot{a}$ is the crack velocity and $\bar{R}$ is an arbitrary length scale which is undetermined from the asymptotic analysis. The asymptotic form of the plastic strains is given by,

$$\epsilon^p_{\alpha\beta} \sim \frac{(5-4\nu)}{2\sqrt{2}}\frac{\tau_0}{E}G_{\alpha\beta}(\theta)\ln\left(\frac{\bar{R}}{r}\right), \qquad r \to 0 . \tag{3.3.3}$$

The angular factors $G_{\alpha\beta}(\theta)$ are fully determined from an asymptotic angular integration of $D^p_{\alpha\beta}$ [3.2,3.4]. It should be noted that the dominant log(r) term of (3.3.3) is much weaker than the 1/r plastic strain singularity near a monotonically loaded stationary crack tip [3.7].

Motivated by the above, Rice et al.[3.3] proposed the following form for the near-tip crack opening rate during stable plane strain crack advance,

$$\dot{\delta} \sim \frac{\alpha\dot{J}}{\sigma_0} + \beta\frac{\sigma_0}{E}\dot{a}\ln\left(\frac{R}{r}\right), \qquad r \to 0 . \tag{3.3.4}$$

In the above equation, α and β are constants and R is a length dimension, which is expected to scale with the plastic zone size under small-scale yielding conditions, so that

$$R = s\left(\frac{EJ}{\sigma_0^2}\right) . \tag{3.3.5}$$

Here J is the remotely applied value of the J integral which under small scale yielding conditions is given by,

$$\begin{aligned} J &= (1-\nu^2)\frac{K_I^2}{E} \qquad (plane\ strain) \\ &= \frac{K_I^2}{E} \qquad (plane\ stress)\ . \end{aligned} \tag{3.3.6}$$

The constant β in (3.3.4) can be obtained from an all-round asymptotic solution [3.3,3.4], whereas the constants α in (3.3.4) and s in (3.3.5) are undetermined from the asymptotic analysis.

The second term in (3.3.4) arises because of the log(r) dominant singularity in the material particle velocities. The first term in (3.3.4) encompasses the assumption that the higher-order terms in velocities are bounded and linear in load rate ($\dot{J}$ for small scale yielding). Also, for $\dot{a} = 0$, the right hand side of (3.3.4) reduces to the correct expression for the discrete crack opening rate that is observed during the monotonic loading of a stationary crack [3.7]. An asymptotic integration of (3.3.4) can be carried out to obtain the near-tip crack opening displacement during stable crack growth (when crack length a increases continuously with J) as follows,

$$\delta \sim \frac{\alpha r}{\sigma_0}\frac{dJ}{da} + \beta r\frac{\sigma_0}{E}\ln\left(\frac{eR}{r}\right), \qquad r \to 0\,, \tag{3.3.7}$$

where e is the base of the natural logarithm. As opposed to the monotonic loading of a stationary crack, Eqn.(3.3.7) implies that the opening displacement at the crack tip is equal to zero during crack growth. However, as can be noticed from (3.3.7), the crack profile during growth exhibits a vertical tangent at the tip.

Plane Stress

The general features outlined above for plane strain apply to plane stress as well, with some modifications. No all-round asymptotic solution that satisfies all the boundary and symmetry conditions and that does not violate material stability postulates has yet been assembled for this case. However, Rice [3.2] has performed a preliminary asymptotic analysis and has demonstrated that only two types of plastic sectors can exist near the crack tip. These are centered fan sectors in which radial lines are stress characteristics ($s^\circ_{rr} \equiv 0$) and constant stress sectors in which the Cartesian components of stress $\sigma^\circ_{\alpha\beta}$ are constant (not functions of angle θ). The asymptotic stress and deformation fields within the above plastic sectors and in elastic unloading sectors have been derived in [3.2].

The asymptotic fields within a centered fan sector are summarized below assuming that it adjoins the $\theta = 0$ ray (similar to the stationary crack tip solution [3.8]):

$$\sigma^\circ_{rr} = \tau_0 \cos\theta \,, \qquad \sigma^\circ_{\theta\theta} = 2\tau_0 \cos\theta \,, \qquad \sigma^\circ_{r\theta} = \tau_0 \sin\theta \tag{3.3.8}$$

$$\left.\begin{aligned} v_r &\sim 3\frac{\tau_0}{E}\dot{a}\sin^2\theta \ln\left(\frac{\bar{R}}{r}\right) \\ v_\theta &\sim 3\frac{\tau_0}{E}\dot{a}F(\theta)\ln\left(\frac{\bar{R}}{r}\right) \\ D^p_{\theta\theta} &\sim 3\frac{\tau_0}{E}\frac{\dot{a}}{2r}\cot\theta(\sin 2\theta - F(\theta))\ln\left(\frac{\bar{R}}{r}\right) \\ D^p_{r\theta} &\sim 3\frac{\tau_0}{E}\frac{\dot{a}}{2r}(\sin 2\theta - F(\theta))\ln\left(\frac{\bar{R}}{r}\right) \end{aligned}\right\} , \quad r \to 0 \,, \tag{3.3.9}$$

where

$$F(\theta) = |\sin\theta|^{-1/2} \int_0^\theta (\sin\phi)^{1/2} \cos 2\phi d\phi \,. \tag{3.3.10}$$

Both $D^p_{r\theta}$ and $D^p_{\theta\theta}$ are singular as $\frac{1}{\mathrm{r}}\log(\mathrm{r})$ in plane stress, whereas only $D^p_{r\theta}$ exhibits this singularity in plane strain (Eqn.(3.3.2)). $\bar{R}$ in the above equations is an undetermined length dimension.

Rice [3.1] has demonstrated that if Eqn.(3.3.9) for the plastic strain rates D^p_{ij} is valid on the $\theta = 0$ ray, then an integration with respect to r can be carried out to obtain

$$\epsilon^p_{ij} \sim \frac{1}{2}\frac{\tau_0}{E} G_{ij} \ln^2\left(\frac{\bar{R}}{r}\right), \qquad \theta = 0, \quad r \to 0\,, \tag{3.3.11}$$

where,

$$\left.\begin{array}{ll} G_{11} = 0 & G_{12} = 0 \\ G_{22} = 2 & G_{33} = -2 \end{array}\right\} . \tag{3.3.12}$$

It should be observed that the plastic strains (on the $\theta = 0$ ray) are singular as $\log^2$(r) in plane stress, whereas in plane strain the plastic strains in the fan have a log(r) dominant singularity from (3.3.3). The stronger $\log^2$(r) dominant plastic strain singularity in plane stress (which also occurs in anti-plane shear) arises because the crack propagates into a centered fan region unlike in Mode I plane strain.

In plane stress, the material particle velocities have a log(r) singularity analogous to plane strain (see Eqns.(3.3.2) and (3.3.9)). Hence one expects the crack opening rate during stable plane stress crack advance to have the same functional form as (3.3.4). Also the Equations from (3.3.4) to (3.3.7) and the accompanying *discussions are expected to apply for stable plane stress crack growth.*

3.4 RESULTS AND DISCUSSION

Plastic Zone

The active plastic zone surrounding the crack tip is shown in Fig. 3.3*a* in moving coordinates that have been made dimensionless by the self-similar parameter $(K_I/\sigma_0)^2$. For comparison purposes, the plastic zone corresponding to a stationary crack under plane stress conditions, which was obtained in [3.9], is shown in Fig. 3.3*b*. In Fig. 3.3*a*, the current crack tip is at the origin of the coordinate system,

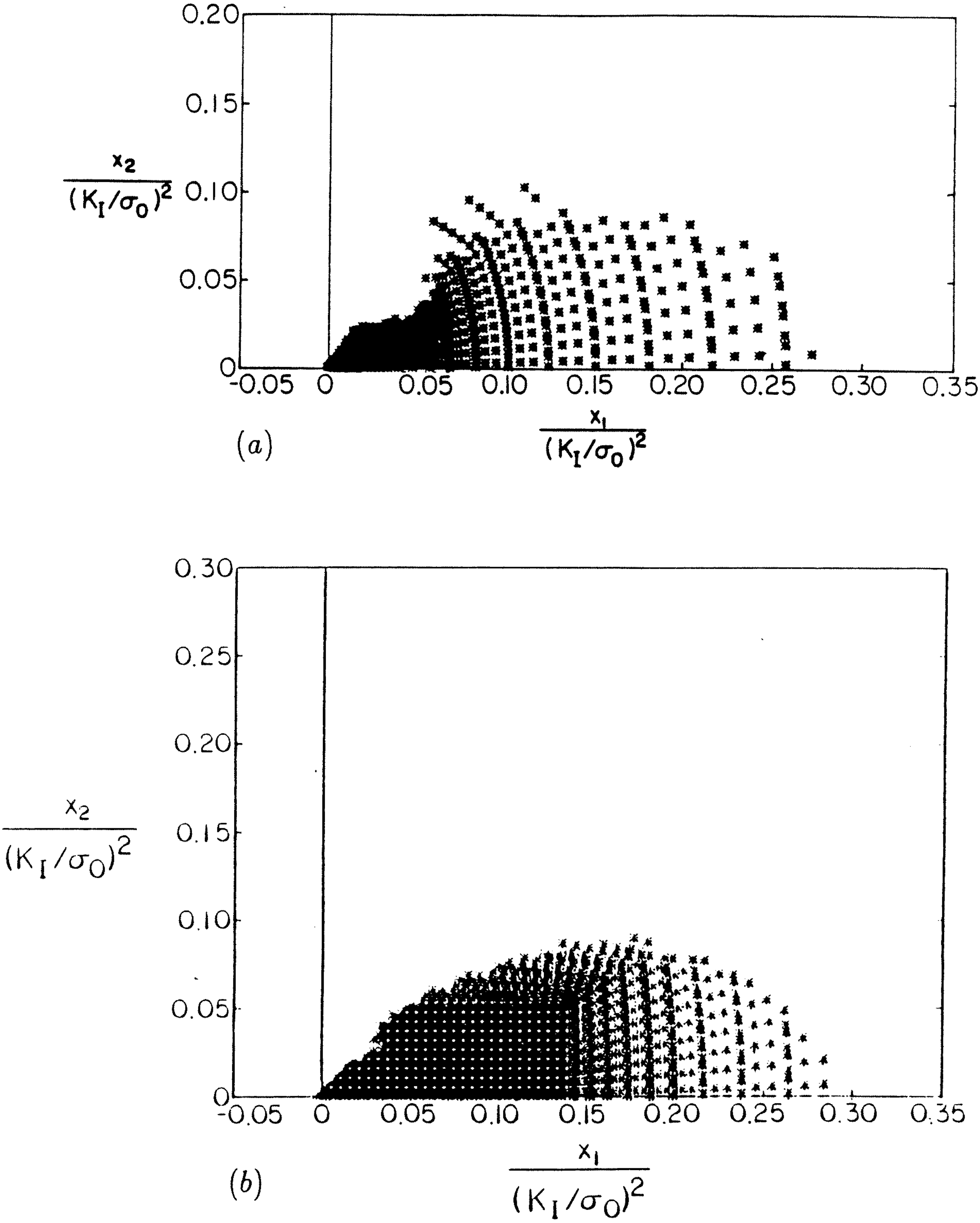

Figure 3.3. *a) Active plastic zone surrounding the propagating crack tip and b) Plastic zone corresponding to the stationary crack [3.9].*

and this result was obtained at the end of twentieth crack growth step. A point in the figure represents an actively yielding integration station (currently on the yield surface in stress space) within an element. It can be seen from the figure that a large elastic unloading region follows the active plastic zone. The active plastic zone appears to occupy an asymptotic angular extent from $\theta = 0^\circ$ to about 45°, which will be verified later.

The elements behind the active plastic zone, which are close to the crack plane and which occupy the angular range from $\theta = 45^\circ$ to 180°, have unloaded elastically. These elements have previously experienced plastic yielding during the passage of the crack tip. The present numerical solution does not exhibit any secondary (plastic) reloading along the crack flank. This is in contrast to plane strain, where a secondary plastic region was found, extending behind the moving crack tip [3.10-3.14].

As can be seen from Fig. 3.3*a*, the trailing boundary of the active plastic zone seems to have a kink, resulting in a shape similar to that observed in anti-plane shear [3.11,3.15]. The parallel between plane stress and anti-plane shear has been recognized earlier, from the presence of an intense deformation zone (centered fan) ahead of the moving tip in both cases. In the present computation, the kink in the active plastic zone developed during the first few crack growth steps and persisted with subsequent crack advance. Also, the overall features of the plastic zone did not change much after the first few crack growth steps.

The maximum radial extent of the plastic zone, which occurs directly ahead of the growing crack tip ($\theta = 0$), is $R_p \approx 0.28(K_I/\sigma_0)^2$, which is about the same as the stationary problem (Fig. 3.3*b*). Also, on comparing Figs. 3.3*a* and *b*, it can be seen that the plastic zone for the propagating crack is similar in overall shape and size to that obtained for the stationary problem at points away from the crack tip.

However near the tip the two plastic zones seem to deviate in shape, primarily due to elastic unloading behind the trailing boundary during crack growth. As pointed out by Rice [3.2], strong changes in plastic zone shape near the tip and a tendency to reestablish a shape similar to that for the stationary crack at points away from the tip are expected during the initial stages of crack growth. This can also be observed in the results for both anti-plane shear [3.15] and plane strain [3.10].

Finally, it is noted that the plastic zone of Fig. 3.3*a* compares well with the steady-state result obtained by Dean [3.16], from an Eulerian finite element formulation, except for the presence of the kink. However, the present finite element solution is more detailed, since it has a larger ratio of plastic zone to smallest element size of over 100 as compared to about 35 in Dean's computation. Also, unlike Dean's work, the initial phase of crack growth was simulated here under continuously increasing external load.

Radial Distribution of Plastic Strain

The radial distribution of normalized plastic strain, $\epsilon_{22}^{p}/\epsilon_0$, with respect to normalized distance, $r/(K_I/\sigma_0)^2$, ahead of the current crack tip is shown in Fig. 3.4. Results are presented for various levels of crack growth under steadily increasing value of far-field J at T=5. The solid line in the figure is the plastic strain distribution ahead of a monotonically loaded stationary crack tip, which was obtained in [3.9]. It can be seen that the plastic strain converges rapidly during the first few crack growth steps to an invariant distribution. For example, at a distance of $0.01(K_I/\sigma_0)^2$ ahead of the moving crack tip, the plastic strain dropped by 32% during the first five crack growth steps and by 17%, 8% and 3% during the sixth to tenth steps, eleventh to fifteenth steps and sixteenth to twentieth steps, respectively. Such rapid convergence was also observed in the numerical simulation of anti-plane shear crack growth by Sorensen [3.15].

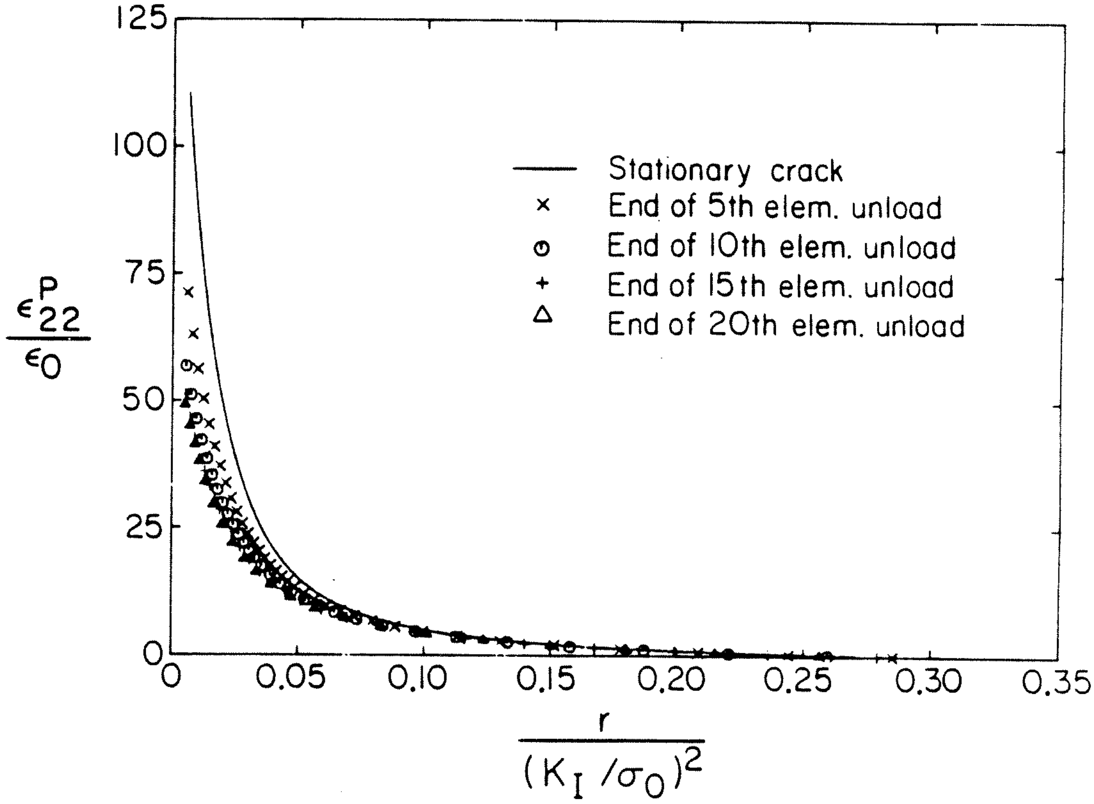

Figure 3.4. *Radial distribution of plastic strain ahead of the propagating crack tip for various levels of crack growth.*

As can be seen from Fig. 3.4, the plastic strain distribution ahead of the tip during growth exhibits a weaker singularity than in the stationary problem. This is due to the dominant $\log^2(r)$ singularity, which is expected to occur during plane stress crack growth, as compared to the $1/r$ distribution for the stationary crack. This fact is the origin for the stable crack extension phase [3.1,3.17] observed in elastic-plastic materials (preceding instability), when crack growth occurs under steadily increasing external load.

Finally, it is important to note that due to increase in external load (as in the present analysis) with crack growth, a term of order $\log(r)$ will have to be added to the leading $\log^2(r)$ term for the plastic strains ahead of the tip in (3.3.11) [3.1]. For crack growth at large values of T, this higher-order term may be important even for moderate distances from the tip, and hence the $\log^2(r)$ term may dominate only very near the tip.

Crack Profiles

The self-similar development of the crack opening profile for various levels of crack growth at $T = 5$ is shown in Fig. 3.5 in the nondimensional form $\delta/(J/\sigma_0)$ versus $x_1'/(K_I/\sigma_0)^2$. The stationary crack profile obtained in [3.9] is also plotted in the figure for comparison. As can be seen from the figure, the crack profile changes from a blunted form at the end of the stationary load history to a sharp shape during crack growth. This is because of the lessened strain concentration that results when the crack propagates into material that has already deformed plastically. In Sec.(3.5) this numerically obtained profile will be used to estimate the parameters α, β, and s in the asymptotic Equation (3.3.7).

Radial Distribution of Stresses

The radial variation of the normalized stress components, $\sigma_{\alpha\beta}/\tau_0$, versus normalized distance ahead of the crack tip at the end of the twentieth release step is

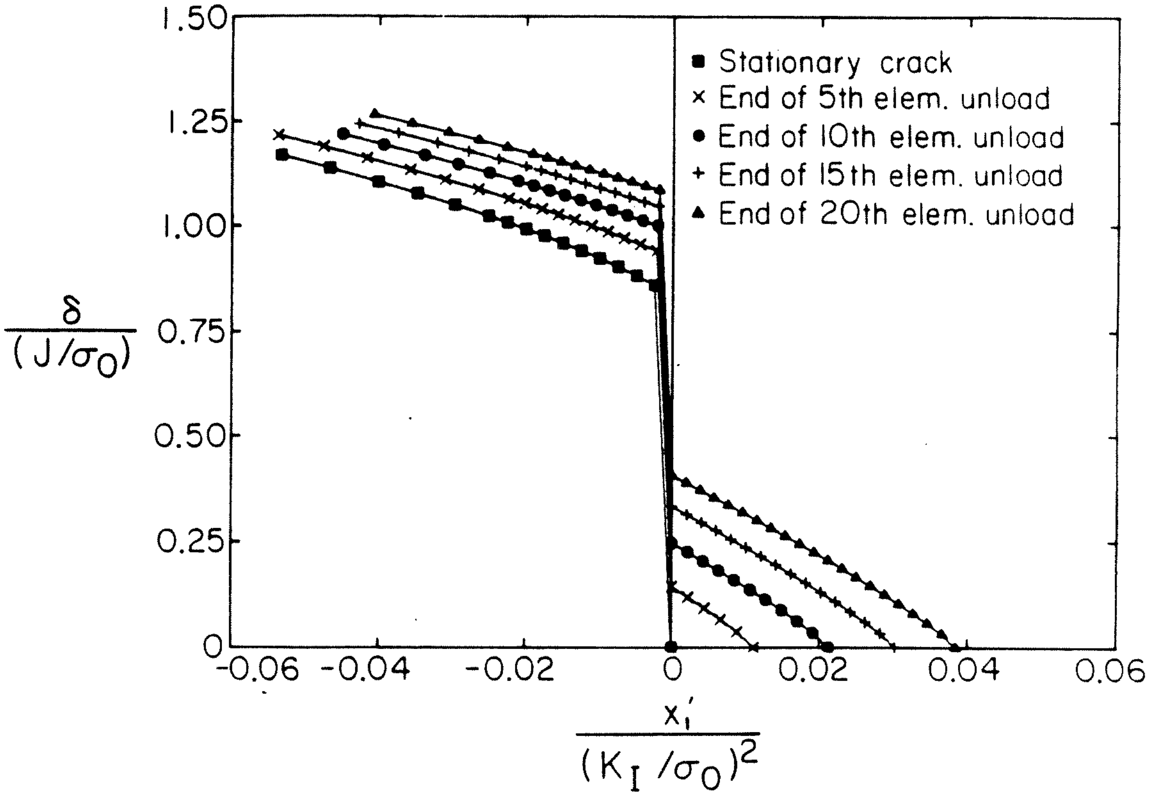

Figure 3.5. *Development of crack profile for various levels of crack growth.*

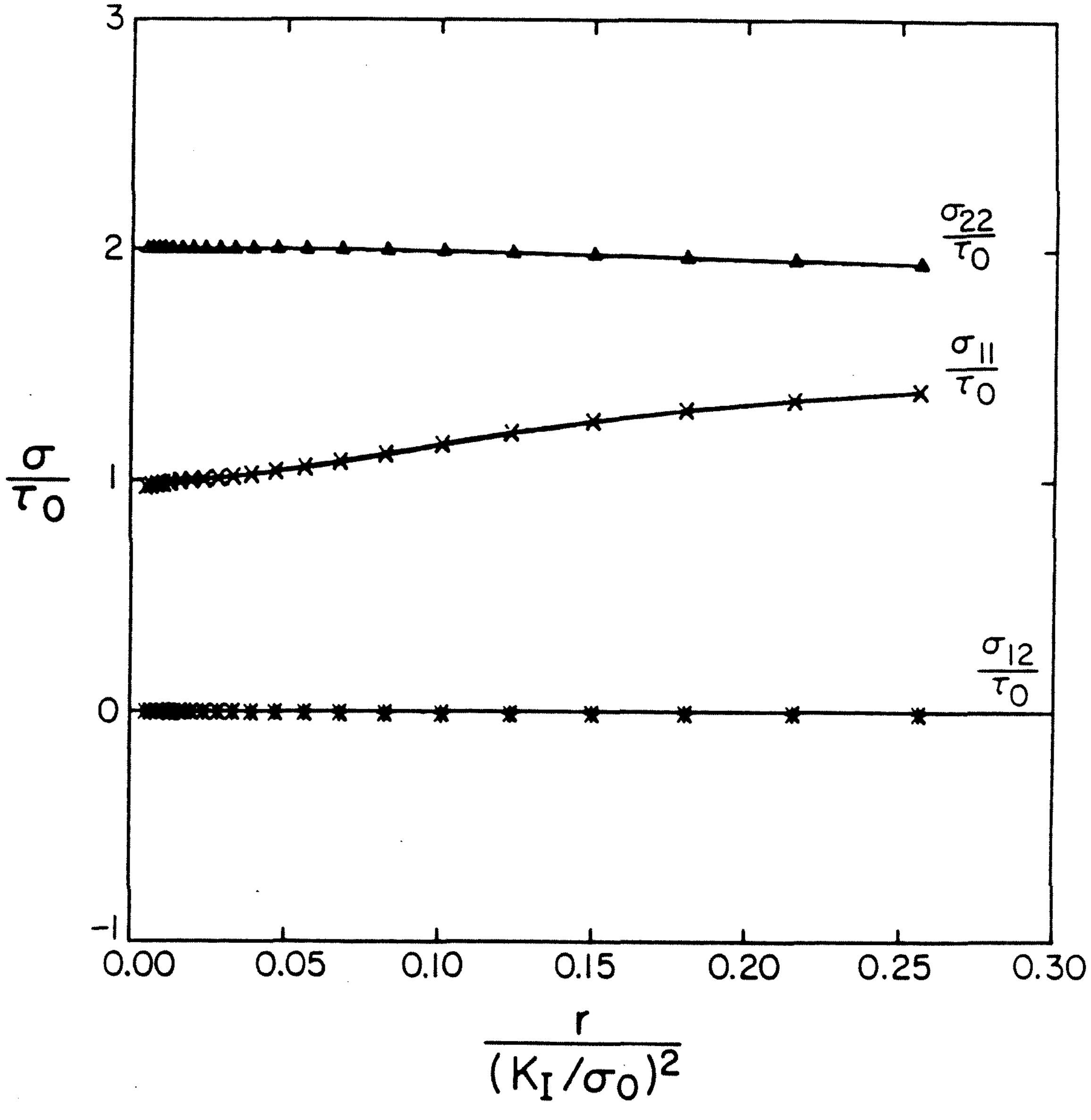

Figure 3.6. *Radial distribution of stresses ahead of moving crack tip.*

shown in Fig. 3.6. The centroidal values of stresses in the row of elements ahead of the tip have been used to construct this plot. The numerically obtained stresses very near the crack tip approach the asymptotic distribution given by Eqn.(3.3.8) which assumes that there is a centered fan ahead of the tip. For example, from the finite element results at $r = 0.01(K_I/\sigma_0)^2$, the values of σ_{11} and σ_{22} are $0.99\tau_0$ and $1.999\tau_0$, in excellent agreement with the values τ_0 and $2\tau_0$, respectively given by (3.3.8).

It can be seen from Fig. 3.6 that the σ_{11} stress component exhibits a strong radial variation with a value of $1.40\tau_0$ at the elastic-plastic boundary. The value of σ_{11} differs from the asymptotic limit by less than 5% in the range $r < 0.04(K_I/\sigma_0)^2$. This stress variation compares closely with that for the stationary crack [3.9]. As noted in [3.9], it suggests possible curving of the leading boundary of the fan at moderate distances from the tip. This will also be discussed later in connection with Fig. 3.8.

Near-tip Angular Distribution of Stresses

The angular variation of the normalized polar stress components at a distance of $0.01(K_I/\sigma_0)^2$ from the moving crack tip (which is within $.04R_p$) is shown in Fig. 3.7*a*. The centroidal values of stresses in the elements lying on a rectangular contour surrounding the moving crack tip, which is shown as an inset in the figure, have been used to construct this plot. The angular variation along the above contour of the Von Mises equivalent stress, $\sigma_{eqv} = (\frac{3}{2}s_{ij}s_{ij})^{1/2}$ which has been normalized by σ_0, is shown in Fig. 3.7*b*.

As can be seen from Fig. 3.7*b*, σ_{eqv} becomes less than σ_0 for $\theta > 45°$, which suggests that the asymptotic angular extent of the active plastic zone is about 45°. This agrees well with visual observation of Fig. 3.3*a*. However, from published results for crack advance under both anti-plane shear [3.11,3.15] and plane strain

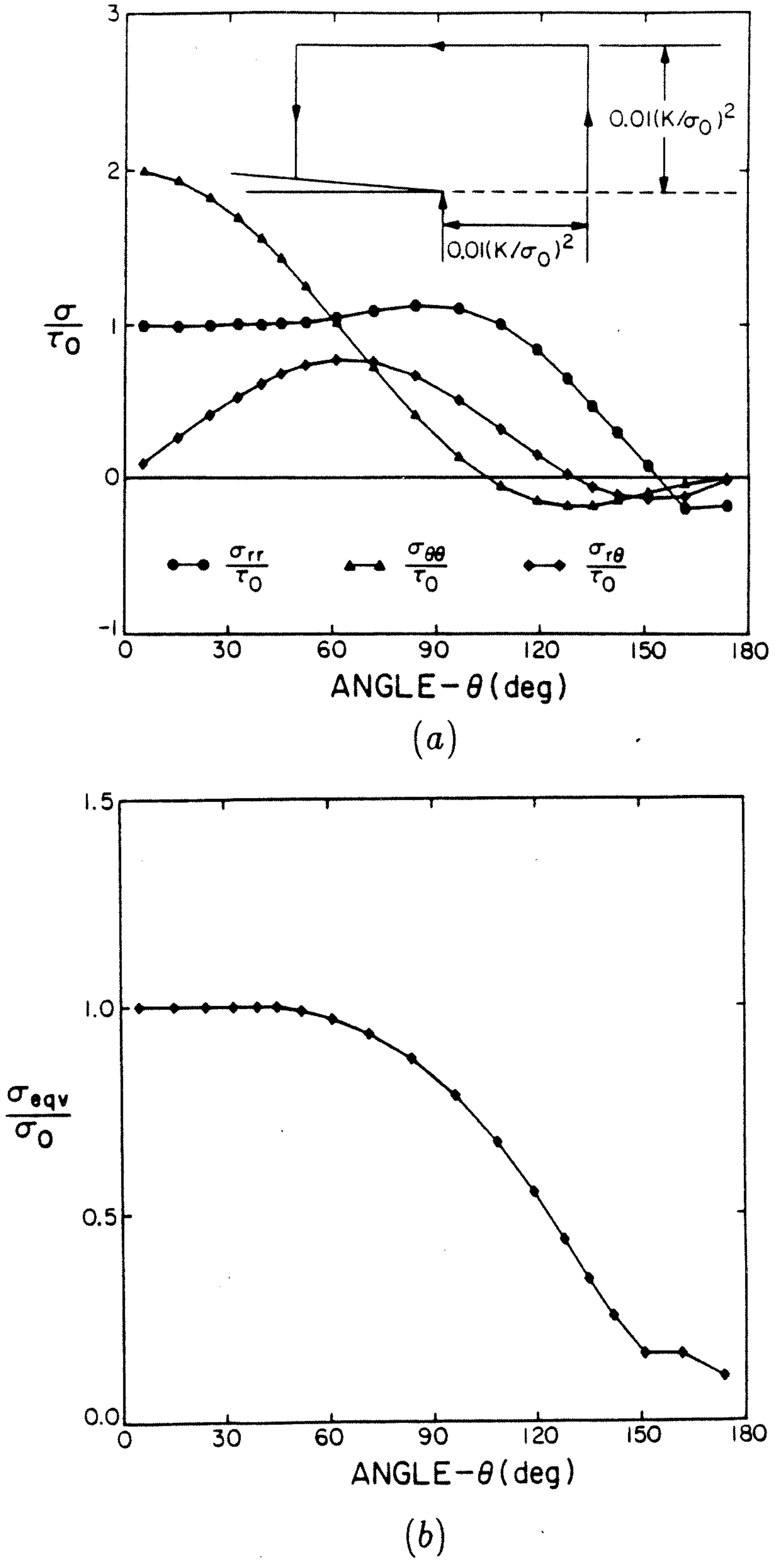

Figure 3.7. *Near-tip angular distribution of* a) *normalized polar stress components and* b) *Von Mises equivalent stress.*

[3.10], where the asymptotic angular extent of active yielding was overestimated by finite element solutions, one is led to interpret the above conclusion with some caution. Also, from Fig. 3.7*b*, it can be seen that σ_{eqv} does not become equal to σ_0 as θ approaches 180°, which implies that no secondary (plastic) reloading has been detected by this numerical solution.

The angular distribution of stresses (Fig. 3.7*a*) within the actively yielding region is in good agreement with the variation in a centered fan, as predicted by Eqn.(3.3.8). For example, in the angular range $0° \leq \theta < 45°$, the values of $\sigma_{\theta\theta}$ and $\sigma_{r\theta}$ as given in Fig. 3.7*a* differ from that obtained using Eqn.(3.3.8) by less than 1% and 4%, respectively. However, the value of σ_{rr} shown in Fig. 3.7*a* agrees with that given by Eqn.(3.3.8) to within 8% in the angular range $0° \leq \theta \leq 25°$ and deviates substantially for $25° < \theta < 45°$. The reason for this discrepancy will be explained later in this section. Also, the angular stress distribution of Fig. 3.7*a* compares quite well with the finite element results of Dean [3.16]. However, as pointed out earlier, the present computation is considered to be more detailed than Dean's analysis.

The recent asymptotic analysis of Castañeda [3.18] for steady, quasi-static crack growth in a linear hardening material is unfortunately not definitive about the asymptotic angular extent of the primary plastic zone in the limit as the perfect plasticity case is approached. He obtains a primary plastic angle of about 53.2° and 49° when the ratio E_t/E of the tangent modulus to the elastic modulus is 0.001 and 0.0001, respectively. Also the presence of a secondary reloading zone and its angular extent (which is extremely small) are not completely conclusive from his results, in the limit as E_t/E tends to zero. The prediction of a very small reloading angle is, however, not inconsistent with the present numerical results, since such a tiny reloading zone cannot possibly be detected by a finite element scheme.

Nevertheless, the angular factors $\sigma^{\circ}_{ij}(\theta)$ of the dominant r^s term for the stresses given in [3.18] for $E_t/E = 0.001$ agree closely with the present numerical solution of Fig. 3.7, except for the σ_{rr} component, which seems to deviate in the angular range from $\theta = 25°$ to about $100°$. Also, the stress distribution in [3.18] for $E_t/E = 0.001$ suggests yielding in compression for θ very close to $180°$. While the present results do indicate a region near the crack flank where σ_{rr} is negative (see Fig. 3.7), no yielding in compression has been observed.

Stress Characteristics

The two families of stress characteristics within the active plastic zone, near the propagating crack tip, are shown in Fig. 3.8, using nondimensional crack tip coordinates. The dashed line in the figure is the boundary of the active plastic zone. The characteristics were plotted using the averaged stresses within the elements, as described in Appendix B. The dotted line in the figure separates a region near the tip, in which the equations for the stresses are hyperbolic, from a region outside, in which they are elliptic. At each point on the dotted line, the condition for parabolicity of the governing equations for the stresses (See Appendix B, second of (B.2)) is satisfied. As can be seen from the figure, the two families of characteristics become mutually tangential to each other at every point along this dotted line, as it curves upwards from the $\theta = 0$ ray. However, it is not clear whether the elliptic region extends all the way upto the crack tip as a wedge of vanishingly small angular extent, as $r \to 0$ along the $\theta = 0$ ray, although there is some evidence to suggest this possibility.

Two important observations should be made from this figure. Firstly, it can be seen that a family of characteristics focusses at the crack tip in the angular range from $\theta = 0°$ to about $25°$, beyond which the characteristics seem to intersect the crack plane slightly behind the tip. This is probably because of the fact that, due to discretization, the crack tip is not precisely sensed in the finite element solution

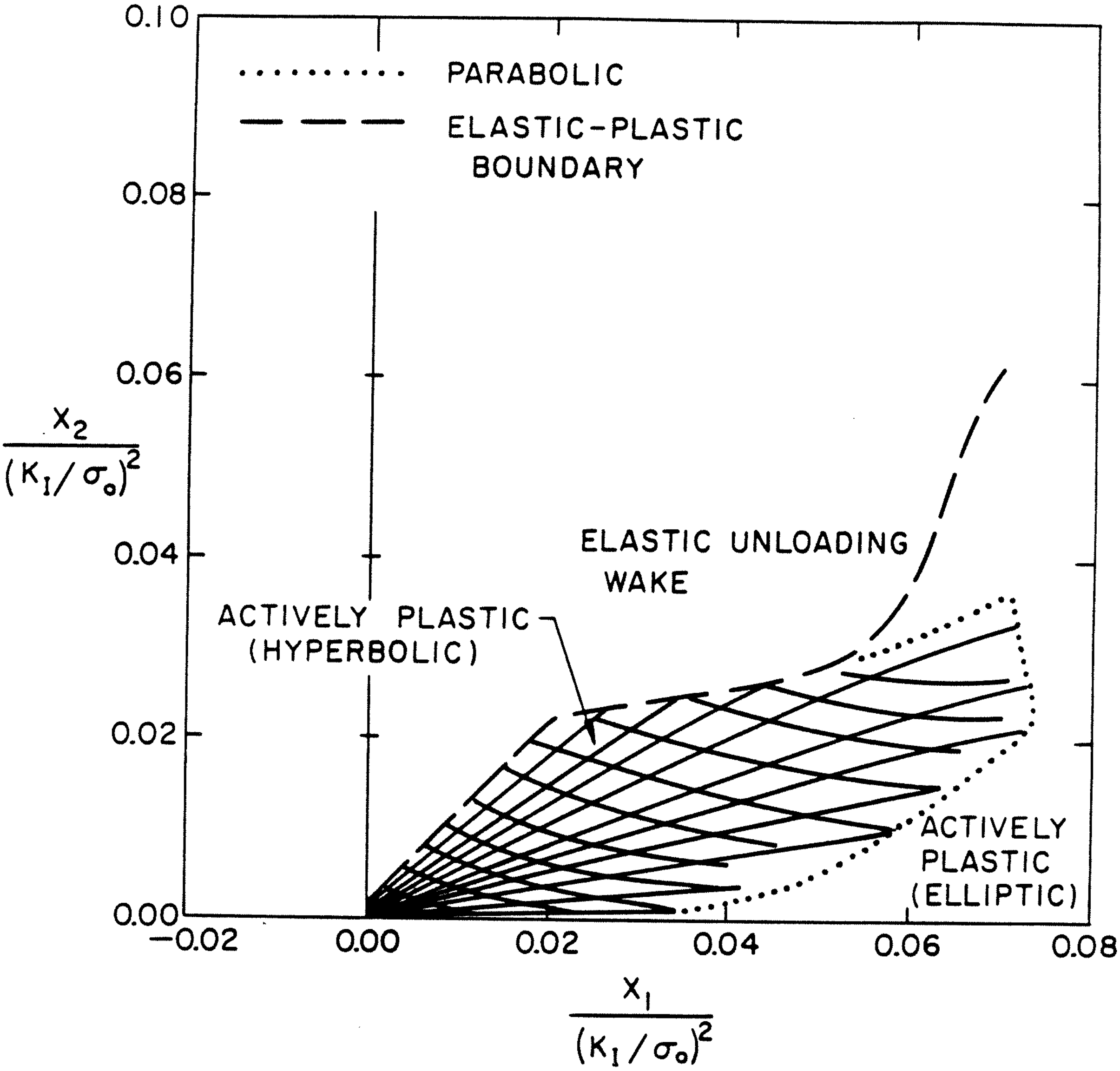

Figure 3.8. *Stress characteristics within active plastic zone.*

leading, according to the terminology of [3.15], to a "fuzzy crack tip phenomenon."

This was also observed in anti-plane shear by Dean and Hutchinson [3.11], who found that the active plastic zone obtained from their steady-state finite element solution extended from $\theta = 0°$ to about 60°, while the characteristics focussed at the tip only for angles less than 20°. For comparison, the analytical asymptotic solution of Chitaley and McClintock [3.19] in anti-plane shear crack growth has a centered fan region from $\theta = 0°$ to 19.69°, followed by a large elastic unloading region and a tiny secondary reloading zone.

Secondly, the radial family of characteristics in Fig. 3.8 bend downwards (towards the $\theta = 0$ ray) even for small distances ($r > 0.01(K_I/\sigma_0)^2$) from the tip. These two factors probably account for the strong discrepancy in the σ_{rr} stress component, between the finite element solution and the analytical asymptotic expression Eqn.(3.3.8), in the angular range $25° < \theta < 45°$.

Finally, the strong radial variation in the stresses ahead of the crack tip (Fig. 3.6), combined with the observation of the change in nature of the governing equations as the distance from the crack tip is increased (Fig. 3.8), seems to disagree with the assumption of a constant stress field ahead of the tip made in [3.31].

3.5 DUCTILE CRACK GROWTH CRITERION

Prediction of Asymptotic Crack Profile

In this section, a value for the parameter β in the asymptotic crack opening rate (3.3.4) will be obtained by fitting the analytical asymptotic form to the numerically obtained values. The method employed is similar to that used by Sham [3.10] in stable plane strain crack advance. Also, the linearity of the higher-order term in (3.3.4) with respect to $\dot{J}$ will be verified from the numerical solution.

To that effect, the crack opening rate $\dot{\delta}$ is written as

$$\dot{\delta} \sim \dot{a}\frac{\sigma_0}{E}\left[f\left(\frac{a}{L}\right) + \beta \ln\left(\frac{L}{r}\right)\right], \qquad r \to 0\,, \tag{3.5.1}$$

where L is the smallest element size and is a convenient length scale and a is the crack length. Under small-scale yielding conditions, the function $f(\frac{a}{L})$ can be shown to have the following form (see Sec.(3.3) and also [3.3,3.10]),

$$f\left(\frac{a}{L}\right) = g(T(a)) + \beta \ln\left(\frac{EJ(a)/\sigma_0^2}{L}\right), \tag{3.5.2}$$

where the quantity EJ/σ_0^2 has the dimension of length and is a measure of the plastic zone size. In the above equation, J, which is the remotely applied value of the J integral, and the nondimensional Paris tearing modulus $\mathrm{T} = \frac{\mathrm{E}}{\sigma_0^2}\frac{\mathrm{dJ}}{\mathrm{da}}$ are functions of the crack length a. If g(T) is a linear function of T as was assumed in Sec.(3.3), then comparison of Eqn.(3.5.2) with Eqns.(3.3.4) and (3.3.5) gives,

$$g(T) = \alpha T + \beta \ln s\,, \tag{3.5.3}$$

where α and s will be taken as constants for limited amounts of crack growth.

The crack displacement increment at a fixed material point $(x_1',0)$, when the crack grows from a_1 to a_2, can be obtained by integrating (3.5.1) as follows [3.10],

$$\frac{E}{\sigma_0}\frac{\Delta\delta(x_1',a)}{L} \sim \Delta F + \beta\left[\frac{a_2 - x_1'}{L}\ln\left(\frac{eL}{a_2 - x_1'}\right) - \frac{a_1 - x_1'}{L}\ln\left(\frac{eL}{a_1 - x_1'}\right)\right]. \tag{3.5.4}$$

In the above equation, e is the base of the natural logarithm and

$$\left.\begin{aligned} \Delta\delta(x_1',a) &= \delta(x_1',a_2) - \delta(x_1',a_1) \\ \Delta F &= \int_{a_1/L}^{a_2/L} f(\varsigma)d\varsigma \end{aligned}\right\}. \tag{3.5.5}$$

The values of β and ΔF were obtained as the slope and axis intercept of a least-squares straight line fit to $\frac{E}{\sigma_0}(\frac{\Delta\delta(x_1',a)}{L})$ versus $\Delta[\frac{a-x_1'}{L}\ln(\frac{eL}{a-x_1'})]$ for successive one-element crack growth steps.

The representative straight line fits for crack growths under four different values of T of 0, 5, 15 and 20, which were simulated for the twentieth release step, is shown in Fig. 3.9. The first node behind the crack tip has been omitted and the data corresponding to the next five nodes have been plotted in this graph. The first node was omitted because it was observed that the crack tip element undergoes excessive rotation during the nodal release procedure. This conclusion was reached by performing a sensitivity study as described below. The average value of β based on the first six nodal points behind the crack tip was obtained as 2.1. On omitting the first node, it was found that a better straight line fit can be made to the data corresponding to the next five nodal points (as in Fig. 3.9), which, however, gave a substantially lower average value of β of 1.7. The straight line fits underwent very little change on omitting the first and second nodes behind the tip, giving an average value of β of 1.67. On the basis of the above study, it is concluded that correct estimate for β, based on the crack displacement increments obtained from the finite element solution is around 1.70.

The excessive rotation of the crack tip element during the nodal release procedure was also observed in plane strain. For example, Rice and Sorensen [3.13] obtained estimates for β, from the finite element solution of Sorensen [3.14] for stable plane strain crack growth, as 9.5 and 4.8, based on the crack displacement increments of the first and second node behind the crack tip, respectively. The second estimate is in much closer agreement to the theoretical value of 5.46 [3.4]. The high estimate for β based on the data corresponding to the first node is probably a consequence of the nodal release procedure used to simulate crack extension.

The value of ΔF obtained from the axis intercept can be taken approximately as

$$\Delta F \approx \frac{(a_2 - a_1)}{L} f\left(\frac{\bar{a}}{L}\right) , \tag{3.5.6}$$

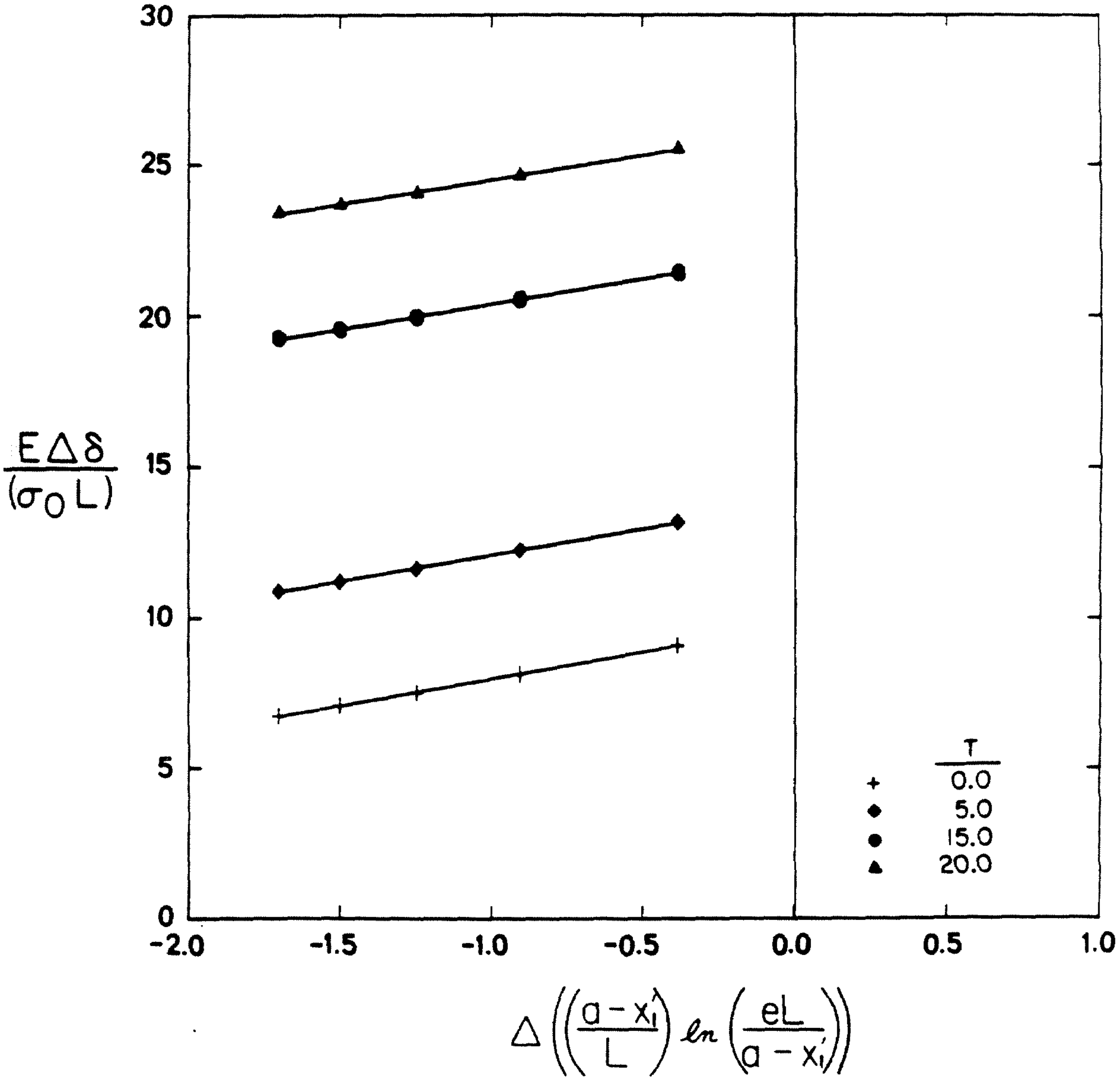

Figure 3.9. *Straight line fits to normalized crack displacement increments during the twentieth release step to determine β in asymptotic equation for crack opening rate.*

where

$$\bar{a} = \frac{(a_1 + a_2)}{2} .$$

The value of $f(\frac{\bar{a}}{L})$, which was computed from the above equation, was used along with the mean value of J during crack growth from a_1 to a_2 in Eqn.(3.5.2) to determine g(T). The values of g(T) obtained as above for crack growth simulations under four different values of T during the twentieth release step are plotted against T in Fig. 3.10. It can be seen that a very accurate straight-line fit can be made to the numerically obtained points validating the assumption of linearity of g(T) with respect to T made in Sec.(3.3).

On employing Eqn.(3.5.3) (with β as 1.7), we obtained the values of α and s as 0.82 and 0.60 from the slope and axis intercept of the straight line fit (Fig. 3.10), respectively. From the analysis which included the first node behind the crack tip to determine β and ΔF (giving β as 2.1), the values of α and s were estimated as 0.82 and 0.24, respectively.

The value of α computed above is thus completely insensitive to the determination of β and is also in good agreement with the corresponding estimate from the opening displacement of the stationary crack, which was 0.85 as reported in [3.9]. The value of s, on the other hand, seems to be extremely sensitive to the accuracy in determining β. This can also be observed in plane strain from the scatter in published numerical results for β and s [3.10-3.14].

Finally, the asymptotic crack profile as given by (3.3.7) is plotted in nondimensional form for crack growth at T=5.0 in Fig. 3.11 with the the parameters α, β and s taken as 0.82, 1.7 and 0.6, respectively. The values obtained from the finite element solution are also plotted in the figure for comparison. It is found that the predicted asymptotic crack profile is very close to the numerical solution in the range $r < 0.04(K_I/\sigma_0)^2$.

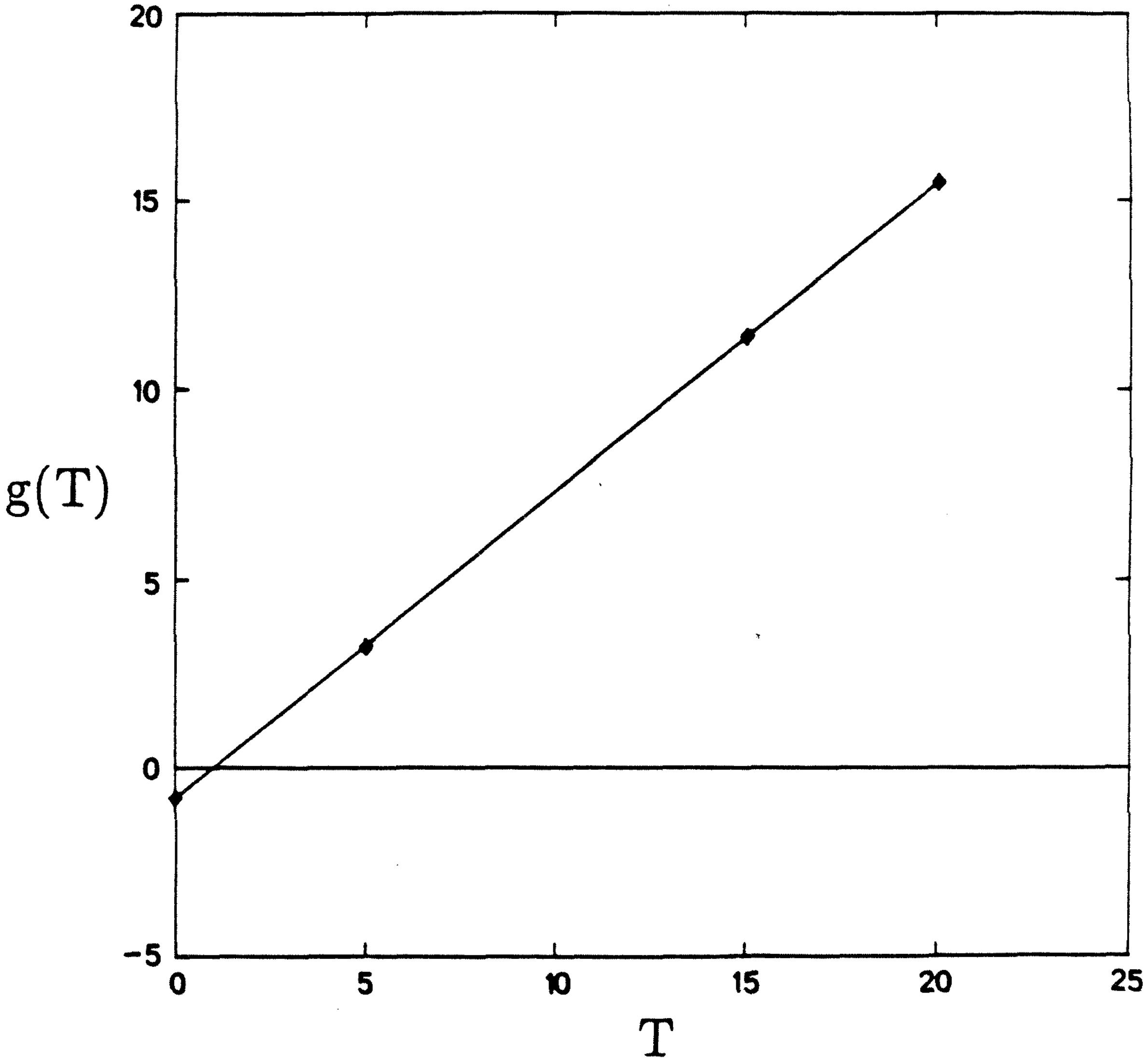

Figure 3.10. *Variation of higher-order term $g(T)$ in crack opening rate with respect to T. Straight line fit has been made to determine α and s.*

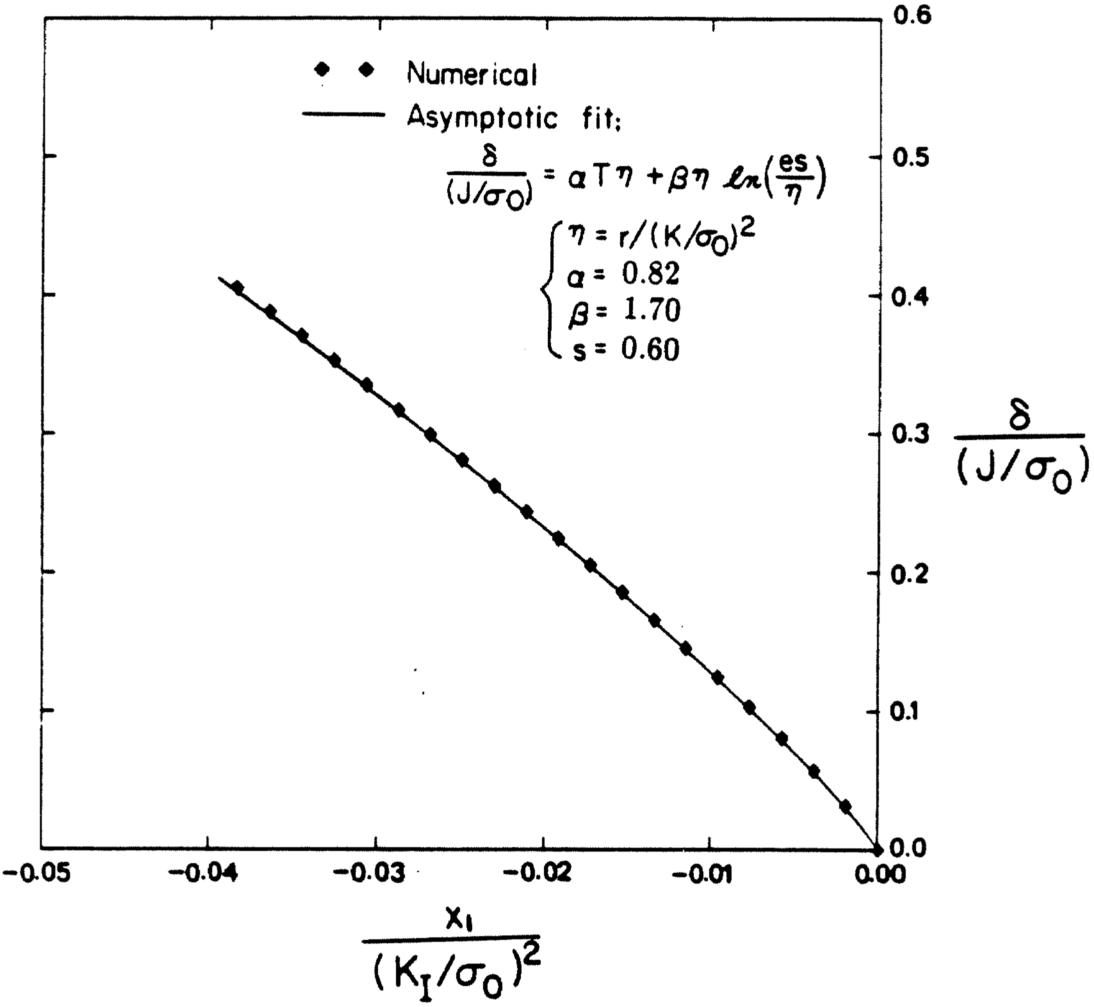

Figure 3.11. *Comparison of predicted asymptotic crack profile (solid line) with the finite element solution for stable crack growth at $T = 5.0$.*

Fracture Criterion

Motivated by the critical plastic strain criterion of McClintock and Irwin [3.17], Rice et al.[3.3] proposed that a geometrically similar near-tip crack opening profile should be maintained for continued crack growth. The near-tip crack displacement (3.3.7) during continuous crack extension can be written as

$$\delta = \beta\left(\frac{\sigma_0}{E}\right) r \ln\left(\frac{\rho}{r}\right), \qquad r \to 0 , \tag{3.5.7}$$

where

$$\rho = Re^{(1+T\alpha/\beta)} . \tag{3.5.8}$$

In the above equation, $R = sEJ/\sigma_0^2$ for small-scale yielding and T is the tearing modulus. The crack growth criterion stated above requires that the parameter ρ, which uniquely characterizes the near-tip crack profile, be constant for continued crack extension.

Thus, on estimating ρ from J_{IC} and T_0, which are the values of the far-field J and the tearing modulus T at the onset of crack growth, it is possible for us to obtain the following differential equation for J as a function of crack length a [3.3],

$$T = \frac{E}{\sigma_0^2}\frac{dJ(a)}{da} = T_0 - \frac{\beta}{\alpha}\ln\left(\frac{J}{J_{IC}}\right) . \tag{3.5.9}$$

By our using $J = J_{IC}$ and $a = a_0$ as initial conditions, the above equation can be integrated to give

$$\frac{a - a_0}{(EJ_{IC}/\sigma_0^2)} = \frac{\alpha}{\beta}e^{(\alpha T_0/\beta)}\left[E_i\left\{-\frac{\alpha T_0}{\beta}\right\} - E_i\left\{\ln\left(\frac{J}{J_{IC}}\right) - \frac{\alpha T_0}{\beta}\right\}\right] , \tag{3.5.10}$$

where $E_i\{.\}$ is the exponential integral function.

A family of plane stress resistance curves generated from (3.5.10) corresponding to several values of T_0 with α and β taken as 0.82 and 1.70, respectively, is shown in Fig. 3.12. The abscissa of the figure is the extent of crack growth, made

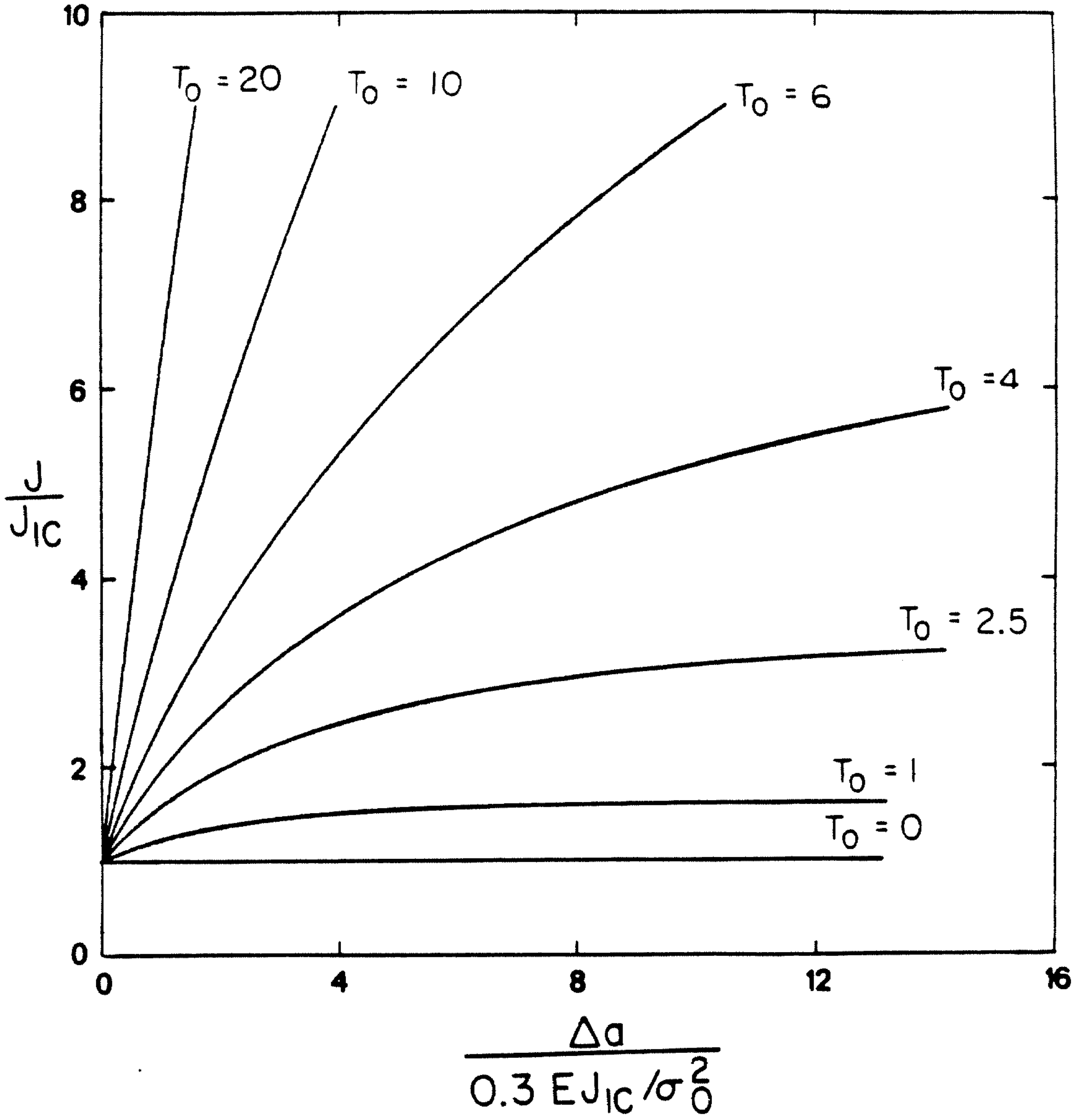

Figure 3.12. *Predicted normalized plane stress J resistance curves. The abscissa is the amount of crack growth normalized by a quantity which is approximately equal to the maximum plastic zone extent at initiation.*

dimensionless by the quantity $0.3\mathrm{E}\mathrm{J}_{\mathrm{IC}}/\sigma_0^2$ which is approximately equal to the maximum plastic zone extent at initiation. The flat portion of the curves corresponds to steady-state crack growth when no further increase in externally applied J is required to propagate the crack. Setting $\frac{\mathrm{dJ}}{\mathrm{da}} = 0$ in (3.5.9) gives J corresponding to steady-state as

$$J_{SS} = J_{IC} e^{\alpha T_0/\beta} \; . \tag{3.5.11}$$

Comparison of Fig. 3.12 with the corresponding plot for plane strain given in [3.3] shows that the amount of stable crack extension in plane stress is far more extensive than in plane strain. This is because the ratio α/β in plane stress, as computed in the present investigation, is 0.82/1.70, which is about 4.40 times larger than the corresponding ratio of 0.6/5.46 in plane strain [3.4,3.10]. Thus, for $\mathrm{T}_0 = 5$, the ratio $\mathrm{J}_{\mathrm{SS}}/\mathrm{J}_{\mathrm{IC}}$ calculated from (3.5.11) is 11.2 and 1.73 for plane stress and plane strain, respectively.

The above crack growth criterion can also be interpreted as the attainment of a critical opening angle, $\delta_{\mathrm{C}}/\mathrm{r}_{\mathrm{c}}$, at a small microstructural distance r_{c}, behind the crack tip. Following Rice et al.[3.3], it is then possible for us to examine the fracture criterion from the microstructural viewpoint. Thus, (3.5.7) and (3.5.9) imply that

$$T_0 = \frac{1}{\alpha}\left(\frac{\delta_C}{\epsilon_0 r_c}\right) - \frac{\beta}{\alpha}\ln\left(\frac{esEJ_{IC}}{r_c \sigma_0^2}\right) . \tag{3.5.12}$$

Substituting (3.5.12) into (3.5.11) gives

$$\frac{J_{SS}}{J_{IC}} = \frac{\epsilon_0 r_c}{sJ_{IC}/\sigma_0} e^{(\lambda_m/\beta - 1)} , \tag{3.5.13}$$

where λ_m is a microscale parameter given by,

$$\lambda_m = \frac{\delta_C}{\epsilon_0 r_c} . \tag{3.5.14}$$

If one makes the additional assumption, as in [3.11], that the value of the crack tip displacement at initiation δ_{IC} is equal to δ_C, then

$$\delta_{IC} = \delta_C = \alpha \frac{J_{IC}}{\sigma_0} \, . \tag{3.5.15}$$

Finally, substitution of (3.5.15) into (3.5.13) yields

$$\frac{J_{SS}}{J_{IC}} = \frac{\alpha}{s\lambda_m} e^{(\lambda_m/\beta - 1)} \, , \tag{3.5.16}$$

where λ_m is the microscale parameter defined in (3.5.14) .

The variation of J_{SS}/J_{IC} with respect to λ_m, as given by Eqn.(3.5.16), is plotted for both plane stress and plane strain in Fig. 3.13. The values of the parameters α and β were taken as mentioned earlier, and s was taken as 0.60 for plane stress from the present analysis and 0.12 for plane strain from [3.10]. The curve for plane stress compares well (for $\lambda_m < 10$) with the corresponding result obtained by Dean, using a different method from his steady-state numerical solution [3.16]. Also, the vast discrepancy noted earlier, in the potential for stable crack growth under plane stress as compared to plane strain, can be seen from this figure. This corroborates experimental observations of larger potential for stable crack growth under plane stress [3.25-3.27].

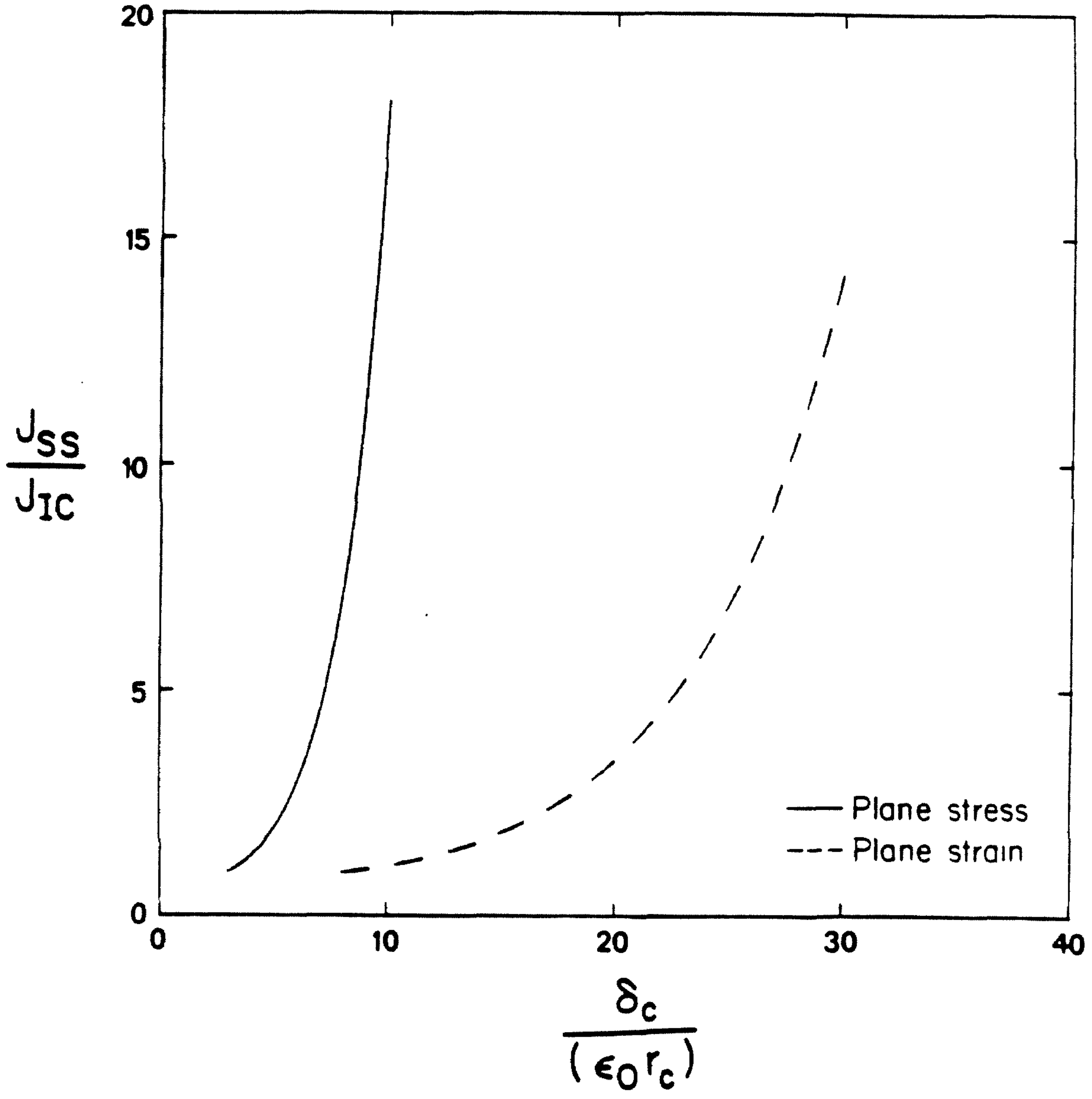

Figure 3.13. *Variation of J_{SS}/J_{IC} with respect to the microscale parameter λ_m for both plane stress and plane strain.*

CHAPTER REFERENCES

3.1. Rice, J. R. (1975), "Elastic-Plastic Models for Stable Crack Growth," *Mechanics and Mechanisms of Crack Growth*, M. J. May ed. , British Steel Corp. Physical Metallurgy Centre Publication, Sheffield, pp. 14-39.

3.2. Rice, J. R. (1982), "Elastic-Plastic Crack Growth," *Mechanics of Solids*, H. G. Hopkins and M. J. Sewell eds. , Pergamon Press, Oxford, pp. 539-562.

3.3. Rice, J. R. , Drugan, W. J. and Sham, T. L. (1980), "Elastic-Plastic Analysis of Growing Cracks," *Fracture Mechanics: Twelfth Conference*, ASTM STP 700, American Society for Testing and Materials, pp. 189-221.

3.4. Drugan, W. J. , Rice, J. R. and Sham, T. L. (1982), "Asymptotic Analysis of Growing Plane Strain Tensile Cracks in Elastic-Ideally Plastic Solids," *Journal of Mechanics and Physics of Solids*, Vol. 30, 447-473.

3.5. Drugan, W. J. and Rice, J. R. (1984), "Restrictions on Quasi-statically Moving Surfaces of Strong Discontinuity in Elastic-Plastic Solids," *Mechanics of Material Behaviour*, G. J. Dvorak and R. T. Shield eds. , Elsevier, Amsterdam, pp. 59-73.

3.6. Narasimhan, R. and Rosakis, A. J. (1986), "Reexamination of Jumps across Quasistatically Propagating Surfaces under Generalized Plane Stress in Anisotropically Hardening Elastic-Plastic Solids," Caltech Report SM 86-3, to appear in the *Journal of Applied Mechanics*.

3.7. Rice, J. R. (1968), "Mathematical Analysis in Mechanics of Fracture," *Fracture: An Advanced Treatise*, H. Liebowitz ed. , Academic Press, New York, Vol. 2, pp. 191-311.

3.8. Hutchinson, J. W. (1968), "Plastic Stress and Strain Fields at a Cracktip," *Journal of Mechanics and Physics of Solids*, Vol. 16, pp. 337-347.

3.9. Narasimhan, R. and Rosakis, A. J. (1986), "A Finite Element Analysis of Small-Scale Yielding near a Stationary Crack under Plane Stress," Caltech Report SM 86-21, Submitted for publication to *Journal of Mechanics and Physics of Solids.*

3.10. Sham, T. L. (1982), "A Finite Element Study of the Asymptotic Near-Tip Fields for Mode I Plane Strain Cracks in Elastic Ideally Plastic Solids," Ph. D. dissertation, Brown University, Providence.

3.11. Dean, R. H. and Hutchinson, J. W. (1980), "Quasi-Static Steady Crack Growth in Small-Scale Yielding," *Fracture Mechanics: Twelfth Conference*, ASTM STP 700, American Society for Testing and Materials, pp. 383-405.

3.12. Lam, P. S. and McMeeking, R. M. (1984), "Analysis of Steady Quasistatic Crack Growth in Plane Strain Tension in Elastic-Plastic Materials with Non-Isotropic Hardening," *Journal of Mechanics and Physics of Solids*, Vol. 32, 395-414.

3.13. Rice, J. R. and Sorensen, E. P. (1978), "Continuing Crack-Tip Deformation and Fracture for Plane Strain Crack Growth in Elastic-Plastic Solids," *Journal of Mechanics and Physics of Solids*, Vol. 26, 163-186.

3.14. Sorensen, E. P. (1979), "A Numerical Investigation of Plane Strain Stable Crack Growth under Small-Scale Yielding Conditions," *Elastic-Plastic Fracture*, ASTM STP 668, American Society for Testing and Materials, pp. 151-174.

3.15. Sorensen, E. P. (1978), "A Finite Element Investigation of Stable Crack Growth in Anti-Plane Shear," *International Journal of Fracture*, Vol. 14, 485-500.

3.16. Dean, R. H. (1983), "Elastic-Plastic Steady Crack Growth in Plane Stress," *Elastic-Plastic Fracture: Second Symposium, Volume I - Inelastic Crack Anal-*

ysis, ASTM STP 803, American Society for Testing and Materials, pp. I-39 - I-51.

3.17. McClintock, F. A. and Irwin, G. R. (1965), "Plasticity aspects of Fracture Mechanics," *Fracture Toughness Testing and its Applications*, ASTM STP 381, pp. 84-113.

3.18. Castañeda, P. P. (1985), "Asymptotic Fields in Steady Crack Growth with Linear Strain-Hardening," Harvard University Report MECH-69.

3.19. Chitaley, A. D. and McClintock, F. A. (1971), "Elastic-Plastic Mechanics of Steady Crack Growth under Anti-Plane Shear," *Journal of Mechanics and Physics of Solids*, Vol. 19, 147-163.

3.20. Amazigo, J. C. and Hutchinson, J. W. (1977), "Crack-Tip Fields in Steady Crack Growth with Linear Strain-Hardening," *Journal of Mechanics and Physics of Solids*, Vol. 25, 81-97.

3.21. Bathe, K. J. (1982), *Finite Element Procedures in Engineering Analysis*, Prentice Hall, Englewood Cliffs, New Jersey.

3.22. Kachanov, L. M. (1974), *Fundamentals of the Theory of Plasticity*, Mir Publishers, Moscow, pp. 244-262.

3.23. Slepyan, L. I. (1974), "Growing Cracks during Plane deformation of an Elastic-Plastic body," *Izv. Akad. Nauk. SSSR, Mekhanika Tverdogo Tela*, Vol. 9, 57-67.

3.24. Gao, Y. C. (1980), "Elastic-Plastic Fields at the tip of a Crack growing steadily in a Perfectly Plastic Medium," *Acta Mechanica Sinicia* (in Chinese), No. 1, 48-56.

3.25. Broek, D. (1968), "Some Considerations on Slow Crack Growth," *International Journal of Fracture*, Vol. 4, 19-34.

3.26. Green, G. and Knott, J. F. (1975), "On Effects of Thickness on Ductile Crack Growth in Mild Steel," *Journal of Mechanics and Physics of Solids*, Vol. 23, 167-183.

3.27. Yoder, G. R. and Griffis, C. A. (1976), *Mechanics of Crack Growth*, ASTM STP 590, American Society for Testing and Materials, pp. 61-81.

3.28. Hermann, L. and Rice, J. R. (1980), "Comparison of experiment and theory for Elastic-plastic Plane Strain Crack Growth," *Metal Science*, Vol. 14, 285-291.

3.29. Rosakis, A. J. and Freund, L. B. (1982), "Optical Measurement of the Plastic Strain Concentration at a Cracktip in a Ductile Steel plate," *Journal of Engineering Materials and Technology*, Transactions of ASME, Vol. 104, 115-120.

3.30. Zehnder, A. T. , Rosakis, A. J. and Narasimhan, R. (1986), "Measurement of J integral with Caustics: An experimental and Numerical Investigation," Caltech Report SM 86-8.

3.31. Achenbach, J. D. and Dunayevsky, V. (1984), "Crack Growth under Plane Stress Conditions in an Elastic Perfectly-Plastic Material," *Journal of Mechanics and Physics of Solids*, Vol. 32, 89-100.

CHAPTER IV

INFLUENCE OF ISOTROPIC HARDENING ON QUASI-STATIC PLANE STRESS CRACK GROWTH

4.1 INTRODUCTION

A slow, stable crack extension phase is often observed in elastic-plastic materials [4.18-4.20] prior to catastrophic failure, during which a steady increase in applied load is required to propagate the crack. Unlike the case of elastic materials, a complete refocussing of the strains at the tip of an extended crack is prevented in elastic-plastic materials due to the irreversible nature of plastic deformation. The lessened strain concentration at the tip that results during crack extension is the primary reason for stable crack growth in elastic-plastic solids. Thus, as emphasized by Rice [4.3], the reversible elastic strain increments are destabilizing, since their incompatibility induces additional plastic strain increments at the tip of the advancing crack.

The main progress in understanding the stress and deformation fields at the tip of a growing crack has been limited to elastic-perfectly plastic materials. Also, attention has been focussed primarily on the study of anti-plane shear and plane strain crack growth. Chitaley and McClintock [4.21] found an asymptotic solution for a crack growing quasi-statically in an elastic-perfectly plastic material under anti-plane shear conditions. Rice et al.[4.5], Gao [4.7] and Slepyan [4.8] independently assembled an asymptotic solution for crack growth in an incompressible elastic-perfectly plastic material under Mode I plane strain. Drugan et al.[4.4] extended the analysis of [4.5] to account for elastic compressibility.

However, the singularity fields at growing crack tips in hardening solids are not completely understood. Amazigo and Hutchinson [4.9] presented an asymptotic analysis for steady-state crack extension in a linear hardening solid under anti-plane shear and Mode I plane strain and plane stress. Castañeda [4.10] has recently extended the analysis of [4.9] to include the possibility of secondary (plastic) reloading and has also treated Mode II plane strain and plane stress crack growth. Nevertheless, the use of a linear hardening rule and some complications regarding the perfectly plastic limit have curtailed the applicability of the results of [4.9] and [4.10].

Gao and Hwang [4.11] performed a preliminary investigation about the near-tip fields for a crack growing in a material governed by a more realistic power hardening law. The main feature of their solution was an interaction between the elastic and plastic strain rates, which was emphasized by Rice [4.3] for the perfectly plastic case. They considered an incompressible elastic-plastic material under Mode I plane strain and proposed the following form for the dominant near-tip solution,

$$\left.\begin{aligned} \sigma_{ij} &\sim \sigma^{\circ}_{ij}(\theta)\left(\ln\left(\frac{\bar{R}}{r}\right)\right)^{\frac{1}{(n-1)}} \\ \epsilon^{p}_{ij} &\sim \epsilon^{\circ p}_{ij}(\theta)\left(\ln\left(\frac{\bar{R}}{r}\right)\right)^{\frac{n}{(n-1)}} \end{aligned}\right\}, \qquad r \to 0\,, \tag{4.1.1}$$

where R̄ is an undetermined length dimension and n is the hardening exponent. For the specific problem which they considered, Gao and Hwang showed that $\sigma^{\circ}_{ij}(\theta)$ is essentially the same as the asymptotic stress field for the perfectly plastic case. Thus, far large n, their dominant solution for the stresses, uniformly approaches the perfectly plastic field of [4.5,4.7,4.8]. Nevertheless, some issues still remain to be resolved, before the near-tip behaviour in power hardening solids during quasi-static crack growth can be well understood.

Finite element studies using a nodal release procedure were conducted to simulate crack extension under anti-plane shear by Sorensen [4.12] and Mode I plane strain by Rice and Sorensen [4.13] and Sham [4.14]. Dean and Hutchinson [4.15] and Lam and McMeeking [4.16] employed a Eulerian finite element formulation to investigate steady-state crack advance in the above cases. Besides isotropic hardening, the influence of corner formation on the yield surface and the Bauschinger effect were studied in [4.15] and [4.16].

As far as crack growth under Mode I plane stress is concerned, comparatively much less progress has been made. A preliminary investigation has been performed by Rice [4.4], concerning the nature of the asymptotic stress and deformation fields near a crack growing in an elastic-perfectly plastic material under plane stress. However, a complete asymptotic solution for this problem has not yet been found. This has greatly impeded a conceptual understanding of the mechanics of quasi-static crack growth in thin plates.

A steady-state Eulerian finite element study has been conducted recently by Dean [4.17] for plane stress crack growth in a linear hardening material (including the perfectly plastic case), following the approach of [4.15]. But the analysis of [4.17] is not very detailed, and certain issues pertaining to the near-tip stress and deformation fields have not been examined. In order to resolve these issues, we performed a detailed finite element analysis to simulate stable crack extension under plane stress in an elastic-perfectly plastic material [4.2] (see Chapter III). Besides revealing certain interesting features about the near-tip fields, the analysis of [4.2] predicted that the extent of stable crack growth under plane stress, based on a ductile crack growth criterion [4.5,4.13], could be far more extensive than plane strain. This corroborates experimental observations (see for example [4.18]), of a greater potential for stable crack growth under plane stress as compared with plane strain.

In this work, a detailed finite element analysis similar to [4.2] is undertaken to model crack growth under plane stress in isotropic power hardening solids. This is a continuation of an earlier work [4.1] (see Chapter II), which analyzed the monotonic loading of a stationary crack. Two crack growth histories (see Sec.(4.2)) are simulated in the present investigation to study the mechanics problem of quasi-static crack extension and also the initial phase of stable crack growth under small-scale yielding, as would be observed in an experiment (as in [4.20]). The influence of hardening on the active plastic zone and near-tip stress and deformation fields is investigated, and comparisons are made with the results obtained in [4.2] for the perfectly plastic case.

A ductile crack growth criterion, based on the attainment of a critical crack opening displacement at a small microstructural distance behind the tip (which was used in [4.2]), is employed to study the effect of isotropic hardening on the potential for stable crack growth under plane stress. As in anti-plane shear and Mode I plane strain [4.15,4.16], it is found that predictions based on a perfectly plastic model could be unconservative, when the material actually possesses some hardening. In view of this observation, it is suggested that the influence of corner formation on the yield surface and kinematic hardening should also be examined for plane stress.

4.2 NUMERICAL ANALYSIS

Formulation

The numerical modelling of the Mode I plane stress, small-scale yielding problem was discussed in detail in [4.1] (see Chapter II), where the analysis of a monotonically loaded stationary crack was performed. In the present investigation, the results obtained in [4.1] will be used as initial conditions to simulate quasi-static crack extension. Some of the features about the numerical analysis that were described in [4.1] will be summarized in this section.

The upper half of a domain R containing a crack and represented entirely by finite elements is shown in Figs. 4.1*a* and *b*. The leading term in the displacements

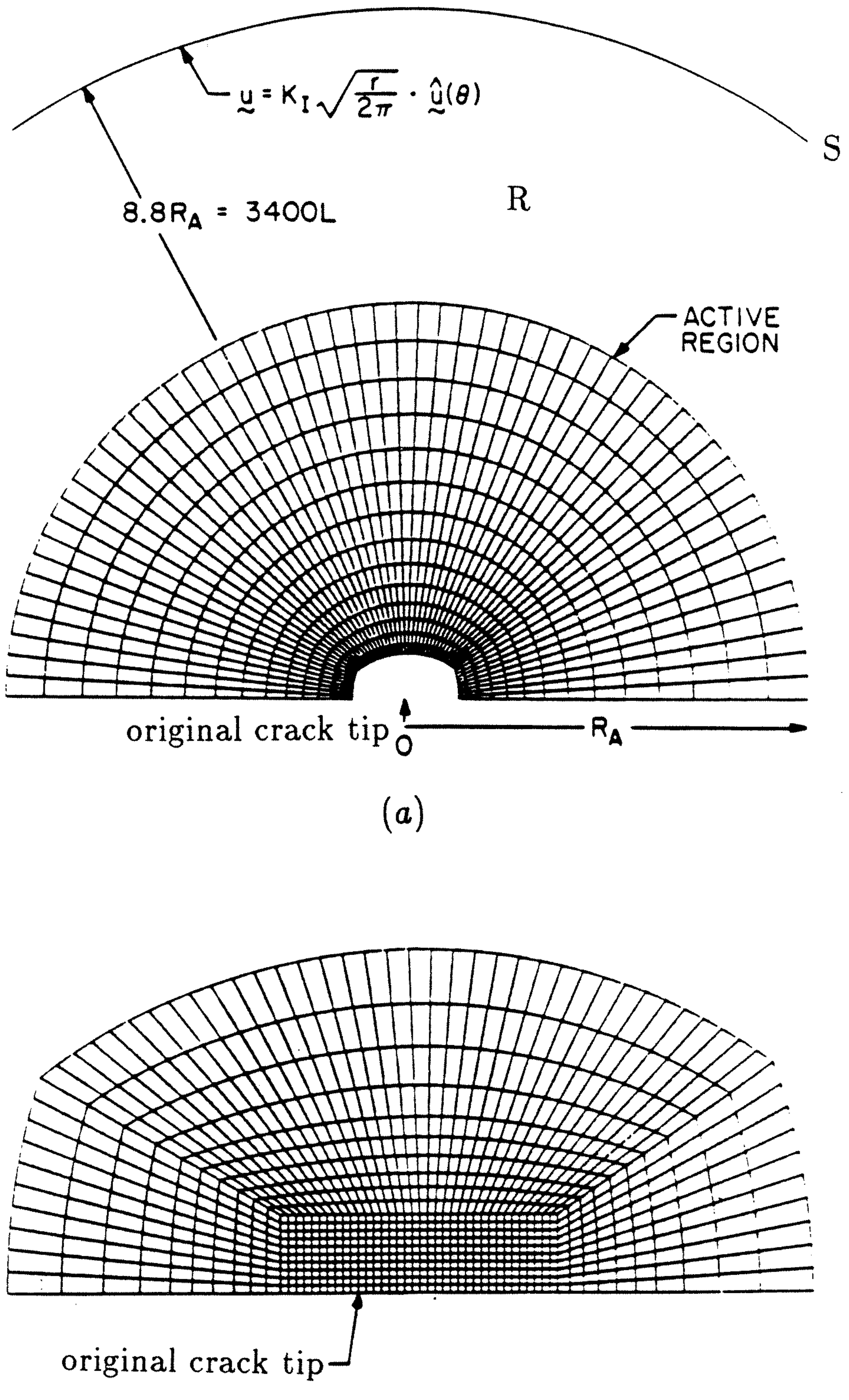

Figure 4.1. *Finite element mesh: a) Outer mesh b) Fine mesh near the crack tip.*

of the linear elastic asymptotic solution was specified as a boundary condition on the outermost contour S of the domain (see Fig. 4.1*a*). The loading was applied through the Mode I stress intensity factor K_I or equivalently through the far-field value of the J integral. All plastic deformation was contained within a distance from the crack tip which was less than $\frac{1}{30}$ of the radius of S.

The active region in Fig. 4.1*a* has a total of 1704 four noded quadrilateral elements and 3549 degrees of freedom. The quadrilaterals were formed from four constant strain triangles with static condensation of the internal node. Static condensation was also employed in the large region surrounding the active mesh, which always remained elastic. The cutout in Fig. 4.1*a*, which is the fine mesh region near the crack tip, is shown in detail in Fig. 4.1*b*. The small square elements near the crack tip have a size L, which is about $\frac{1}{385}$ of the radius R_A of the active region and about $\frac{1}{3400}$ of the radius of S.

Constitutive Assumptions

The material model that was considered here was that of an elastic-plastic solid with an isotropic power law hardening behaviour. A small strain incremental plasticity theory was employed along with the Huber-Von Mises yield condition and the the associated flow rule. The Huber-Von Mises yield condition for isotropic hardening takes the form,

$$\mathrm{f}(\underline{\sigma}, \bar{\epsilon}^{\mathrm{p}}) = \mathrm{F}(\underline{\sigma}) - \bar{\sigma}^2(\bar{\epsilon}^{\mathrm{p}}) \tag{4.2.1}$$

where $\mathrm{F}(\underline{\sigma}) = \frac{3}{2}\underline{\mathrm{S}} \cdot \underline{\mathrm{S}}$, and $\bar{\epsilon}^p = \int \left(\frac{2}{3}\epsilon^p_{ij}\epsilon^p_{ij}\right)^{1/2} dt$ is the accumulated equivalent plastic strain. In the above, $\underline{\mathrm{S}}$ is the deviatoric stress tensor, and $\bar{\sigma}(\bar{\epsilon}^p)$ is defined by the following power hardening rule,

$$\frac{\bar{\epsilon}^p}{\epsilon_0} = \left(\frac{\bar{\sigma}}{\sigma_0}\right)^n - \frac{\bar{\sigma}}{\sigma_0}\,. \tag{4.2.2}$$

Here σ_0 and ϵ_0 are the yield stress and strain in uniaxial tension.

The total strain rate tensor is assumed to be decomposed into elastic and plastic parts, and the constitutive law for material currently experiencing plastic deformation is given by [4.1],

$$\dot{\sigma}_{ij} = C^*_{ijkl}\dot{\epsilon}_{kl} = \left[C_{ijkl} - \frac{C_{ijpq}S_{pq}S_{mn}C_{mnkl}}{S_{rt}C_{rtuv}S_{uv} + \frac{4}{9}\bar{\sigma}^2 H} \right] \dot{\epsilon}_{kl} \ . \tag{4.2.3}$$

Here C_{ijkl} is the isotropic, positive definite elasticity tensor and $H = \frac{d\bar{\sigma}}{d\bar{\epsilon}^p}$, which can be obtained from (4.2.2). In the present analysis, the yield criterion and the constitutive law were used along with the plane stress condition,

$$\sigma_{3i} \equiv 0 \ . \tag{4.2.4}$$

On using Eqn.(4.2.4) in (4.2.3), a constraint for $\dot{\epsilon}_{33}$ in terms of $\dot{\epsilon}_{\alpha\beta}$ may be obtained.

The computations were performed for two levels of hardening, n = 5 and 9. The ratio of the Young's modulus to the yield stress in pure shear (E/τ_0) was taken as 1400 and the Poissons ratio as 0.3 in the calculations.

Finite Element Scheme

A displacement-based finite element method was employed and inertia effects were neglected in the analysis. The incremental finite element equilibrium equations were derived from the principle of virtual work by linearization [4.1]. These equations were solved for each time step using an iterative Newton-Raphson approach, which is summarized in Appendix A. An explicit integration procedure also known as the Tangential Predictor-Radial return method was employed together with subincrementation to integrate the incremental stress strain law (see Appendix A for details).

Solution Strategy

In this study, two simple crack growth histories were simulated employing the nodal release procedure [4.2,4.14]. In the first case, the maximum plastic zone extent at the end of the stationary loading process [4.1] was slightly more than 50 times the smallest element size L. Subsequently, twenty one-element crack growth steps were simulated using the nodal release procedure [4.2], holding the externally applied load fixed. This is shown in the Fig. 4.2 for both cases of hardening, $n = 5$ and 9 as the lines designated by a zero value for the nondimensional Paris tearing modulus, $T \equiv \frac{E}{\sigma_0^2} \frac{dJ}{da}$. In this figure, the value of J has been made dimensionless by the amount J_i, which caused incipient yielding in the element nearest to the tip during the monotonic loading of the stationary crack [4.1]. Also, the extent of crack growth Δa has been made dimensionless by the smallest element length L.

The purpose of this investigation is to examine the nature of the near-tip stress and deformation fields for the mechanics problem of quasi-static crack growth without the influence of increase in applied load. Following Rice [4.3], this would correspond to a hypothetical situation in which a cracked specimen is initially loaded by clamping portions of its boundary and imposing displacements, which is then followed by crack extension by saw-cutting ahead under fixed boundary displacements.

However, in an actual situation, after initiation, a crack will generally grow stably in an elastic-plastic material for an extent typically of the order of a few plastic zone sizes, during which the applied load will have to be increased to propagate the crack. A steady-state condition will then be reached, after which no further increase in applied load will be required for additional crack growth. In the second load history, stable crack extension was modelled (in a continuous manner) by simultaneously increasing the applied load during the nodal release procedure as in [4.2]. This was accomplished by simulating fifteen one-element crack growth steps under $T = 1.5$, as shown in Fig. 4.2, following the stationary loading process [4.1]. The maximum extent of the plastic zone was over 100 times the smallest element

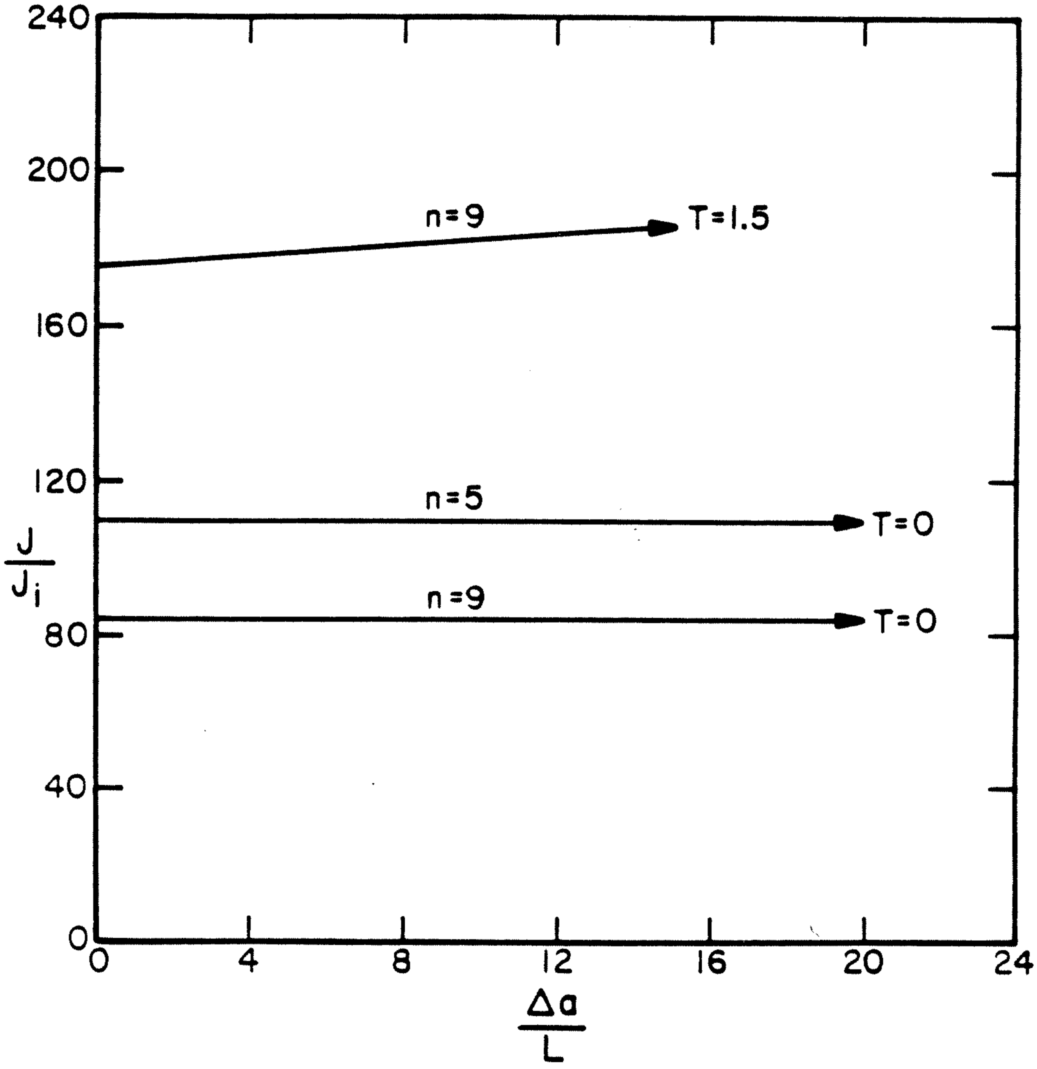

Figure 4.2. *J versus crack growth history.*

length, L. Only the material with n = 9 was considered in this investigation.

The analysis of [4.2] predicts a ratio J_{SS}/J_{IC}, of the value of J at steady-state to that at initiation, of around 2 for a perfectly plastic material, when the value of the tearing modulus at initiation, T_0, is 1.5. Hence a constant value of T of 1.5 was chosen, so that this history could be viewed as the initial phase of stable crack extension under contained yielding conditions, as would be observed in an experiment (as in [4.20]).

In the following section, detailed results will be presented initally for n = 5 and 9 corresponding to the first load history. At the end of the section, comparison between the results for the two load histories will be made for the material with n = 9.

4.3 RESULTS AND DISCUSSION

Active Plastic Zones

The active plastic zone surrounding the propagating crack tip after the twentieth crack growth step is shown in Fig. 4.3 for n = 5 and 9, in moving coordinates that have been made dimensionless by the self-similar parameter $(K_I/\sigma_0)^2$. The plastic zone obtained in [4.2] for stable plane stress crack growth in an elastic-perfectly plastic material is also shown for comparison.[1] The current crack tip is at the orign of the coordinate system, and a point in the figure represents an actively yielding integration station within an element.

A large elastic unloading region can be seen following the active plastic zone. No secondary (plastic) reloading along the crack flank has been observed for any level of hardening from the present numerical solution. The asymptotic angular extent of

---

[1] Throughout this chapter, results given as $n = \infty$ will correspond to the perfectly plastic crack growth analysis of [4.2] (see Chapter III).

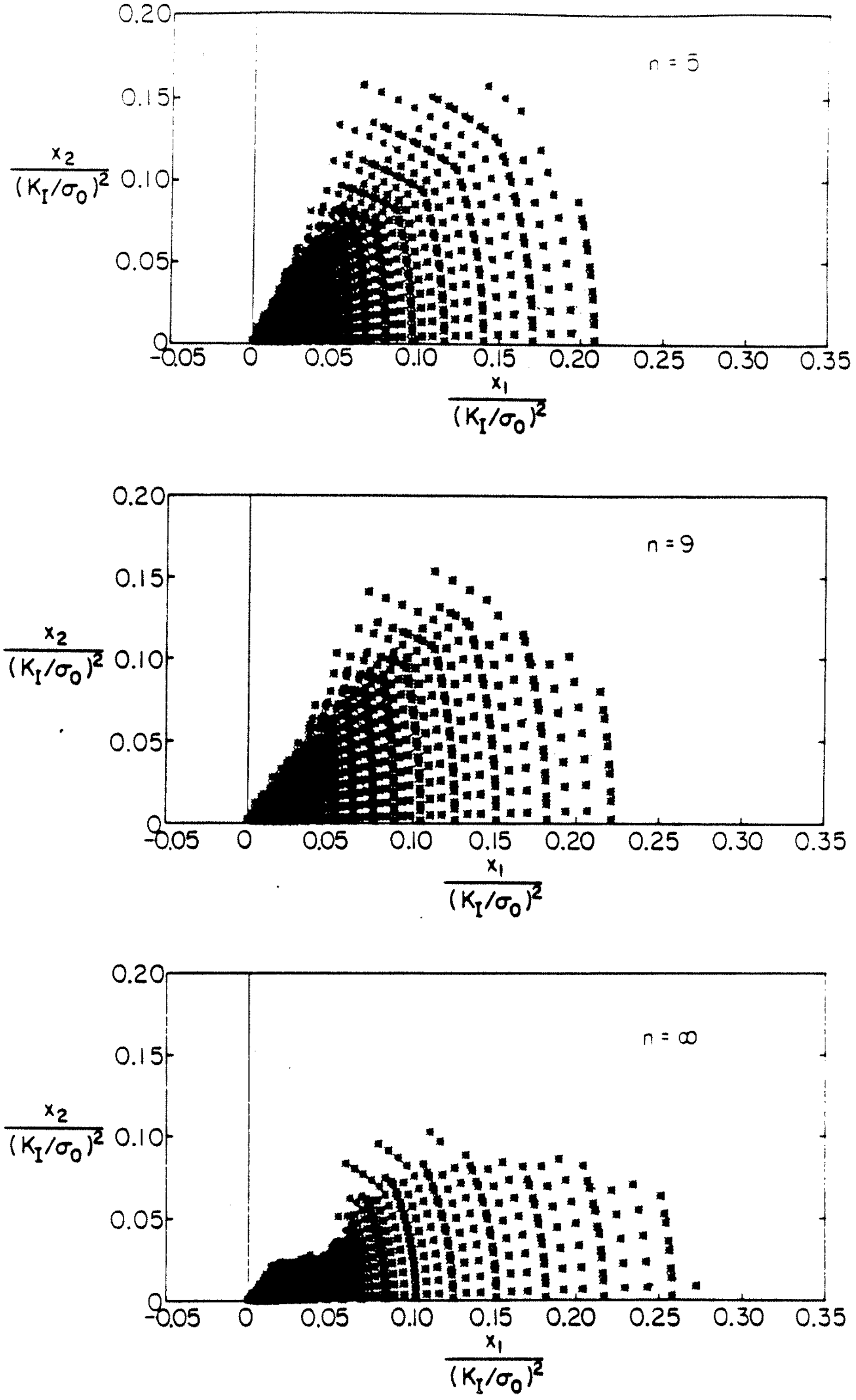

Figure 4.3. *Active plastic zone surrounding the propagating crack tip for various levels of hardening.*

the active plastic zone, θ_p, decreases with decreasing hardening (increasing n). The values of θ_p are approximately 65°, 55° and 45° for $n = 5, 9$ and ∞, respectively. The maximum radial extent of the active plastic zone, R_p, which occurs directly ahead of the crack tip, increases with decreasing hardening. The values of R_p are about $0.22(K_I/\sigma_0)^2$, $0.24(K_I/\sigma_0)^2$ and $0.28(K_I/\sigma_0)^2$ for $n = 5, 9$ and ∞, respectively.

Comparison of Fig. 4.3 with the plastic zone surrounding the stationary crack [4.1] shows that the active plastic zone becomes more acute (sharper) with the onset of crack growth. The results for the stationary problem in [4.1] show rounded plastic zones for the hardening cases, with yielding spreading beyond 90° near the crack tip. Strong changes in the near-tip plastic zone shape occurred during the first few crack growth steps, and then the overall features were unaltered with subsequent crack advance. The maximum radial extent of the plastic zone, R_p, given above for the propagating crack, is about the same as in the stationary problem [4.1] for all levels of hardening.

A kink in the trailing boundary of the active plastic zone (Fig. 4.3) appears to develop for materials with low hardening, and it becomes pronounced for the perfectly plastic case. The reason for this development could be related to the change in nature of the governing equations (from elliptic to hyperbolic), in the limit as the perfectly plastic case is approached. Such a behaviour can also be observed from the plastic zone shapes given by Dean and Hutchinson [4.15] for crack growth under anti-plane shear in a linear hardening material. The similarity between the present plane stress plastic zone shapes and the anti-plane shear results of [4.15] stems from the presence of an intense deformation zone ahead of the crack tip in both cases.

The active plastic zones of Fig. 4.3 and the corresponding results obtained by Dean [4.17] for steady-state crack growth under plane stress in a linear hardening material have essentially the same features. However, one difference seems to be the absence of the kink in the active plastic zone for the perfectly plastic limit in Dean's solution. Nevertheless, the present solution is more detailed than that of [4.17], because it has a larger ratio of plastic zone to smallest element size as compared with that in [4.17]. Also, unlike [4.17], the initial phase of crack growth was modelled in the present analysis.

Radial Distribution of Plastic Strains

The radial distribution of the normalized plastic strain, $\epsilon^p_{22}/\epsilon_0$, with respect to normalized distance, $r/(K_I/\sigma_0)^2$, ahead of the propagating crack tip is shown in Fig. 4.4 for a material with $n = 9$. Results are presented for various levels of crack growth at a fixed applied load, along with the plastic strain distribution ahead of a monotonically loaded stationary crack tip, which was obtained in [4.1]. As can be seen from this figure, the plastic strain ahead of the moving crack tip converges rapidly during the first few crack growth steps to an invariant distribution. For example, at a distance of $r = 0.013(K_I/\sigma_0)^2$ ahead of the moving tip, the plastic strain dropped by 30% during the first five crack growth steps and by 8%, 3% and 1.5% during the sixth to tenth steps, eleventh to fifteenth steps and sixteenth to twentieth steps, respectively.

Such rapid convergence was typical of the other hardening case ($n = 5$), as well as the perfectly plastic material [4.2]. The weaker singularity in the plastic strains near the tip during crack growth, as compared with the stationary problem in Fig. 4.4, is due to the fact that the crack propagates into material that has already deformed plastically [4.3]. The radial distribution of the plastic strains ahead of the tip at the end of the twentieth release step is shown in Fig. 4.5 for the two levels of hardening, $n = 5$ and 9.

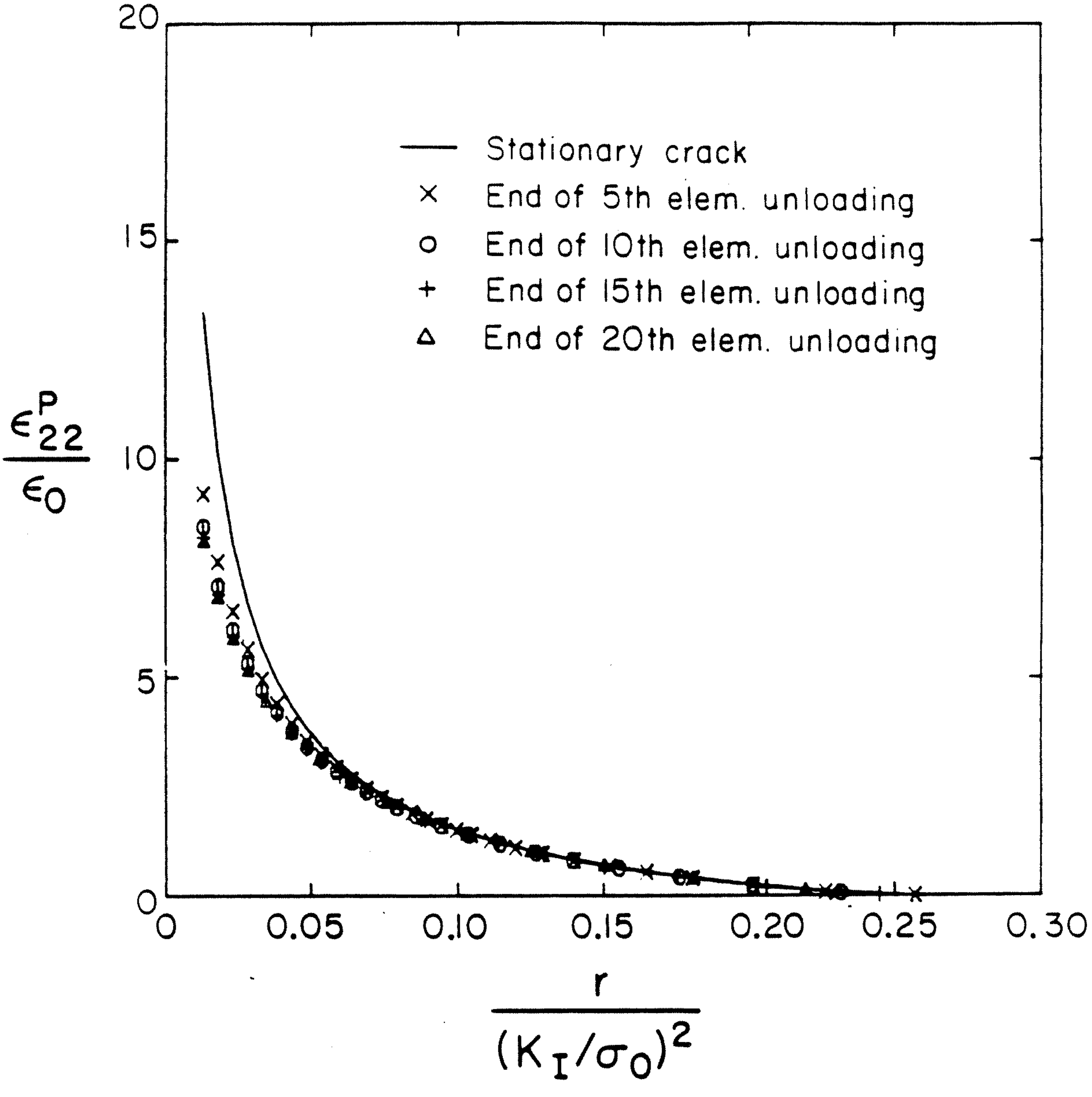

Figure 4.4. *Radial distribution of plastic strain ahead of the propagating crack tip for various levels of crack growth under fixed applied load for a material with* $n=9$.

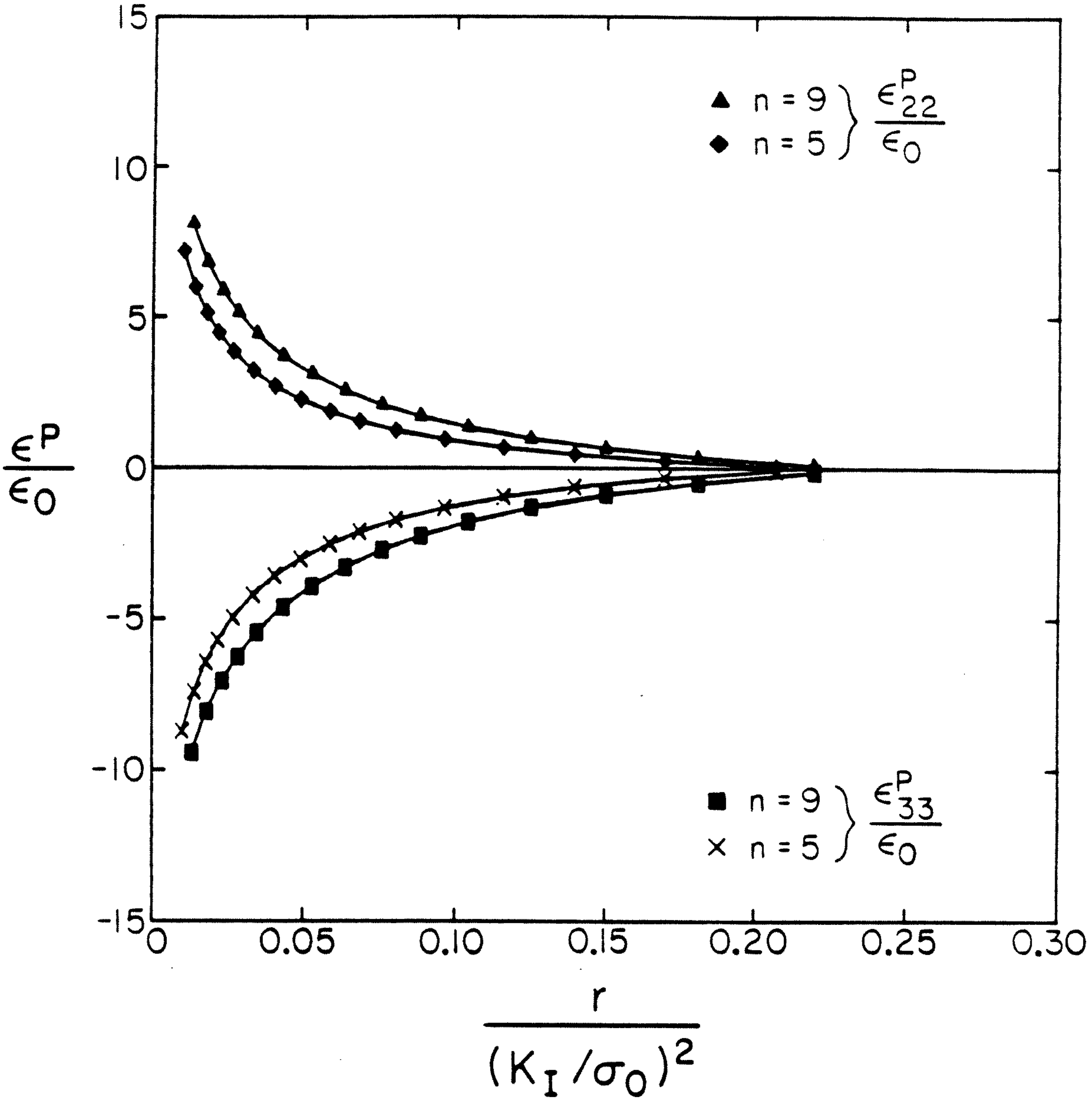

Figure 4.5. *Radial distribution of plastic strains ahead of the propagating crack tip at the end of the twentieth crack growth step at fixed applied load for n=5 and 9.*

Radial Distribution of Stresses

The radial distribution of the normalized opening stress, σ_{22}/τ_0, ahead of the moving crack tip is shown in Fig. 4.6 for $n = 5$ and 9, along with the perfect plasticity solution of [4.2]. As can be seen from this figure, the stress components become more strongly singular with increasing hardening. The perfect plasticity solution of [4.2] for σ_{22} tends to a bounded value of $1.999\tau_0$, as the crack tip is approached along the $\theta = 0$ ray, and is in excellent agreement with the preliminary asymptotic result of Rice [4.4]. This asymptotic limit was the same as that obtained by the numerical solution near the stationary crack tip [4.1].

The stress variation for the hardening materials in Fig. 4.6 also differs only slightly from the stationary crack distribution of [4.1], for moderate to large distances from the tip. For example, at a distance of $r = 0.018(K_I/\sigma_0)^2$ ahead of the tip, the ratio of the opening stress for the propagating crack to that for the stationary problem is 3.04/3.13 and 2.58/2.66 for $n = 5$ and 9, respectively. Also, as pointed out in [4.1], the stress distribution (Fig. 4.6) appears to be relatively insensitive to the hardening level for distances from the tip exceeding about $0.15(K_I/\sigma_0)^2$.

In order to study the influence of the crack tip plastic zone on the stress field in the surrounding elastic region, the radial stress distribution ahead of the moving crack tip is shown on an expanded scale for $n = 5$ and 9 in Fig. 4.7. The singular elastic solution (K_I field) is also indicated by the solid line in the figure, for comparison. The distribution of stresses outside the plastic zone is almost identical to the corresponding result obtained for the stationary problem in [4.1]. The σ_{22} stress component obtained from the numerical solution differs strongly (by more than 30%) from that given by the K_I field at the elastic-plastic boundary ($r = R_p$). But a rapid transition in the stress distribution takes place immediately outside the plastic zone and, as in [4.1], the stresses agree closely with those of the K_I field for

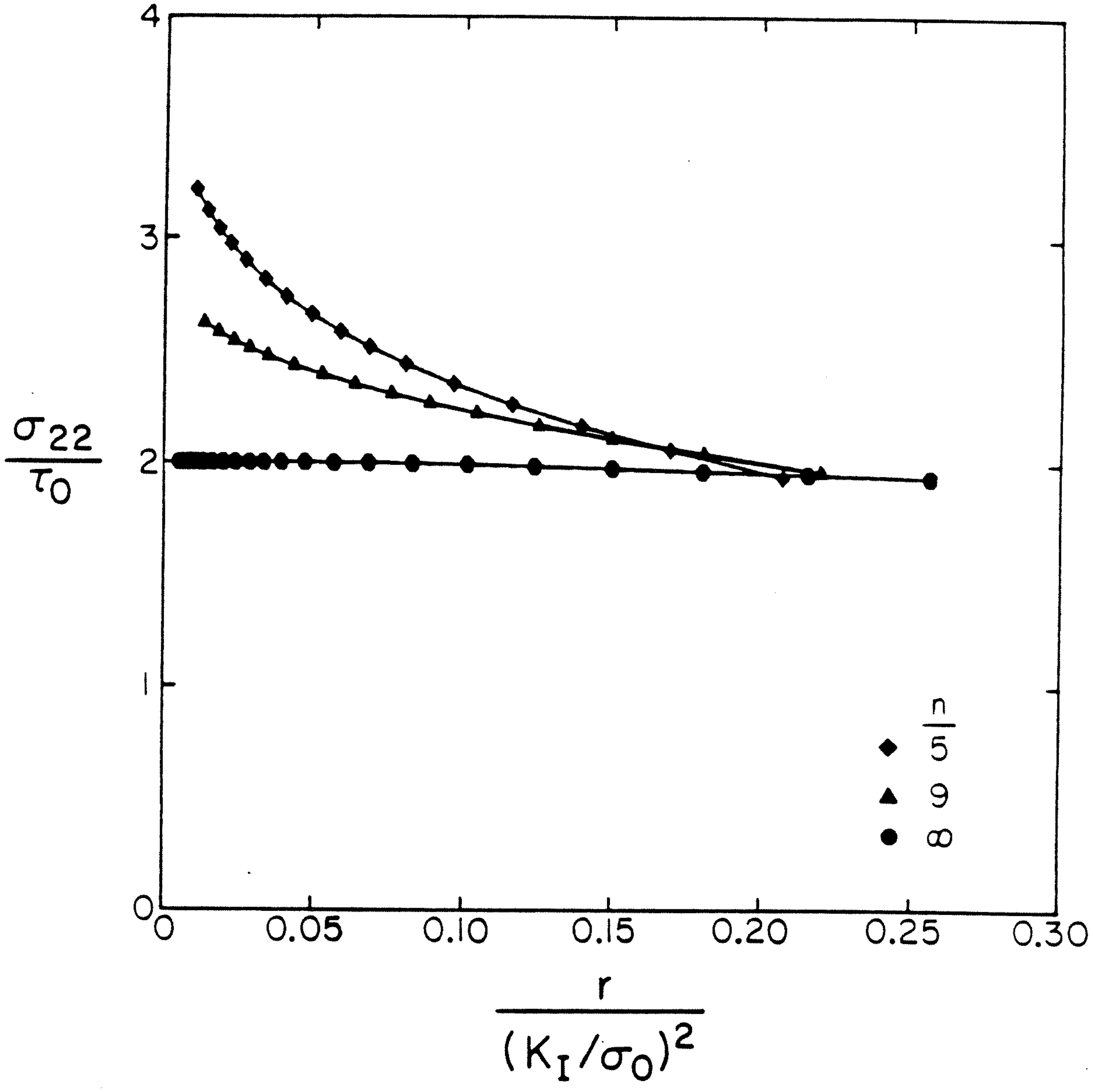

Figure 4.6. *Radial distribution of opening stress ahead of the moving tip.*

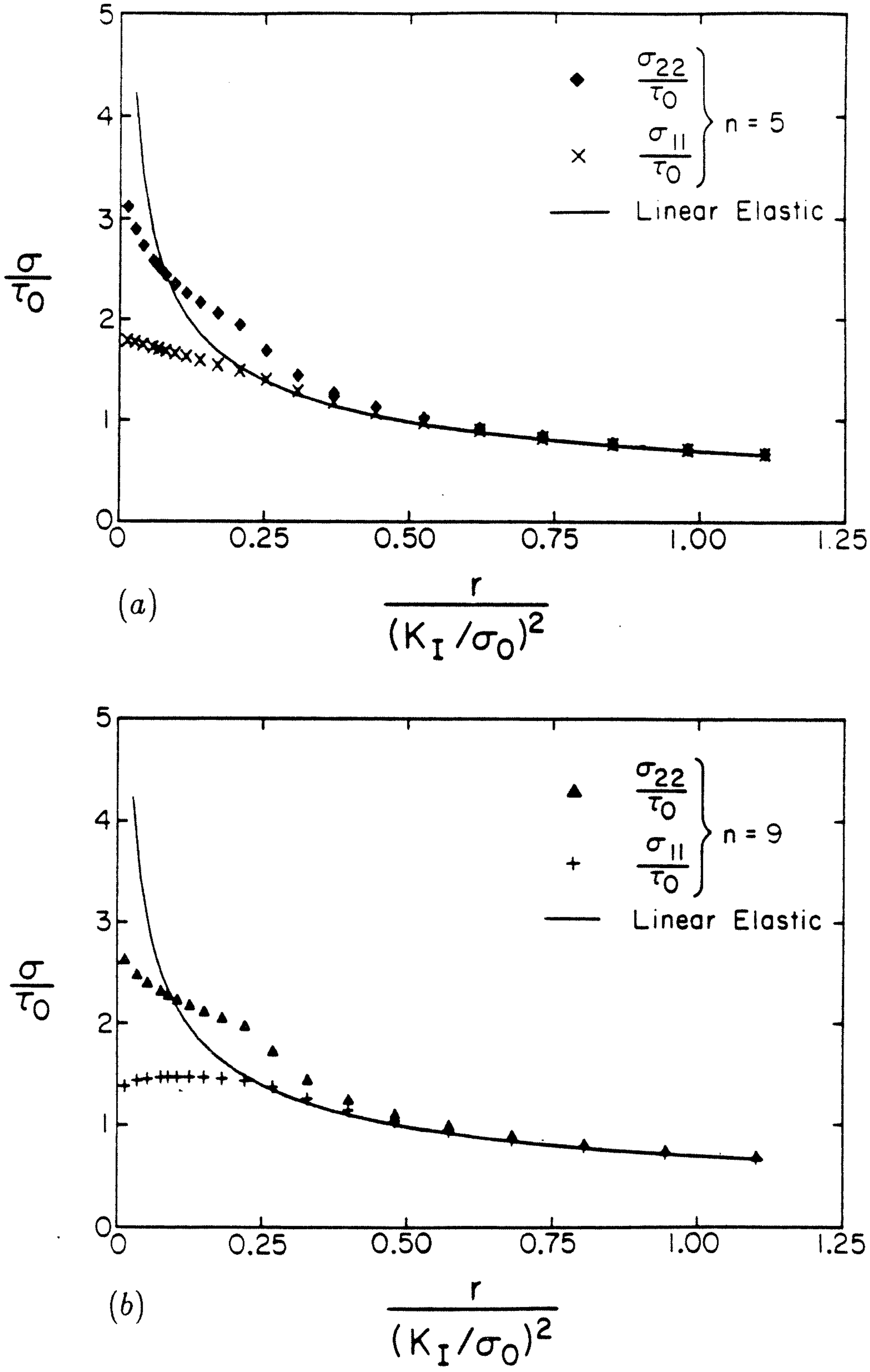

Figure 4.7. *Comparison of radial stress distribution ahead of the moving tip as given by the K_I field (solid line) with the finite element solution for* a) *n=5 and* b) *n=9.*

$r > 1.5R_p$.

Near-tip Angular Distribution of Stresses

The near-tip angular distribution of the normalized polar stress components is shown in Fig. 4.8 for $n = 5$ and 9 along with the perfect plasticity solution of [4.2]. The centroidal values of stresses in the elements lying on a rectangular contour surrounding the moving crack tip, with an average radius of $0.018(K_I/\sigma_0)^2$ (which is within $0.08R_p$), have been used to make this plot. The angular variation along the above contour of the Von Mises equivalent stress, $\sigma_{eqv} = (\frac{3}{2}s_{ij}s_{ij})^{1/2}$, which has been made dimensionless by σ_0, is also shown in the figure.

The assertion made earlier, that no secondary (plastic) reloading was observed (as $\theta \to 180°$) for any level of hardening, is confirmed from this figure. Also, elastic unloading occurs for angles θ greater than about 65°, 55° and 45° for $n = 5, 9$ and ∞, respectively, although it is not obvious from this figure for the hardening cases. The near-tip angular stress variation for the hardening materials appears to be qualitatively similar to the perfectly plastic case. This seems to agree with the assumption made by Gao and Hwang [4.11], regarding the invariance with respect to hardening, of the angular distribution of the asymptotic stress field (see Eqn.(4.1.1)). As noted in [4.2], the stress variation within the active plastic zone for the perfectly plastic case is in very good agreement with the distribution in a centered fan, as predicted by Rice [4.4].

Crack Opening Profiles

The normalized crack opening displacement, $\delta/(J/\sigma_0)$, versus normalized distance, $x_1/(K_I/\sigma_0)^2$, along the crack flank is shown in Fig. 4.9 for the two hardening cases, $n = 5$ and 9, when the crack grows under fixed applied load. This profile was obtained after twenty crack growth steps and was self-similar in normalized form, in the sense that it was almost identical for different levels of crack growth (as in

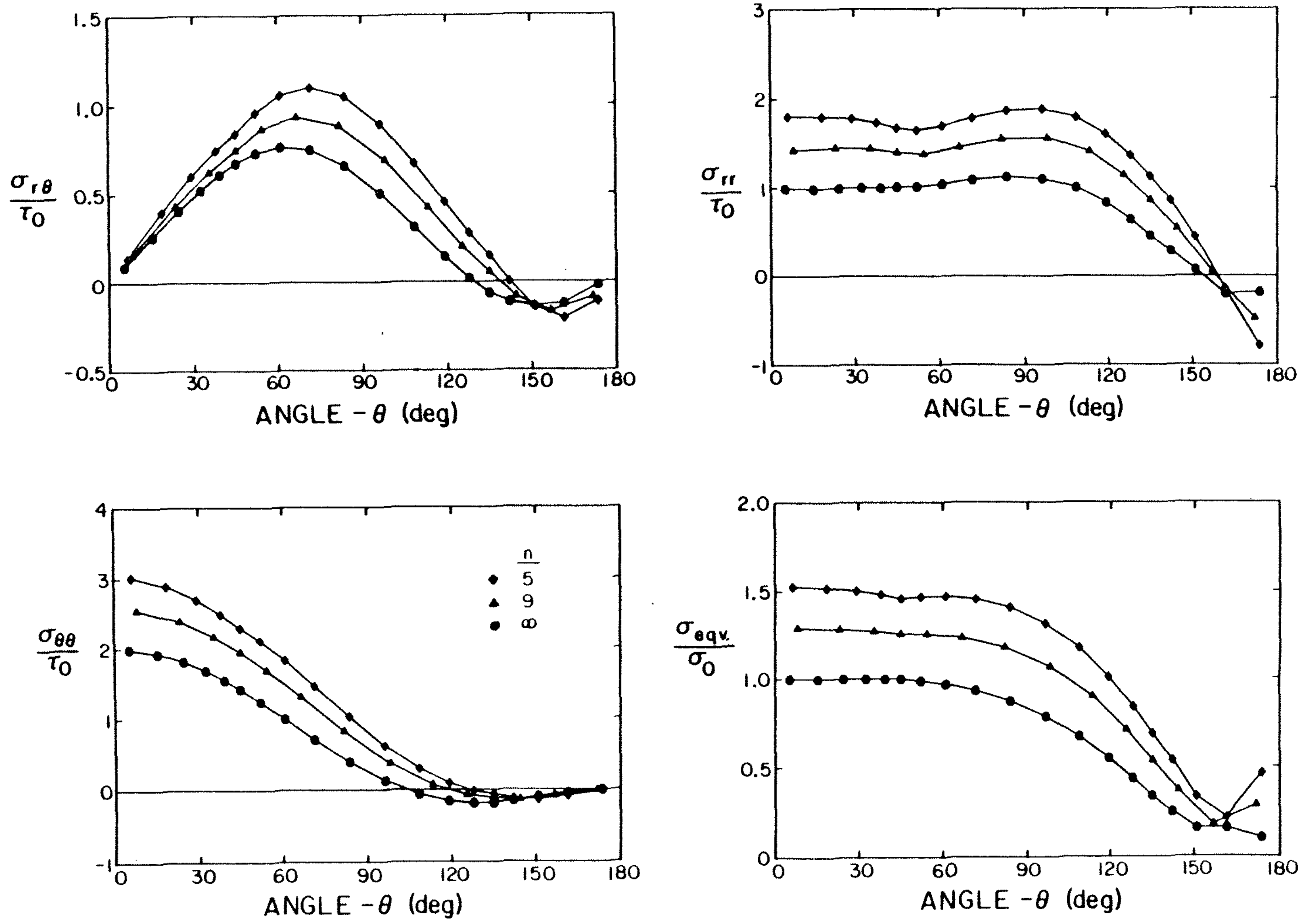

Figure 4.8. *Near-tip angular distribution of the normalized polar stress components and the Von Mises equivalent stress at a distance of* $0.018(K_I/\sigma_0)^2$ *from the moving tip.*

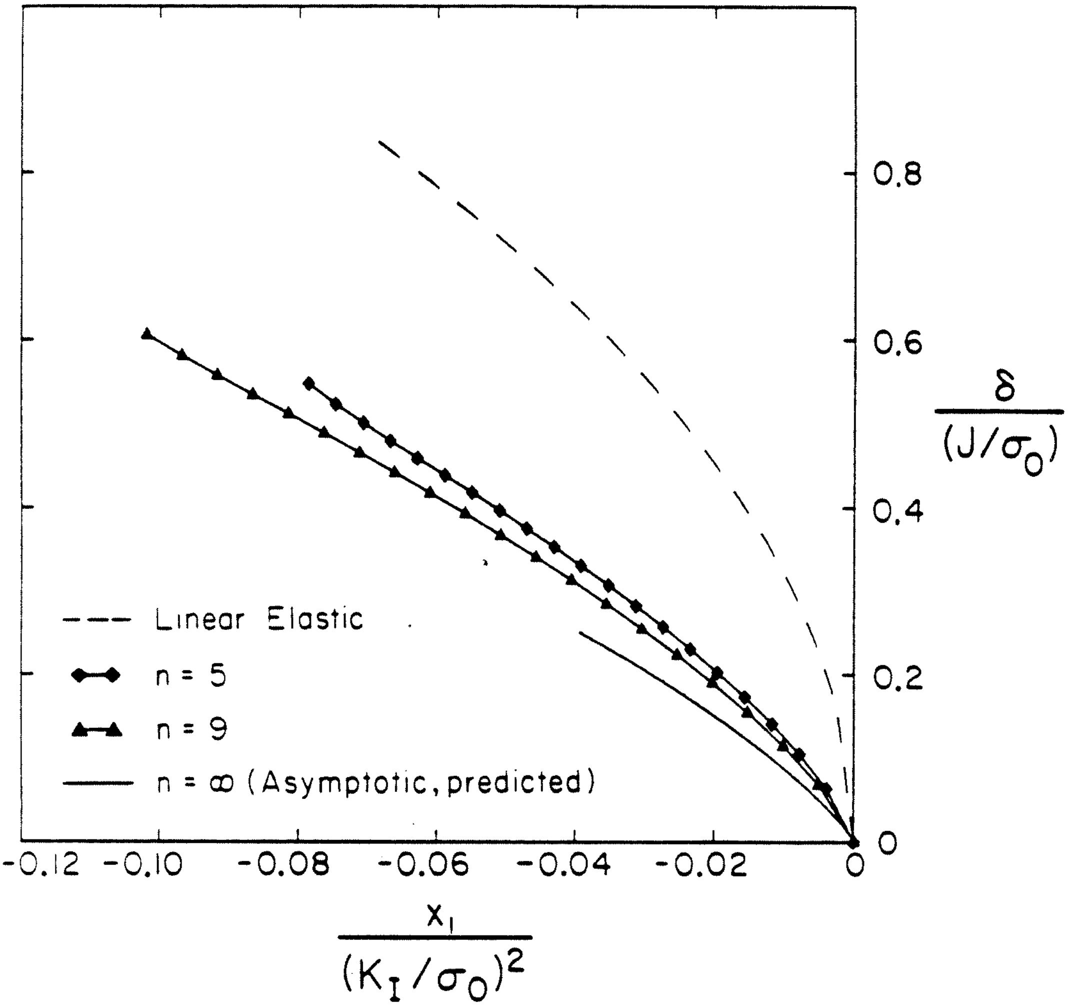

Figure 4.9. *Numerically obtained crack opening profiles for quasi-static crack growth under fixed applied load for n=5 and 9. The dashed line is the linear elastic asymptotic solution and the solid line is the asymptotic crack displacement for steady-state crack growth in a perfectly plastic solid, as predicted by the analysis of [4.2].*

[4.2]). The crack opening profile for a linear elastic material is also shown by the dashed line in the figure.

The steady-state asymptotic opening profile for a crack growing in a perfectly plastic material, as predicted by the analysis of [4.2], is indicated by the solid line in the figure. This is given by [4.2],

$$\frac{\delta}{(J/\sigma_0)} = \beta\eta \ln\left(\frac{es}{\eta}\right), \tag{4.3.1}$$

where

$$\eta = r/(K_I/\sigma_0)^2.$$

In the above equation e is the base of the natural logarithm. In [4.2], the parameters β and s which occur in (4.3.1) were estimated as 1.70 and 0.60, respectively, from a best-fit to the near-tip crack displacement increment, obtained from the numerical solution for the non hardening case.

It can be noticed from Fig. 4.9 that the crack profiles vary considerably with the hardening level. This was also observed by Dean [4.17] from his steady-state solution for plane stress crack growth in linear hardening solids. This also appears to be true for the crack profiles obtained under anti-plane shear by Dean and Hutchinson [4.15]. However, the crack profiles under Mode I plane strain show comparatively less variation with the hardening level, at least near the crack tip [4.15]. Also, as opposed to the blunted shapes obtained for the stationary problem [4.1], the crack opening profiles during growth (Fig. 4.9) exhibit a sharp shape. This is directly traceable to the permanence of plastic deformation [4.3].

Ductile Crack Growth Criterion

Rice and Sorensen [4.13] and Rice et al.[4.5] proposed that a critical opening displacement, $\delta = \delta_C$, should be maintained at a small microstructural distance, r_c, behind the crack tip for continued crack growth. If one employs the above criterion for initiation and continuation of crack growth as in [4.15], it is possible to examine the potential for stable crack growth from the microstructural viewpoint. To this end, the self-similar crack profiles shown in Fig. 4.9 for crack growth under fixed applied load were taken as steady-state profiles and were used to generate a plot of $\delta/(\epsilon_0 \mathrm{r})$ versus $\mathrm{r}/(\mathrm{K_{SS}}/\sigma_0)^2$. This is shown in Fig. 4.10*b* for the two cases of hardening, n = 5 and 9. The opening displacement for the stationary crack given in [4.1] was used similarly to obtain the variation of $\delta/(\epsilon_0 \mathrm{r})$ versus $\mathrm{r}/(\mathrm{K_{IC}}/\sigma_0)^2$ as shown in Fig. 4.10*a*.

For a given value of the microscale parameter $\lambda_\mathrm{m} = \delta_\mathrm{C}/(\epsilon_0 \mathrm{r_c})$, the value of $\mathrm{r_c}/(\mathrm{K_{SS}}/\sigma_0)^2$ can be obtained from the abscissa of Fig. 4.10*b* corresponding to steady-state crack growth. The value of $\mathrm{r_c}/(\mathrm{K_{IC}}/\sigma_0)^2$ may be obtained similarly from Fig. 4.10*a* for initiation of crack growth. These two quantities can be used to compute the ratio of $\mathrm{J_{SS}}/\mathrm{J_{IC}} = (\mathrm{K_{SS}}/\mathrm{K_{IC}})^2$, corresponding to the chosen value of the microscale parameter λ_m. The variation of $\mathrm{J_{SS}}/\mathrm{J_{IC}}$ versus $\delta_\mathrm{C}/(\epsilon_0 \mathrm{r_c})$, calculated as indicated above for n = 5 and 9, is shown in Fig. 4.11. On comparing Figs. 4.10*a* and *b*, it can be seen that the influence of hardening on the relationship between $\mathrm{J_{SS}}/\mathrm{J_{IC}}$ and $\delta_\mathrm{C}/(\epsilon_0 \mathrm{r_c})$ arises mainly due to the results in Fig. 4.10*b*, corresponding to steady-state crack growth. The effect of hardening on the variation of $\delta/(\epsilon_0 r)$ with respect to $\mathrm{r}/(\mathrm{K_{IC}}/\sigma_0)^2$ at initiation is not so significant, as can be seen from Fig. 4.10*a*.

For comparison purposes, the variation of $\mathrm{J_{SS}}/\mathrm{J_{IC}}$ with respect to $\delta_\mathrm{C}/(\epsilon_0 \mathrm{r_c})$ for the elastic-perfectly plastic material, which was deduced in [4.2] from the steady-state asymptotic crack profile (4.3.1), is also shown in Fig. 4.11 by the solid line. This relation is given by [4.2],

$$\frac{J_{SS}}{J_{IC}} = \frac{\alpha}{s\lambda_m} e^{(\lambda_m/\beta - 1)} , \tag{4.3.2}$$

where $\lambda_\mathrm{m} = \delta_\mathrm{C}/(\epsilon_0 \mathrm{r_c})$ and the parameters α, β and s were estimated in [4.2] as 0.82,

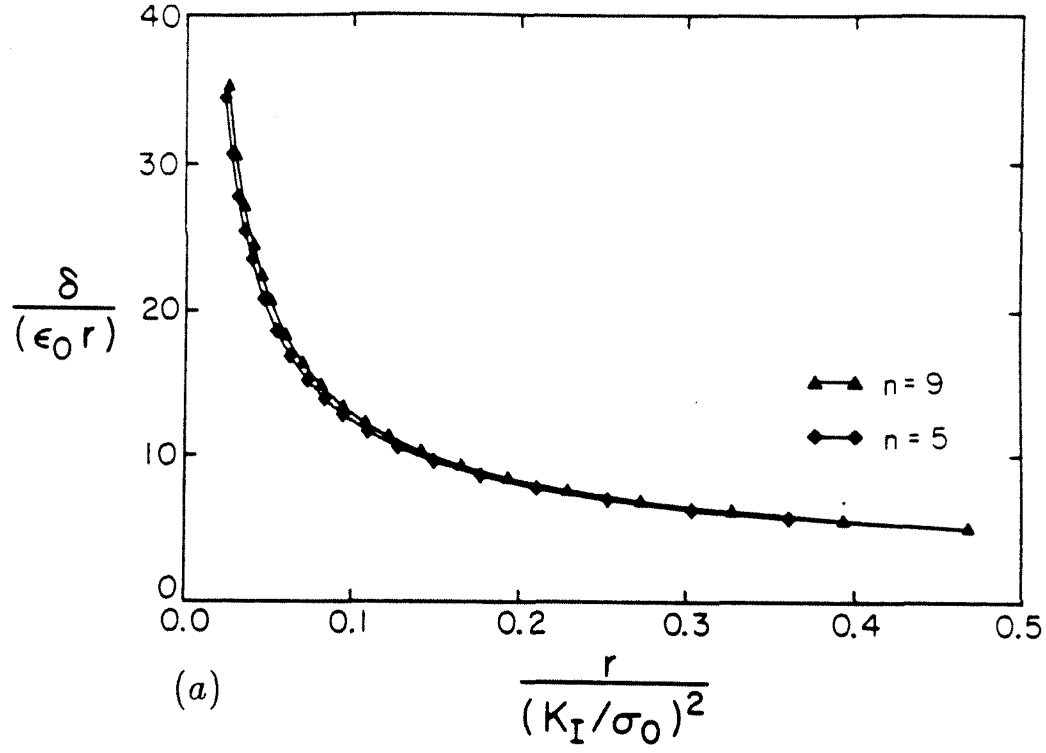

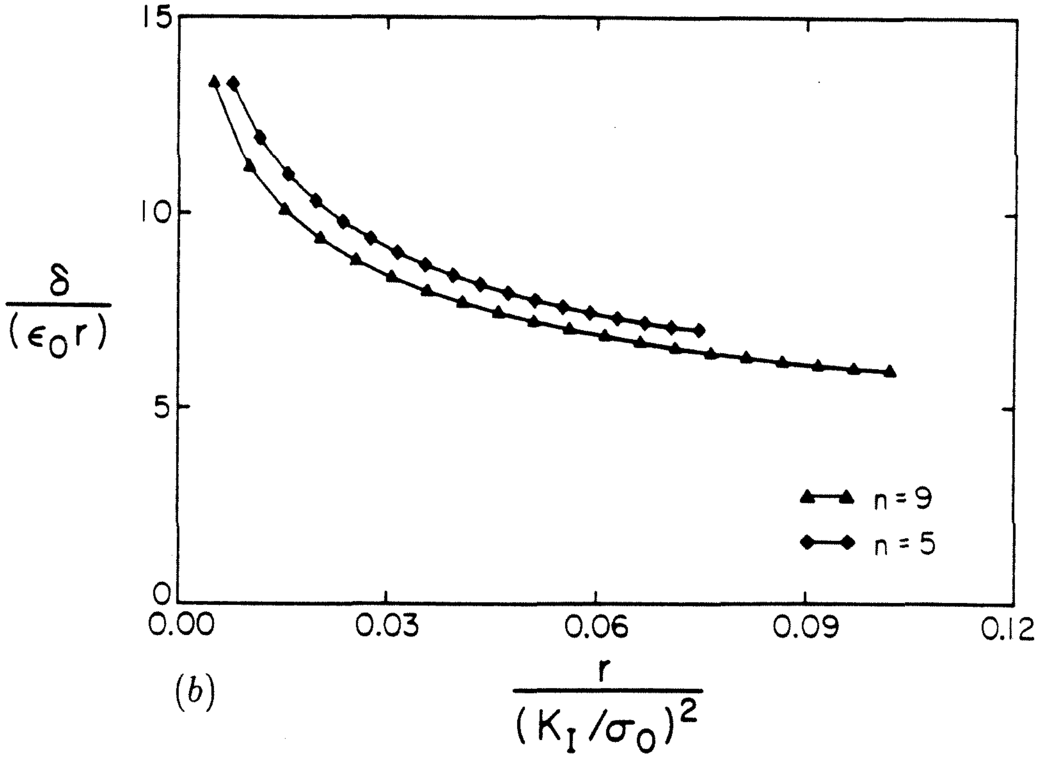

Figure 4.10. *Variation of $\delta/(\epsilon_0 r)$ with normalized distance along the crack flank for a) the stationary problem [4.1] and b) quasi-static crack growth under fixed applied load.*

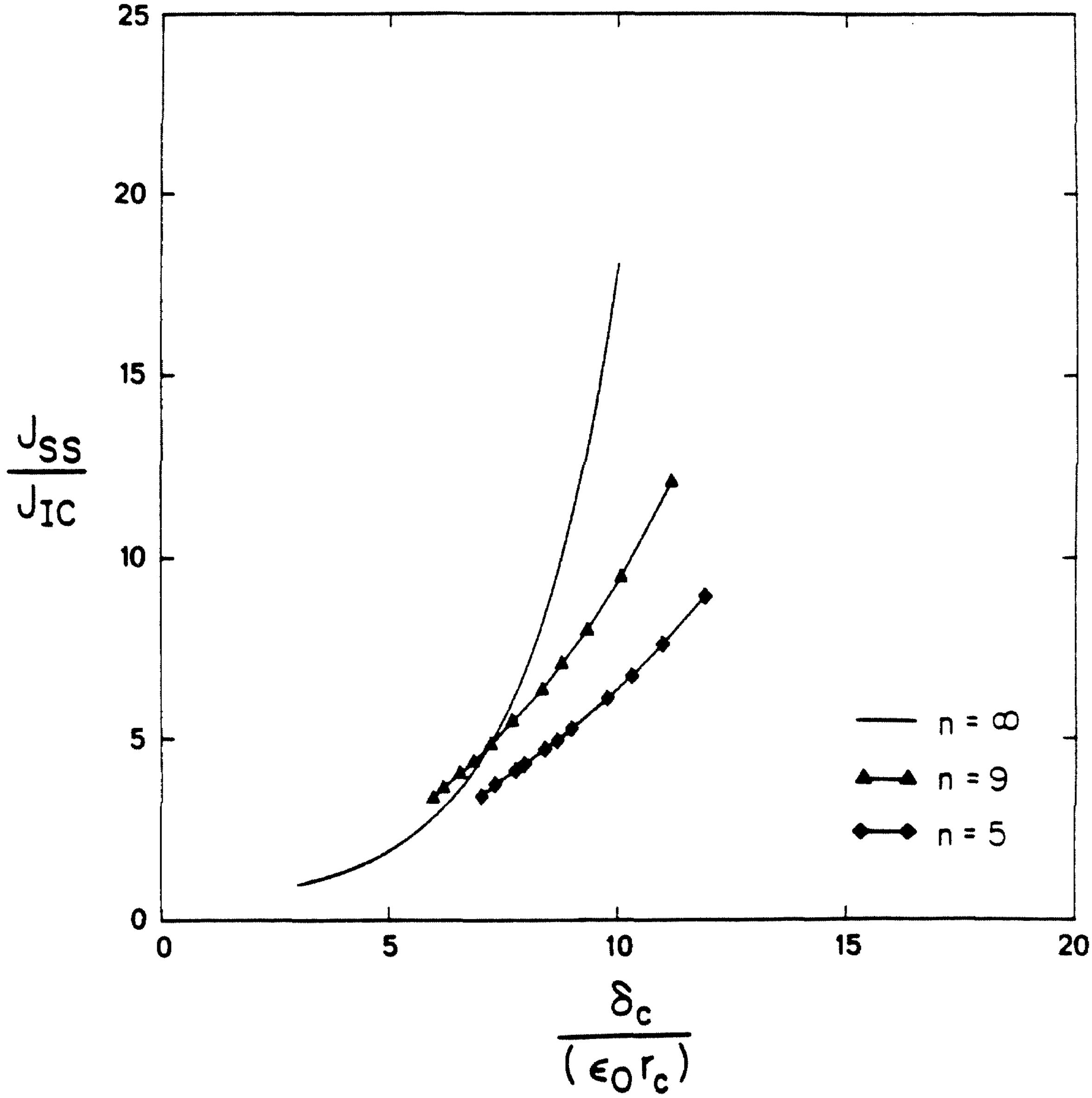

Figure 4.11. *Influence of hardening on J_{SS}/J_{IC} in Mode I plane stress, as predicted by the critical displacement criterion, for continued crack growth. The solid line is the perfect plasticity result of [4.2].*

1.70 and 0.60, respectively. It can be seen from Fig. 4.11 that in the range $\lambda_m > 8.0$, the ratio J_{SS}/J_{IC} may increase significantly with a decrease in hardening. For example, corresponding to a value of $\lambda_m = 9.5$, the ratio J_{SS}/J_{IC} is 5.8, 8.3 and 14.1 for $n = 5, 9$ and ∞, respectively. Thus, the potential for stable crack growth may be grossly overestimated by a calculation based on the perfect plasticity idealization, when the material actually possesses some hardening. Hence, predictions about the extent of stable crack growth based on the perfectly plastic model (as made in [4.2]) may be unconservative for a hardening material when the microscale parameter exceeds a value of about 8. A qualitatively similar conclusion was reached in anti-plane shear and Mode I plane strain as well, by Dean and Hutchinson [4.15].

In the light of the above observation, one is compelled to examine the effects of kinematic hardening and corner formation on the yield surface, which may occur during the nonproportional loading experienced by a material particle near the crack tip. It is not clear to what extent these factors will affect the potential for stable crack growth under plane stress conditions. Dean and Hutchinson [4.15] found that the influence of corner formation was not as significant as strain hardening from their numerical results for anti-plane shear crack growth. However, Lam and McMeeking [4.16] observed that both corner formation and kinematic hardening further reduced the potential for stable crack growth in Mode I plane strain. Thus, in this sense, even the results based on a smooth yield surface with isotropic hardening may be unconservative. It is suggested that such effects should be investigated in Mode I plane stress.

Comparison of results for the two Crack Growth Histories

In order to study the influence of increase in applied load, as would be observed in an experiment during the initial phase of stable crack extension, a crack growth history at a constant value of $T = 1.5$ was also simulated in this work (Fig. 4.2).

Only the material with $n = 9$ was considered in this investigation.

The active plastic zones obtained for this crack growth history compared very closely with that shown in Fig. 4.3, both in shape and size. During the first few crack growth steps, the active plastic zone assumed the sharpened shape of Fig. 4.3, which did not change with subsequent crack advance. The values of θ_p and R_p were about 55° and $0.24(K_I/\sigma_0)^2$ as reported earlier, based on the first crack growth history (at fixed applied load).

The plastic strains ahead of the moving crack tip exhibited a tendency to converge rapidly to an invariant distribution during the first few crack growth steps as in the earlier analysis (Fig. 4.4). The normalized plastic strains ahead of the tip at the end of the fifteenth crack growth step under $T = 1.5$ is shown in Fig. 4.12 and is compared with the result given in Fig. 4.5 for crack growth at $T = 0$. As expected, the plastic strains for $T = 1.5$ are slightly higher due to the influence of increase in applied load with crack growth.

The radial distribution of stresses ahead of the propagating crack tip for the two histories is shown in Fig. 4.13 in the nondimensional form, $\sigma_{\alpha\beta}/\tau_0$ versus $r/(K_I/\sigma_0)^2$. The effect of the increase in applied load on the stress field seems to be less significant than that on the deformation field. Also, the near-tip angular stress distribution for the two histories were almost identical. Finally, the nondimensional crack opening displacement, $\delta/(J/\sigma_0)$, as a function of position on the crack flank, $x_1/(K_I/\sigma_0)^2$, is shown in Fig. 4.14 for $T = 0$ and 1.5. Due to the increase in applied load, the crack opening displacement for $T = 1.5$ is higher than that for $T = 0$.

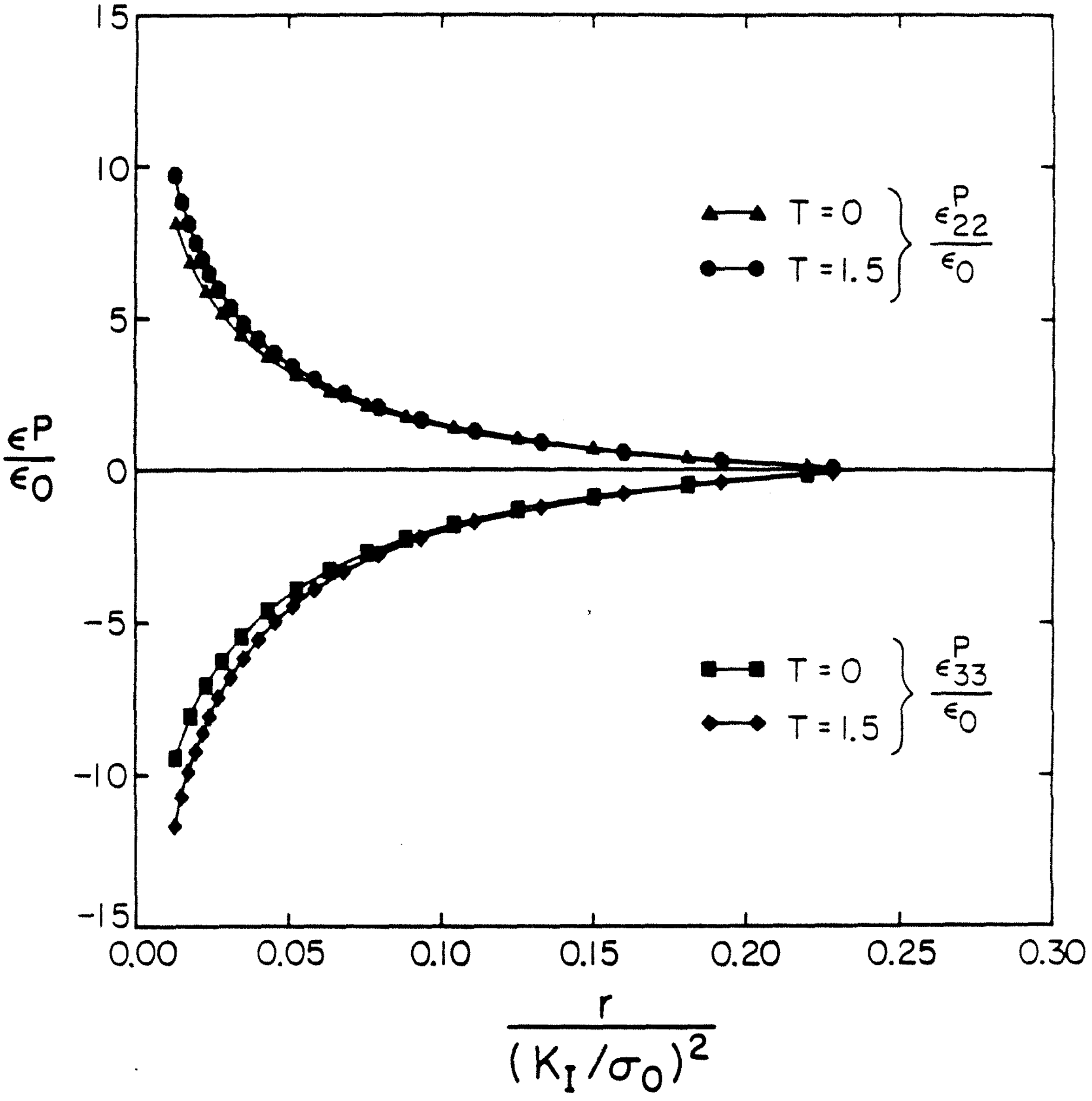

Figure 4.12. *Comparison of the radial distribution of plastic strains ahead of the tip for the two crack growth histories that were simulated for* $n=9$.

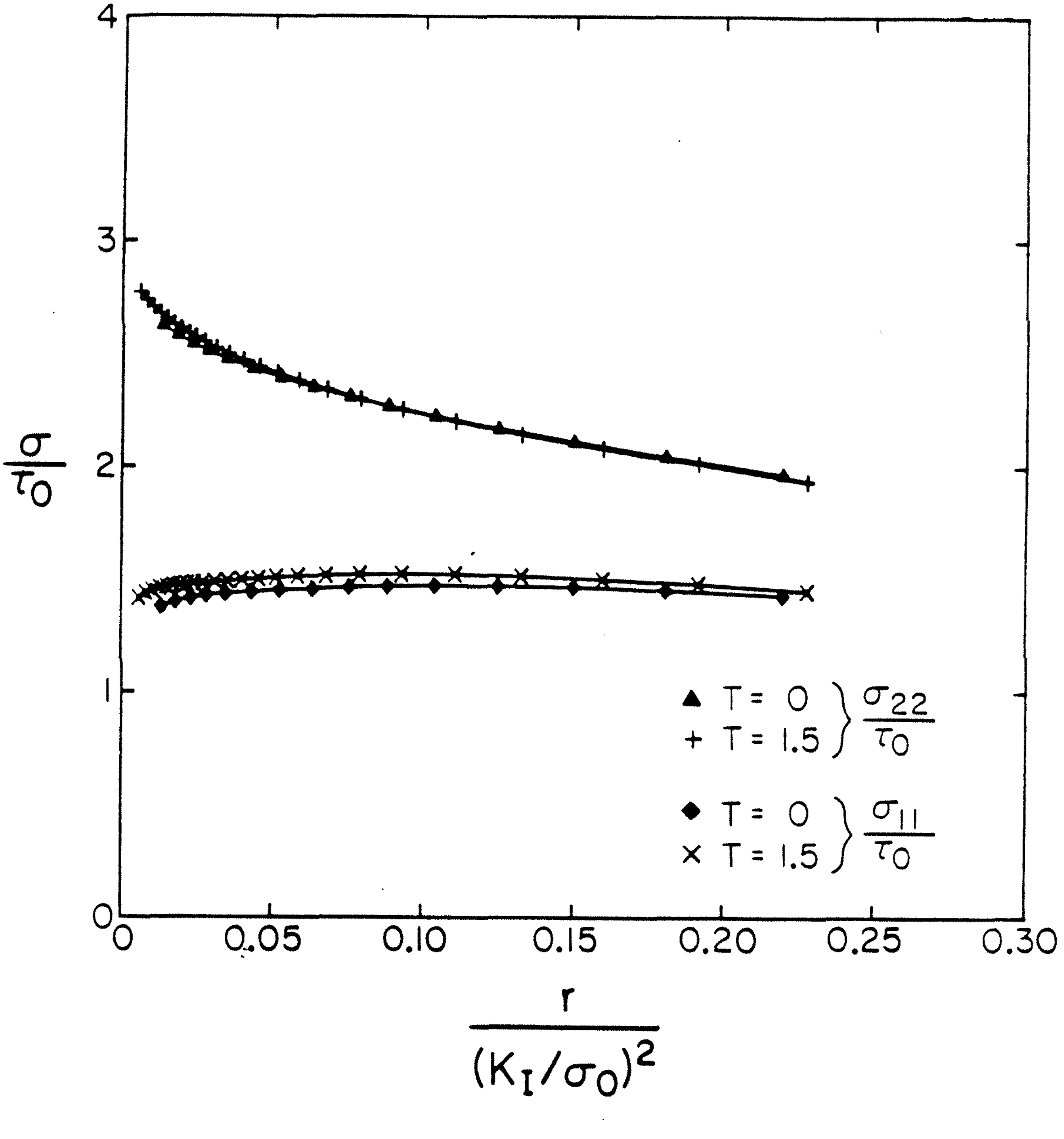

Figure 4.13. *Radial stress distribution ahead of the tip for n=9 for the two crack growth histories.*

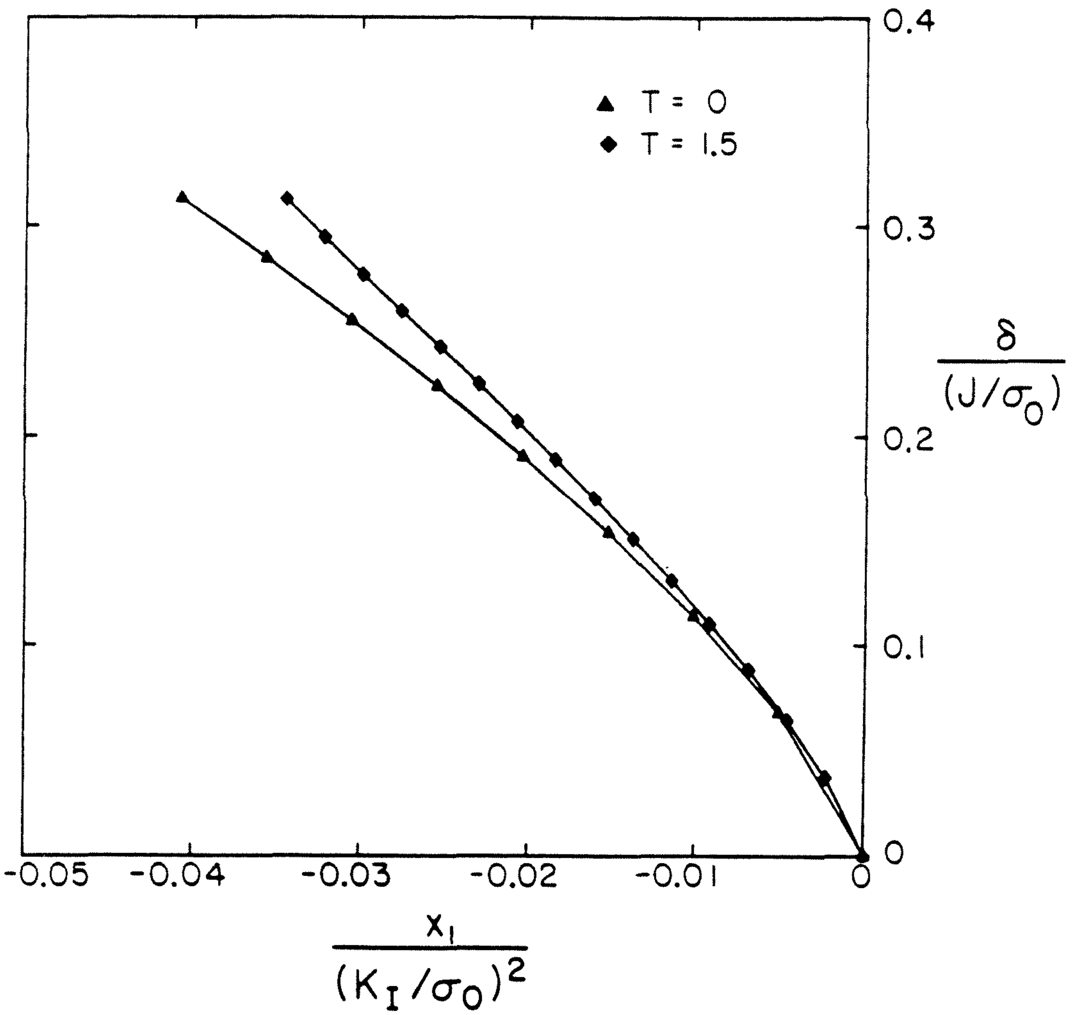

Figure 4.14. *Effect of increase in applied load at T=1.5 on the near-tip crack displacement for n=9.*

CHAPTER REFERENCES

4.1. Narasimhan, R. and Rosakis, A. J. (1986), "A Finite Element Analysis of Small-Scale Yielding near a Stationary Crack under Plane Stress," Caltech Report SM 86-21, submitted for publication to *Journal of Mechanics and Physics of Solids.*

4.2. Narasimhan, R. , Rosakis, A. J. and Hall, J. F. (1986), "A Finite Element Study of Stable Crack Growth under Plane Stress Conditions in Elastic-Perfectly Plastic Solids," Caltech Report SM 86-22, submitted for publication to *Journal of Applied Mechanics.*

4.3. Rice, J. R. (1975), "Elastic-Plastic Models for Stable Crack Growth," *Mechanics and Mechanisms of Crack Growth*, M. J. May ed. , British Steel Corp. Physical Metallurgy Centre Publication, Sheffield, pp. 14-39.

4.4. Rice, J. R. (1982), "Elastic-Plastic Crack Growth," *Mechanics of Solids*, H. G. Hopkins and M. J. Sewell eds. , Pergamon Press, Oxford, pp. 539-562.

4.5. Rice, J. R. , Drugan, W. J. and Sham. T. L. (1980), "Elastic-Plastic Analysis of Growing Cracks," *Fracture Mechanics: Twelfth Conference*, ASTM STP 700, pp. 189-221.

4.6. Drugan, W. J. , Rice, J. R. and Sham, T. L. (1982), "Asymptotic Analysis of Growing Plane Strain Tensile Cracks in Elastic-Ideally Plastic Solids," *Journal of Mechanics and Physics of Solids*, Vol. 30, 447-473.

4.7. Gao, Y. C. (1980), "Elastic-Plastic Field at the Tip of a Crack Growing Steadily in a Perfectly Plastic Medium," *Acta Mechanica Sinicia*(in Chinese), No. 1, 48-56.

4.8. Slepyan, L. I. (1974), "Growing Cracks during Plane Deformation of an Elastic-Plastic body," *Izv. Akad. Nauk. SSSR, Mekhanika Tverdogo Tela,* Vol. 9, 57-67.

4.9. Amazigo, J. C. and Hutchinson, J. W. (1977), "Crack-Tip Fields in Steady Crack Growth with Linear Strain-Hardening," *Journal of Mechanics and Physics of Solids,* Vol. 25, 81-97.

4.10. Castañeda, P. P. (1985), "Asymptotic Fields in Steady Crack Growth with Linear Strain-Hardening," Harvard University Report MECH-69.

4.11. Gao, Y. C. and Hwang, K. C. (1981), "Elastic-Plastic Fields in Steady Crack Growth in a Strain Hardening Material," Proceedings of Fifth International Conference on Fracture, D. Francois ed. , Pergamon Press, New York, Vol. 2, 669-682.

4.12. Sorensen, E. P. (1978), "A Finite Element Investigation of Stable Crack Growth in Anti-Plane Strain," *International Journal of Fracture*, Vol. 14, 485-500.

4.13. Rice, J. R. and Sorensen, E. P. (1978), "Continuing Crack-Tip Deformation and Fracture for Plane Strain Crack Growth in Elastic-Plastic Solids," *Journal of Mechanics and Physics of Solids*, Vol. 26, 163-186.

4.14. Sham, T. L. (1982), "A Finite Element Study of Asymptotic Near-Tip Fields for Mode I Plane Strain Cracks in Elastic Ideally Plastic Solids," Ph. D. dissertation, Brown University, Providence.

4.15. Dean, R. H. and Hutchinson, J. W. (1980), "Quasi-Static Steady Crack Growth in Small-Scale Yielding," *Fracture Mechanics: Twelfth Conference*, ASTM STP 700, pp. 385-400.

4.16. Lam, P. S. and McMeeking, R. M. (1984), "Analysis of Steady Quasi-Static Crack Growth in Plane Strain Tension in Elastic-Plastic Materials with Non-Isotropic Hardening," *Journal of Mechanics and Physics of Solids*, Vol. 32, 395-414.

4.17. Dean, R. H. (1983), "Elastic-Plastic Steady Crack Growth in Plane Stress," *Elastic-Plastic Fracture: Second Symposium, Volume I-Inelastic Crack Analysis*, ASTM STP 803, pp. I-39-I-51.

4.18. Broek, D. (1968), "Some Considerations of Slow Crack Growth," *International Journal of Fracture*, Vol. 4, 19-34.

4.19. Green, G. and Knott, J. F. (1975), "On Effects of Thickness on Ductile Crack Growth in Mild Steel," *Journal of Mechanics and Physics of Solids*, Vol. 23, 167-183.

4.20. Hermann, L. and Rice, J. R. (1980), "Comparison of Experiment and Theory for Elastic-Plastic Plane Strain Crack Growth," *Metal Science*, Vol. 14, 285-291.

4.21. Chitaley, A. D. and McClintock, F. A. (1971), "Elastic-Plastic Mechanics of Steady Crack Growth under Anti-Plane Shear," *Journal of Mechanics and Physics of Solids*, Vol. 19, 147-163.

APPENDIX A

EQUILIBRIUM ITERATION AND STRESS COMPUTATION

Newton-Raphson method for equilibrium iteration

It was observed in Sec.(2.2) that an iterative Newton-Raphson method was used in the solution of the incremental equilibrium Equations (2.2.11). This procedure is summarized below for the k^{th} equilibrium iteration of the $(\mathrm{t}+\Delta \mathrm{t})^{\mathrm{th}}$ time step.

1) The externally applied load is increased and $\underline{\mathrm{F}}(\mathrm{t}+\Delta \mathrm{t})$ is calculated.
2) The tangent stiffness matrix $\underline{\mathrm{K}}_{\mathrm{T}}^{\mathrm{k}-1}(\mathrm{t}+\Delta \mathrm{t})$ and the vector $\underline{\mathrm{P}}^{\mathrm{k}-1}(\mathrm{t}+\Delta \mathrm{t}) = \int_{\mathrm{R}} \underline{\mathrm{B}}^{\mathrm{T}} \underline{\sigma}^{\mathrm{k}-1}(\mathrm{t}+\Delta \mathrm{t}) \mathrm{dA}$ are calculated. For the first iteration of the time step (k=1), the above vector is computed from the converged solution at the end of the previous time step as, $\underline{\mathrm{P}}^{0}(\mathrm{t}+\Delta \mathrm{t}) = \int_{\mathrm{R}} \underline{\mathrm{B}}^{\mathrm{T}} \underline{\sigma}(\mathrm{t}) \mathrm{dA}$.
3) The following matrix equation is solved by Gauss elimination:

$$\underline{\mathrm{K}}_{\mathrm{T}}^{\mathrm{k}-1} \Delta \underline{\mathrm{U}}^{\mathrm{k}} = \underline{\mathrm{F}}(\mathrm{t}+\Delta \mathrm{t}) - \underline{\mathrm{P}}^{\mathrm{k}-1} = \Delta \underline{\mathrm{R}}^{\mathrm{k}} .$$

4) The nodal displacements and element strains are updated as follows,

$$\underline{\mathrm{U}}^{\mathrm{k}}(\mathrm{t}+\Delta \mathrm{t}) = \underline{\mathrm{U}}^{\mathrm{k}-1}(\mathrm{t}+\Delta \mathrm{t}) + \Delta \underline{\mathrm{U}}^{\mathrm{k}}$$

$$\underline{\epsilon}^{\mathrm{k}}(\mathrm{t}+\Delta \mathrm{t}) = \underline{\mathrm{B}}\, \underline{\mathrm{U}}^{\mathrm{k}}(\mathrm{t}+\Delta \mathrm{t}) .$$

For the first iteration of the time step (k=1),

$$\underline{\mathrm{U}}^{1}(\mathrm{t}+\Delta \mathrm{t}) = \underline{\mathrm{U}}(\mathrm{t}) + \Delta \underline{\mathrm{U}}^{1} .$$

5) In order to prevent fictitious (numerical) elastic unloading of elements in some parts of the plastic zone during the subsequent iterations ($\mathrm{k} > 1$) of the time step, a path independent scheme is used in this numerical scheme to update element stresses. The stresses are estimated by integrating from the values

at the end of the previous accepted equilibrium configuration to the current iteration of this time step by using the cumulative strains as follows [2.4],

$$\underline{\sigma}^{k}(t+\Delta t) = \underline{\sigma}(t) + \int_{\underline{\epsilon}(t)}^{\underline{\epsilon}^{k}(t+\Delta t)} \underline{D}\, d\underline{\epsilon}\ .$$

An explicit method was employed to evaluate the integral in the above equation.

6) The Euclidean norm of the out-of-balance force vector $\Delta\underline{R}^{k}$ (see Step(3)) and the internal energy increment are checked for convergence by comparing with the corresponding values at the start of the iteration process as [2.5],

$$\|\Delta\underline{R}^{k}\| \leq \delta_F \|\Delta\underline{R}^{1}\|$$

$$\Delta\underline{U}^{k}\,.\,\Delta\underline{R}^{k} \leq \delta_E \Delta\underline{U}^{1}\,.\,\Delta\underline{R}^{1}\ ,$$

where δ_F and δ_E are small, preset tolerances.

If convergence is *not achieved*, control is returned to Step(2) to perform the next iteration.

If convergence is *achieved*, control is returned to Step(1) to perform the next time step.

Explicit Integration of Incremental Constitutive law

The method of stress computation mentioned in Sec.(2.2) is outlined for an isotropic hardening solid below.

1) After solving the finite element equilibrium equations for the nodal displacement increments $\Delta\underline{U}$, the strain increment $\Delta\underline{\epsilon}$ is obtained as

$$\Delta\underline{\epsilon} = \underline{B}\,\Delta\underline{U}\ ,$$

where $\underline{B}$ is the strain-displacement matrix.

2) An elastic estimate $\Delta\underline{\sigma}^{E}$ for the stress increment is computed as

$$\Delta\underline{\sigma}^{E} = \underline{C}\,\Delta\underline{\epsilon}\ .$$

3) A trial stress state $\underline{\sigma}^{\mathrm{E}} = \underline{\sigma}^0 + \Delta\underline{\sigma}^{\mathrm{E}}$ is calculated from the stress state $\underline{\sigma}^0$ at the beginning of the iteration. Here $\underline{\sigma}^0$ is taken to be inside the yield surface (Fig. A.1) for the sake of definiteness.

4) If $\mathrm{F}(\underline{\sigma}^{\mathrm{E}}) - (\bar{\sigma}^0)^2 \leq 0$, where $\bar{\sigma}^0$ is the value of $\bar{\sigma}$ at the beginning of the iteration, then the elastic behaviour assumption holds and the remaining steps in this method are omitted. Otherwise, the yield surface has been crossed during the trial stress incrementation (Fig. A.1).

5) The contact stress state $\underline{\sigma}^{\mathrm{C}}$ is obtained as

$$\underline{\sigma}^{\mathrm{C}} = \underline{\sigma}^0 + \mathrm{q}\Delta\underline{\sigma}^{\mathrm{E}} ,$$

where $0 \leq \mathrm{q} < 1$ and $\mathrm{F}(\underline{\sigma}^{\mathrm{C}}) - (\bar{\sigma}^0)^2 = 0$. This condition for the Von Mises yield function leads to a quadratic equation in q. It should be observed that the path from $\underline{\sigma}^0$ to $\underline{\sigma}^{\mathrm{C}}$ constitutes fully elastic material response.

6) A stress state $\underline{\sigma}^{\mathrm{T}}$ is obtained as

$$\begin{aligned}\underline{\sigma}^{\mathrm{T}} &= \underline{\sigma}^{\mathrm{C}} + \underline{\mathrm{C}}\Big((1-\mathrm{q})\Delta\underline{\epsilon} - \frac{\Delta\lambda}{3}\mathrm{F}_{\underline{\sigma}}\Big) \\ &= \underline{\sigma}^{\mathrm{C}} + \Big((\underline{\sigma}^{\mathrm{E}} - \underline{\sigma}^{\mathrm{C}}) - \frac{\Delta\lambda}{3}\underline{\mathrm{C}}\,\mathrm{F}_{\underline{\sigma}}\Big) .\end{aligned}$$

In this equation, $\mathrm{F}_{\underline{\sigma}}$ is taken as the normal to the yield surface at the stress state $\underline{\sigma}^{\mathrm{C}}$. Also, $\Delta\lambda$ is evaluated corresponding to the stress state $\underline{\sigma}^{\mathrm{C}}$.

7) The yield surface is updated as

$$\bar{\sigma}^{\mathrm{F}} = \bar{\sigma}^0 + \mathrm{H}(\bar{\sigma}^0)\Delta\bar{\epsilon}^{\mathrm{p}} ,$$

where $\Delta\bar{\epsilon}^{\mathrm{p}} = \frac{2}{3}\Delta\lambda\bar{\sigma}^0$ and $\mathrm{H}(\bar{\sigma}^0) = \frac{\mathrm{d}\bar{\sigma}}{\mathrm{d}\bar{\epsilon}^{\mathrm{p}}}\rfloor_{\bar{\sigma}^0}$, which can be obtained from (2.2.4) for hardening solids and is set equal to zero for perfect plasticity.

8) Due to the finite nature of the time step, the stress state $\underline{\sigma}^{\mathrm{T}}$ obtained in Step(6) will not (in general) lie on the updated yield surface. $\underline{\sigma}^{\mathrm{T}}$ is then simply scaled

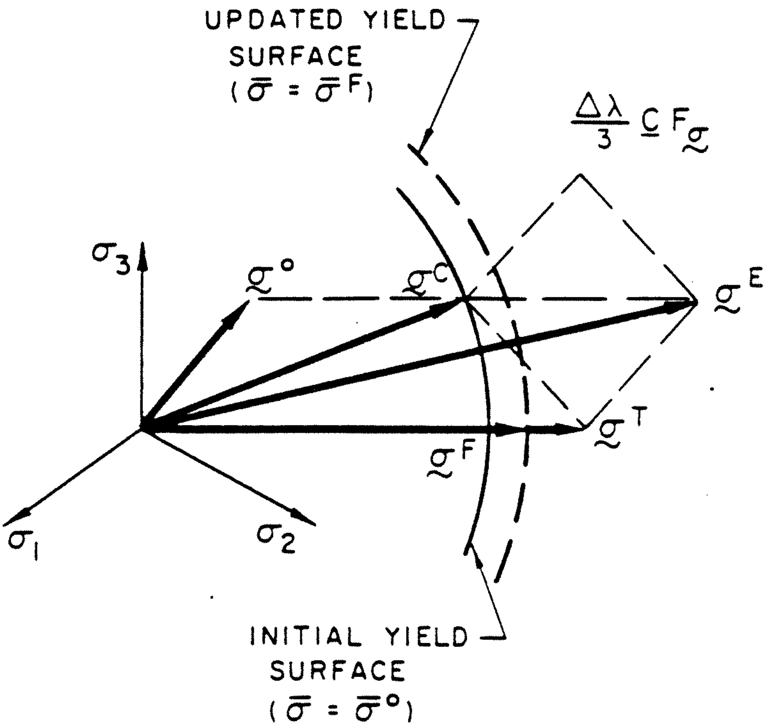

Figure A.1. *Stress computation in the finite element scheme based on an explicit integration of the incremental constitutive law.*

as follows,

$$\underline{\sigma}^{\mathrm{F}} = \left(\frac{\bar{\sigma}^{\mathrm{F}}}{\sqrt{\frac{3}{2}\mathrm{S}_{\mathrm{ij}}^{\mathrm{T}}\mathrm{S}_{\mathrm{ij}}^{\mathrm{T}}}} \right) \underline{\sigma}^{\mathrm{T}} .$$

The path from $\underline{\sigma}^{\mathrm{C}}$ to $\underline{\sigma}^{\mathrm{F}}$ constitutes elastic-plastic material response.

In order to minimise the error due to the use of finite increments, the excess stress $\underline{\sigma}^{\mathrm{E}} - \underline{\sigma}^{\mathrm{C}}$ is divided into m subincrements, and steps (6) to (8) are carried out m times with the subincrements.

APPENDIX B

CONSTRUCTION OF STRESS CHARACTERISTICS

In plane problems involving elastic-perfectly plastic solids, the state of stress within regions that are currently experiencing plastic deformation is governed by the two equilibrium equations and the yield condition. Thus, with the prescription of tractions on the part of the boundary, the stress state becomes statically determinate within plastically deforming regions in the sense that the stresses can be determined without reference to the deformation. It is important to observe that, unlike the case of incompressible plane strain, the solution for stresses within the plastic zone in a plane stress problem may involve regions of hyperbolicity, parabolicity and ellipticity.

In Sec.(3.4), the averaged stresses inside the elements within the active plastic zone, which were obtained from the finite element solution, were used to construct stress characteristics as shown in Fig. 3.8. The procedure employed here to construct stress characteristics follows the general principles outlined by Kachanov [3.22] and is summarized below.

The plane stress Huber-Von Mises yield surface can be represented as an ellipse in principal stress space in the following parametric form,

$$\left.\begin{aligned} \sigma_1 &= 2\tau_0 \cos(\omega - \frac{\pi}{6}) \\ \sigma_2 &= 2\tau_0 \cos(\omega + \frac{\pi}{6}) \\ \omega &= \omega(x_1, x_2) \end{aligned}\right\} , \qquad (B.1)$$

where τ_0 is the yield stress in pure shear. For $\sigma_1 \geq \sigma_2$, the angle ω varies in the range $0 \leq \omega \leq \pi$. It can be shown [3.22] that the equations for the stresses are hyperbolic, parabolic and elliptic, if

$$\left.\begin{aligned} 3-4\cos^2\omega &> 0 \\ &= 0 \\ &< 0 \end{aligned}\right\} , \tag{B.2}$$

respectively.

We first checked the condition (B.2) within each element inside the active plastic zone, using the stresses obtained from the finite element solution. The result of this investigation is shown in Fig. 3.8, where the dotted line separates a region near the tip where the stress state is hyperbolic from a region outside where the stress state is elliptic. At each point of the dotted line the condition for parabolicity (second of (B.2)) is satisfied, and this line has been obtained by appropriate interpolation between elements.

Inside hyperbolic regions, the slopes of the two families of characteristic lines and the Riemann invariants along the characteristics can be obtained as [3.22],

$$\left.\begin{aligned} \frac{dx_2}{dx_1} &= \tan(\varphi-\psi) && for\ \alpha\ lines \\ \frac{dx_2}{dx_1} &= \tan(\varphi+\psi) && for\ \beta\ lines \end{aligned}\right\} , \tag{B.3}$$

and

$$\left.\begin{aligned} \Omega-\varphi &= constant \equiv \xi && for\ \alpha\ lines \\ \Omega+\varphi &= constant \equiv \eta && for\ \beta\ lines \end{aligned}\right\} . \tag{B.4}$$

In the above equations, $\varphi(x_1, x_2)$ is the angle made by the first principal stress direction with the x_1 axis, and the function $\psi(x_1, x_2)$ is defined by,

$$\psi = \frac{\pi}{2} - \frac{1}{2}\arccos\left(\frac{\cot\omega}{\sqrt{3}}\right) , \tag{B.5}$$

where ω is obtained from (B.1) as

$$\cos\omega = \frac{(\sigma_1+\sigma_2)}{2\sqrt{3}\tau_0} . \tag{B.6}$$

Also, the function $\Omega(\omega)$ in (B.4) is defined by

$$\begin{aligned}\Omega(\omega) = -\frac{\pi}{4} + \arcsin\left(\frac{2\cos\omega}{\sqrt{3}}\right) - \frac{1}{4}\arctan\left(\frac{4\cos\omega+3}{\Sigma(\omega)}\right)\\ - \frac{1}{4}\arctan\left(\frac{4\cos\omega-3}{\Sigma(\omega)}\right),\end{aligned} \tag{B.7}$$

where

$$\Sigma(\omega) = \sqrt{3-4\cos^2\omega}\ . \tag{B.8}$$

The values of $\Omega(\omega)$ range from 0 to $-\frac{\pi}{2}$ as ω varies from $\frac{\pi}{6}$ to $\frac{5\pi}{6}$.

From the average stresses within the elements that lie inside the hyperbolic region, the slopes of the two families of characteristics were determined by using Eqn.(B.3). Two small straight lines were drawn at the centroid of each element corresponding to the two characteristic directions. The two families of continuous characteristic lines were then plotted by suitably interpolating between the elements such that the appropriate Riemann function ξ or η as defined in (B.4) remained approximately constant along each line. The net of characteristics thus constructed is shown in Fig. 3.8.

Appendix C

QUASI-STATIC PROPAGATION OF DISCONTINUITY SURFACES

C.1. INTRODUCTION.

A variety of problems of physical interest involving the deformation of elastic-plastic solids may require the admission of discontinuities in the gradients of stresses and velocities (weak discontinuities) or in these quantities themselves (strong discontinuities). Such discontinuities may occur within regions that are currently deforming plastically or at elastic-plastic boundaries. These possibilities have received wide attention for rigid - perfectly plastic solids in plane strain (Hill [C.3]) and in generalized plane stress (Hill [C.1]) in the presence of either the isotropic Huber-von Mises or Tresca yield conditions in the plastic range. It is well known that for such solids, strong discontinuities in stress and velocity cannot be simultaneously present, and that velocity jumps occur across characteristic surfaces. It has been noted by Hill [C.1] that when a rigid-plastic generalized plane-stress theory is employed in the study of the extension of thin plates, two types of strong discontinuities must be considered. These arise because of the neglect of elastic deformation and the averaged nature of generalized plane stress. A consideration of the second of these factors has led to the mathematical idealisation of the experimentally observed phenomenon of localised necking in thin sheets (Nadai [C.8]).

In a recent paper [C.6], Drugan and Rice investigated strong discontinuities across quasi-statically propagating surfaces in elastic-plastic solids under general three-dimensional conditions when all displacement components are assumed to be continuous. One important conclusion of the work reported in [C.6] is that all stress components are always continuous, a result that follows from certain material stability postulates.

Pan [C.7] has also discussed quasi-statically moving strong discontinuities for elastic-perfectly plastic Huber-von Mises materials under generalized plane stress. He assumes that a strong discontinuity can be replaced by a transition layer of elastic material in which all stress components are assumed to vary continuously. He subsequently argues that all stress components are continuous across propagating surfaces, by using the specific nature of the Huber-von Mises locus and arriving at a contradiction.

In the present work, we reexamine quasi-static discontinuities for the more general case of an anisotropic hardening solid, using an integral form of the maximum plastic work inequality and the usual assumptions in the theory of generalized plane stress (Sec.(C.2)). It is demonstrated in Sec.(C.5) that the use of the maximum plastic work inequality leads to full stress continuity for a broad class of solids, which includes some hardening materials and anisotropic behavior. Pan's assumptions and the limitations of his approach are discussed in Sec.(C.5). A complete analysis of all possible velocity jumps, including sliding discontinuity and localized necks, is carried out in Sec.(C.6) with some generality in constitutive behavior.

C.2. THE GENERALIZED PLANE-STRESS PROBLEM.

Consider an elastic-plastic body occupying an open cylindrical region R of height h (see Fig. C.1). Let the boundary ∂R of the above region be composed of two traction-free planar surfaces S_1 and S_2 and a lateral surface L.

Consider further a fixed orthonormal coordinate system $\{o',\underset{\sim}{e}_1',\underset{\sim}{e}_2',\underset{\sim}{e}_3'\}$ such that $\underset{\sim}{e}_3'$ is parallel to the generators of R.

generalized plane stress conditions require that the height of the cylinder (also referred to later as the thickness of the cylindrical plate) be small as compared with any other dimension of the cylinder, and that the prescribed tractions $\underset{\sim}{t}$ be such that:

$$\underset{\sim}{t} = \underset{\sim}{0} \quad or \quad \sigma_{3i} = 0 \quad on\ S_1 \text{ and } S_2$$

and

$$t_3 = 0, \quad t_\alpha = t_\alpha^*(x_1,x_2)\ on\ L. \tag{C.2.1}$$

Here σ_{ij} are the components of the symmetric Cauchy stress tensor, Greek subscript have the range 1, 2 while Latin subscripts take the values 1, 2, and 3. (This convention will be adopted through the following development.)

In what follows, field quantities such as $\underset{\sim}{\sigma}, \underset{\sim}{\epsilon}$, $\underset{\sim}{u}$, and $\underset{\sim}{v}$ will represent thickness averages of the stress and strain tensors and the displacement and velocity vectors, respectively. It is also assumed that,

$$\sigma_{3i} \equiv 0 \quad on \quad R. \tag{C.2.2}$$

The above assumptions result in solutions of the generalized plane stress problem which, in general, will not satisfy the exact three-dimensional field equations as discussed in detail by Timoshenko and Goodier [C.5] and Hill [C.3]. This is because some of the compatibility equations are not generally satisfied, and errors are involved in using the averaged quantities in the constitutive law and the yield condition. However, if the plate thickness is sufficiently small, the generalized plane stress solution is expected to provide an accurate approximation.

Let Σ be a planar surface, parallel to the x_2'–x_3' plane, dividing the region R in two open subregions R^+ and R^- such that

$$R = R^+ \cup R^- \cup \Sigma.$$

We will define the normal $\underset{\sim}{n}(\overset{\circ}{\underset{\sim}{x}})$ to Σ at a point $\overset{\circ}{\underset{\sim}{x}} \in \Sigma$ as the outward normal of the closed subregion $\bar{R}^-(\bar{R}^{\pm} \equiv R^{\pm} \cup \Sigma)$ at the same point $\overset{\circ}{\underset{\sim}{x}}$.

In what follows, the surface Σ will be viewed as a potential surface of strong discontinuities (discontinuities in stresses and strains) and will be allowed to translate quasi-statically with a normal velocity $V\underset{\sim}{n}$.

Since the approximate theory of generalized plane stress treats the thickness of the plate as vanishingly small, Hill [C.1] points out that every quantity whose gradient is of order (1/h) in a zone of breadth comparable to h *should be modelled as a discontinuity.* Thus, the experimentally observed formation of necks (Nadai [C.8]) in thin plates subjected to tension (rapid variation of thickness of the plate in narrow zones) would be modelled as discontinuities in the out-of-plane displacement component u_3.

The jump in a field quantity $g(\underset{\sim}{x})$, across the surface Σ, will be denoted by:

$$\left.\begin{aligned} &[g] \equiv g^+(\overset{\circ}{\underset{\sim}{x}}) - g^-(\overset{\circ}{\underset{\sim}{x}}) \quad \textit{where} \\ &g^{\pm}(\overset{\circ}{\underset{\sim}{x}}) = \lim_{\epsilon \to 0} g(\overset{\circ}{\underset{\sim}{x}} \pm \epsilon \underset{\sim}{n}(\overset{\circ}{\underset{\sim}{x}})) \quad \overset{\circ}{\underset{\sim}{x}} \in \Sigma \quad \text{and} \quad \epsilon > 0 \end{aligned}\right\}. \tag{C.2.3}$$

C.3. SMOOTHNESS CONSIDERATIONS.

All field quantities will be referred to, with respect to an orthonormal frame $\{O, \underset{\sim}{e}_1, \underset{\sim}{e}_2, \underset{\sim}{e}_3\}$ translating with the surface Σ and such that $O \in \Sigma$, $\underset{\sim}{e}_3 = \underset{\sim}{e}_3'$ and $\underset{\sim}{e}_1 = \underset{\sim}{n}$; see Fig. C.2.

In-plane displacement components u_α are required to have the following smoothness properties:

$$\begin{aligned} &u_\alpha \in C(R) \ \text{ and} \\ &u_\alpha \in C^1(R - \Sigma), \end{aligned} \tag{C.3.1}$$

with the understanding that $\frac{\partial u_\alpha}{\partial x_\beta}$ need not be continuous across Σ. Then, according to the Hadamard compatibility relations [C.2] for jumps in the derivatives of a continuous function,

$$\left[\frac{\partial u_\alpha}{\partial x_\beta} \right] = \lambda_\alpha \, n_\beta \quad on \quad \Sigma, \tag{C.3.2}$$

where λ_α are arbitrary functions of position on Σ. The out-of-plane displacement component u_3 will in general be allowed to suffer a jump across Σ, as discussed in Sec.(C.2). Thus:

$$u_3 \in C^1(R^+) \cap C^1(R^-), \tag{C.3.3}$$

with the understanding that on Σ, u_3 and its gradient need not be defined. On the other hand, $[u_3]$, the jump in the limiting value of u_3 from R^- to R^+, will be assumed to be a continuous and continuously differentiable function of position on Σ.

It is now possible to extend the Hadamard compatibility relations (C.3.2) for the treatment of jumps in the derivatives of discontinuous functions. This extension was first discussed by Thomas [C.4]. The following simpler version was later provided by Hill [C.2],

$$\left[\frac{\partial u_3}{\partial x_i} \right] = \lambda_3 \, n_i + \frac{\partial \phi}{\partial x_i} \quad on \quad \Sigma, \tag{C.3.4}$$

where λ_3 is an arbitrary function of position on Σ and ϕ is an arbitrary continuous function, together with its gradient on Σ and in one neighborhood, say R^+, with the additional restriction that

$$\phi = [u_3] \ \ on \ \ \Sigma.$$

One choice of ϕ in R^+ would be to consider ϕ continued analytically along the normals. Any other choice would merely change λ_3, which is given by

$$\lambda_3 = [\ \underset{\sim}{\nabla} u_3 \cdot \underset{\sim}{n}] - \underset{\sim}{\nabla}\phi \cdot n.$$

Relations (C.3.2) and (C.3.4) allow definition of jumps in the strains across Σ, consistent with the assumptions of the approximate theory of generalized plane stress.

Within the contexts of a small strain formulation,

$$\epsilon_{ij} = \frac{1}{2}(u_{i,j} + u_{j,i}), \tag{C.3.5}$$

and the jumps in the in-plane strain component $\epsilon_{\alpha\beta}$ can be expressed by (C.3.2) as:

$$[\epsilon_{\alpha\beta}] = \frac{1}{2}(\lambda_\alpha n_\beta + \lambda_\beta n_\alpha) \ \ on \ \ \Sigma. \tag{C.3.6}$$

On the other hand, the jump in the out-of-plane strain component ϵ_{33} can be expressed by (C.3.2) and (C.3.4) as:

$$[\epsilon_{33}] = \lambda_3 n_3 + \frac{\partial\phi}{\partial x_3} \ \ on \ \ \Sigma, \tag{C.3.7}$$

where $\phi \in C^1(R^+)$ and $\phi=[u_3]$ on Σ.

C.4. MATERIAL IDEALIZATION.

Within the context of the small-strain flow theory of plasticity, the total strain rate tensor can be decomposed into elastic and plastic parts:

$$\underset{\sim}{\dot{\epsilon}} = \underset{\sim}{\dot{\epsilon}}^e + \underset{\sim}{\dot{\epsilon}}^P \quad on\ R, \tag{C.4.1}$$

where the dot denotes differentiation with respect to time. The elastic strain rate tensor $\underset{\sim}{\dot{\epsilon}}^e$ is related to the stress rate tensor $\underset{\sim}{\dot{\sigma}}$ through a constant, positive definite four-tensor $\underset{\sim}{H}$ (the inverse of the elasticity tensor $\underset{\sim}{C}$). $\underset{\sim}{H}$ is assumed to possess the usual major and minor symmetries. For an anisotropic elastic-plastic solid, $\underset{\sim}{\dot{\epsilon}}^e$ is given by:

$$\underset{\sim}{\dot{\epsilon}}^e = \underset{\sim}{H}\underset{\sim}{\dot{\sigma}} \quad on\ R. \tag{C.4.2}$$

Attention will be focussed on the class of materials obeying Drucker's stability postulate. A particular form of this postulate known as the maximum plastic work inequality can be expressed as:

$$(\underset{\sim}{\sigma} - \underset{\sim}{\sigma}^*) \cdot \underset{\sim}{\dot{\epsilon}}^P \geq 0. \tag{C.4.3}$$

$\forall\ f(\underset{\sim}{\sigma},\bar{\epsilon}^P)=0$, and $f(\underset{\sim}{\sigma}^*,\bar{\epsilon}^P)\leq 0$, where $f(\underset{\sim}{\sigma},\bar{\epsilon}^P)$ is the yield function. An important implication of the above postulate is the normality of the plastic strain rate $\underset{\sim}{\dot{\epsilon}}^P$ to the yield surface leading to a flow rule of the form,

$$\underset{\sim}{\dot{\epsilon}}^P = \dot{\lambda}\underset{\sim}{P}, \tag{C.4.4}$$

where $\dot{\lambda}\geq 0$ and $\underset{\sim}{P} = \nabla_{\underset{\sim}{\sigma}} f$. $\dot{\lambda}$ and $\underset{\sim}{P}$ are scalar valued and symmetric tensor valued functions of $\underset{\sim}{\sigma}$, respectively. In the following section, an integral form of (C.4.3) will be used in conjunction with Equations (C.4.1) and (C.4.2), as well as the compatibility conditions for the jumps in total strains (C.3.6), (C.3.7) to define the jumps in the stresses and the plastic strains produced during the passage of a discontinuity Σ through a material point.

C.5. STRESS CONTINUITY ACROSS THE PROPAGATING SURFACE.

In this section it will be demonstrated that all stress components are continuous across the surface Σ, propagating quasi-statically through the thin plate. It will be shown that this is true even if the out-of-plane displacement u_3 suffers a discontinuity across Σ. *The following proof is based on the maximum plastic work inequality* and the positive definiteness of $\underset{\sim}{H}$. It is an adaptation for plane stress of the proof given by Drugan and Rice [C.6] for the general three-dimensional case. In the present analysis, only the in-plane displacement components u_α are assumed continuous, and the proof is adapted to suit the assumptions of the theory of generalized plane stress. Also, unlike the discussion by Pan [C.7] and consistent with the assumptions of generalized plane stress [C.1], our discussion treats necks as jumps and *not* as narrow transition layers.

If inertia terms are neglected, the balance of linear momentum requires that across the *quasi-statically moving surface* Σ *the traction be continuous. Thus*

$$[\, t_\alpha] = [\sigma_{\alpha\beta}\, n_\beta\,] = 0 \quad on\ \Sigma.$$

With respect to the local orthonormal coordinate frame $\{O,\underset{\sim}{e}_1,\underset{\sim}{e}_2,\underset{\sim}{e}_3\}$ moving with Σ, $n_i=\delta_{1i}$ and the above conditions become:

$$[\sigma_{1\alpha}] = 0 \quad on \quad \Sigma. \qquad \text{(C.5.1)}$$

Equations (C.2.2) and (C.5.1) imply that the only stress component that can suffer a non-trivial jump is σ_{22}. The plastic work W^p accumulated discontinuously at a material point due to the passage of the surface Σ is given by:

$$W^P = \int_{\underset{\sim}{\epsilon}^{P+}}^{\underset{\sim}{\epsilon}^{P}} \underset{\sim}{\sigma} \cdot d\underset{\sim}{\epsilon}^P. \tag{C.5.2}$$

It should be observed here that some error is involved in using the averaged stress and strain quantities of generalized plane stress in the above integral. The above integral is evaluated according to the assumptions of Sec.(C.2). On applying Equation (C.2.2), we find that the plastic work accumulation in (C.5.2) reduces to

$$W^P = \int_{\epsilon_{\alpha\beta}^{P+}}^{\epsilon_{\alpha\beta}^{P-}} \sigma_{\alpha\beta}\, d\, \epsilon_{\alpha\beta}^P. \tag{C.5.3}$$

Using (C.5.1), the above becomes:

$$W^P = -\sigma_{11}[\epsilon_{11}^P] - 2\sigma_{12}[\epsilon_{12}^P] + \int_{\epsilon_{22}^{P+}}^{\epsilon_{22}^{P-}} \sigma_{22} d\, \epsilon_{22}^P. \tag{C.5.4}$$

Also, by using the fact that $n_\beta = \delta_{1\beta}$, (C.3.6) implies that:

$$[\epsilon_{22}] = O \;\; on \;\; \Sigma \;\; or \;\; [\epsilon_{22}^e] = -\,[\epsilon_{22}^P] \;\; on \;\; \Sigma. \tag{C.5.5}$$

By setting $d\underset{\sim}{\epsilon}^P = d\underset{\sim}{\epsilon} - d\underset{\sim}{\epsilon}^e$, using the continuity of ϵ_{22} across Σ (C.5.5) and integrating by parts, (C.5.4) becomes

$$W^P = -\sigma_{11}[\epsilon_{11}^P] - 2\sigma_{12}[\epsilon_{12}^P] - \int_{\epsilon_{22}^{e+}}^{\epsilon_{22}^{e-}} \sigma_{22} d\, \epsilon_{22}^e. \tag{C.5.6}$$

The integral in (C.5.6) can now be evaluated by using equations (C.2.2), (C.5.1), and the constitutive law, to give:

$$\int_{\epsilon_{22}^{e+}}^{\epsilon_{22}^{e}} \sigma_{22} d\epsilon_{22}^{e} = -\frac{1}{2} H_{2222}(\sigma_{22}^{+} + \sigma_{22}^{-})[\sigma_{22}]. \tag{C.5.7}$$

In addition, from (C.2.2), (C.5.1), and (C.5.5),

$$[\epsilon_{22}^{P}] = -[\epsilon_{22}^{e}] = -H_{2222}[\sigma_{22}] \quad on\ \Sigma. \tag{C.5.8}$$

Thus, Equations (C.5.6) and (C.5.7) give:

$$W^{P} = -\sigma_{11}[\epsilon_{11}^{P}] - 2\sigma_{12}[\epsilon_{12}^{P}] - \frac{1}{2}(\sigma_{22}^{+} + \sigma_{22}^{-})\,[\epsilon_{22}^{P}]$$

or,

$$W^{P} = -\frac{1}{2}\,(\sigma_{ij}^{+} + \sigma_{ij}^{-})\,[\epsilon_{ij}^{P}]. \tag{C.5.9}$$

It should be observed that the restrictions imposed on the path in stress space in the evaluation of the integral in (C.5.6) are the plane stress conditions and the continuity of tractions across Σ. This effectively implies a straight line path in stress space from σ_{22}^{+} to σ_{22}^{-}.

The integral form of the plastic work inequality (C.4.3) can now be used by setting $\underset{\sim}{\sigma}^{*}=\underset{\sim}{\sigma}^{+}$ where $f(\underset{\sim}{\sigma}^{+},\bar{\epsilon}^{P}) \leq 0$. Thus, $\underset{\sim}{\sigma}^{+}$ is constrained to remain always at or inside the yield surface during passage of Σ. Thus, by our using (C.2.2), (C.5.1), and (C.5.9):

$$\int_{\epsilon_{ij}^{P+}}^{\epsilon_{ij}^{P-}} (\sigma_{ij} - \sigma_{ij}^{+}) d\epsilon_{ij}^{P} = -\frac{1}{2}\,(\sigma_{22}^{+} + \sigma_{22}^{-})[\epsilon_{22}^{P}] + \sigma_{22}^{+}[\epsilon_{22}^{P}] \geq 0$$

which, by (C.5.8), gives

$$\frac{1}{2}\,[\sigma_{22}]\,[\epsilon^{e}_{22}] \leq 0 \quad or \quad \frac{1}{2}\,([\sigma_{22}])^2\, H_{2222} \leq 0. \tag{C.5.10}$$

(C.5.10) now requires that $[\sigma_{22}] = 0$, since $H_{2222} > 0$.

Remarks

The following remarks are relevant:

1. Under generalized plane stress conditions, all stress components are continuous across the slowly propagating surface Σ, even if the out of plane displacement u_3 suffers a discontinuity.

2. The present discussion applies to general anisotropic elastic-plastic hardening solids obeying a flow rule of the associated type. The proof of full stress continuity is based on an integral form of the maximum plastic work inequality and the positive definiteness of the elastic potential.

3. An earlier discussion by Pan [C.7] is limited to elastic- ideally plastic solids of a Huber-von Mises type under generalized plane stress conditions. His argument, which does not make use of the maximum plastic work inequality, follows from Hill's [C.3] statement that the stress state from σ^{+}_{22} to σ^{-}_{22} can be bridged only by a succession of elastic states. This assumes a smooth variation of stresses in a "transition layer." Such an assumption is questionable for generalized plane stress since, as pointed out in Sec.(C.2), any field quantity whose gradient is $O(\frac{1}{h})$ in a zone of breadth comparable to h should be modelled as a discontinuity. Even if this assumption is accepted, Pan's argument clearly does not apply to arbitrary yield surfaces or general hardening solids. For instance, in elastic-perfectly plastic solids characterized by a Tresca yield condition when the neck (discontinuity in u_3) coincides with a principal stress direction and

$\sigma_{11} = \pm \sigma_o$, the stress component σ_{22} can have *any* value between 0 and $\pm \sigma_o$ and still lie on the yield surface (Hill [C.3]). Hence, $\dot{\lambda}$ in equation (C.4.4) is not necessarily zero in the transition from $\underset{\sim}{\sigma}^+$ to $\underset{\sim}{\sigma}^-$ (Hill [C.1]), and the argument fails. Also, for any type of hardening solid, the consistency condition requires the stress state to lie on the yield surface during the process from $\underset{\sim}{\sigma}^+$ to $\underset{\sim}{\sigma}^-$ and no elastic unloading is possible.

C.6. DISCONTINUITIES IN STRAINS AND VELOCITIES.

In this section, the earlier result pertaining to continuity of stresses across Σ will be used to provide restrictions on the nature of admissible jumps in strains and material particle velocities across Σ for a general anisotropic hardening solid. Attention will then be turned to plastically incompressible, generally anisotropic, elastic-perfectly plastic solids with smooth but otherwise arbitrary yield surfaces. Specialized results will be given for Huber-von Mises solids at the end of the discussion.

General Considerations:

The jumps in the in-plane velocity component v_α are given ([C.2], [C.6]) by:

$$[v_\alpha] = -V \left[\frac{\partial u_\alpha}{\partial x_1} \right] \; on \; \Sigma, \tag{C.6.1}$$

where $V\underset{\sim}{n}$ is the normal velocity of Σ. Making use of (C.3.2) and (C.3.6) the velocity jumps may be expressed as:

$$\begin{array}{l} [v_1] = -V[\epsilon_{11}] \\ [v_2] = -2V[\epsilon_{12}] \end{array} \; on \;\; \Sigma. \tag{C.6.2}$$

Full stress continuity and (C.4.2) require the elastic part of the strains to be continuous across Σ,

$$[\epsilon^e_{ij}] = 0 \quad on \quad \Sigma. \tag{C.6.3}$$

The above, and Equation (C.5.8), therefore imply

$$[\epsilon^p_{22}] = 0 \quad on \ \Sigma. \tag{C.6.4}$$

As a result, the expression for the positive plastic work accumulation in (C.5.9) becomes

$$W^p = -\sigma_{11}[\epsilon^p_{11}] - 2\sigma_{12}[\epsilon^p_{12}] \geq 0, \tag{C.6.5}$$

and the jumps in the velocity components v_1 and v_2 are given by:

$$\left.\begin{aligned} [v_1] &= -V\,[\epsilon^p_{11}] \\ [v_2] &= -2V\,[\epsilon^p_{12}] \end{aligned}\right. \quad on \ \ \Sigma. \tag{C.6.6}$$

The plastic work W^p can now be expressed in terms of velocity jumps as follows:

$$W^p = \frac{1}{V}(\sigma_{11}[v_1] + \sigma_{12}[v_2]) \geq 0. \tag{C.6.7}$$

No specific restrictions on the constitutive model other than the general assumptions made in Sec.(C.4) have been imposed in the derivation of Equations (C.6.1)-(C.6.7).

For the specific class of plastically incompressible solids:

$$[\epsilon^p_{33}] = -[\epsilon^p_{11}] - [\epsilon^p_{22}] \quad on \ \Sigma, \tag{C.6.8}$$

which, by use of Equation (C.6.4) simplifies to:

$$[\epsilon^P_{33}] = -[\epsilon^P_{11}] \quad on\ \Sigma. \tag{C.6.9}$$

Equation (C.6.9) serves to determine the jump in the out-of-plane plastic strain component ϵ^P_{33} in terms of the jump in the in-plane plastic strain component ϵ^P_{11} for plastically incompressible solids.

If the displacement component u_3 happens to be continuous across Σ as in [C.6], then ϵ_{33} and hence ϵ^P_{33} would also be continuous. Equations (C.6.8) and (C.6.6) will then imply that ϵ^P_{11} and v_1 should also be continuous across Σ. Thus, it follows that for a plastically incompressible solid, when the surface Σ does not coincide with a neck (jump in u_3), only a sliding velocity discontinuity (jump in v_2) is permissible.

Elastic-Perfectly Plastic Solid

For such solids, the yield surface is represented by

$$f(\underset{\sim}{\sigma}) = 0 \quad on\ \ R, \tag{C.6.10}$$

where $f(\underset{\sim}{\sigma})$ depends symmetrically on $\underset{\sim}{\sigma}$ and $\underset{\sim}{\sigma}^T$. It will also be assumed here that the yield surface is smooth (has a continuous normal).

Under such circumstances the flow rule takes the following form:

$$\dot{\underset{\sim}{\epsilon}}^P = \dot{\lambda}\ \underset{\sim}{P} \quad on\ R, \tag{C.6.11}$$

where $\dot{\lambda} \geq 0$ is an undetermined scalar function of position, and

$$\underset{\sim}{P}(\underset{\sim}{\sigma}) \equiv \nabla_{\underset{\sim}{\sigma}}\ f(\underset{\sim}{\sigma}) \quad on\ R \tag{C.6.12}$$

is a symmetric tensor-valued function of $\underset{\sim}{\sigma}$. Under conditions of generalized plane stress, Equations (C.6.10) and (C.6.12) should be used in conjunction with the constraint (C.2.2). Inside regions that are currently deforming plastically, it can be shown from the two in-plane equilibrium equations, the yield condition and the plane stress assumption (C.2.2) that along stress characteristic directions the direct components of $P_{\alpha\beta}$ should vanish (Hill [C.3]).

It is also clear that, P_{ij} should be continuous across Σ from assumed smoothness of the yield surface and the requirement of full stress continuity. Then, from (C.6.11) the jumps in the plastic strain component ϵ_{ij}^{P} becomes

$$[\epsilon_{ij}^{P}] = -\,\eta\, P_{ij} \text{ on } \Sigma, \qquad \text{(C.6.13)}$$

where $\eta = \int_{\lambda^{+}}^{\lambda^{-}} d\lambda \geq 0$ is an undetermined scalar function of position on Σ.

Since $[\epsilon_{22}^{P}] = 0$ across Σ, Equation (C.6.13) implies that either $\eta=0$ or $P_{22}=0$ or both. If $\eta=0$, (C.6.13) requires all strain components to be continuous. Thus, the *necessary* condition for non-trivial jumps in strains to exist across Σ is that P_{22} should vanish on Σ. In other words, Σ *should coincide with a stress characteristic direction of its plastic side.*

This condition is less restrictive than the necessary condition for non-trivial jumps in the plastic strain components derived by Drugan and Rice [C.6] when *all* displacements were continuous across Σ. The corresponding necessary condition derived in [C.6] states that $P_{22}=P_{33}=P_{23}=0$ on Σ.

From the above, the following important observation can be made:

Consider at least one side of Σ (which coincides with a neck, say R^{+}) to be currently deforming plastically. If in addition, Σ coincides with one of the stress characteristic directions, say direction A (see Fig. C.3), then the velocity component along the other characteristic direction B, is continuous across Σ. Thus,

$$[V_B] = 0 \quad on\ \Sigma. \tag{C.6.14}$$

The above result follows by first observing that since Σ coincides with a stress characteristic direction, P_{22} vanishes on Σ. Also, if the other characteristic direction makes an angle δ ($\delta \neq \pm\frac{\pi}{2}$) with the x_1 axis, then by the fact that $P_{BB}=0$ and the transformation relation, we have

$$\tan\delta = -\frac{P_{11}}{2P_{12}} \quad \text{for} \quad P_{12} \neq 0. \tag{C.6.15}$$

In addition, combining (C.6.6) and (C.6.13) and noting that $P_{12}\neq 0$, we see that the following is true:

$$[v_1] = \frac{P_{11}}{2P_{12}}[v_2] \quad on\ \Sigma. \tag{C.6.16}$$

The velocity jump $[v_B]$ along the other characteristic direction will be given by:

$$[v_B] = \cos\delta([v_1] + [v_2]\tan\delta), \quad \delta \neq \pm\frac{\pi}{2},$$

which vanishes by use of (C.6.15) and (C.6.16). This general result was also noted by Pan [C.7] for the special case of an isotropic Huber-von Mises solid and it also holds for stationary necks in a rigid-plastic solid (Hill [C.1]).

If in addition $P_{12}=0$, both the stress characteristics merge along Σ ($\delta=\pm\frac{\pi}{2}$) and as a result Σ becomes a "parabolic line." Equations (C.6.6) and (C.6.13) then imply that if $P_{12}=0$,

$$[v_2] = 0 \quad on \ \Sigma . \tag{C.6.17}$$

Thus, when Σ coincides with a "parabolic line," the tangential velocity is continuous and *only* the normal velocity has a jump.

When Σ coincides with a neck and the two characteristic directions do not merge along Σ (see Fig. C.3), then the accumulation of plastic work (C.6.7) due to the passage of Σ becomes:

$$W^P = \frac{1}{V} \left(\frac{\sigma_{11}P_{11} + 2\sigma_{12}P_{12}}{2P_{12}}\right) [v_2] \geq 0 . \tag{C.6.18}$$

Also, the fact that $\sigma_{ij}\dot{\epsilon}_{ij}^{P} \geq 0$ implies that

$$\sigma_{ij} \ P_{ij} \geq 0 . \tag{C.6.19}$$

By (C.2.2) and $P_{22}=0$ along Σ, (C.6.19) becomes:

$$\sigma_{11}P_{11} + 2\sigma_{12}P_{12} \geq 0 . \tag{C.6.20}$$

Inequalities (C.6.18) and (C.6.20) result in

$$\frac{1}{V} \frac{[v_2]}{2P_{12}} \geq 0, \qquad P_{12} \neq 0 . \tag{C.6.21}$$

When the two characteristics merge along Σ ($\delta=\pm\frac{\pi}{2}$ and $P_{22}=P_{12}=0$), it follows from (C.6.7) and (C.6.17) that

$$\frac{\sigma_{11}}{V}\,[v_1] \geq 0. \qquad \text{(C.6.22)}$$

Isotropic Huber-von Mises solids

The above results can now be specialized for an isotropic elastic-perfectly plastic solid that obeys the Huber-von Mises yield condition. For such a solid, the yield condition states

$$f(\underset{\sim}{\sigma}) = \frac{1}{2}\,\underset{\sim}{S}\cdot\underset{\sim}{S} - \tau_o^2 = 0 \quad on\ R, \qquad \text{(C.6.23)}$$

where $\underset{\sim}{S} \equiv \underset{\sim}{\sigma} - \frac{1}{3}\,tr\underset{\sim}{\sigma}\underset{\sim}{1}$ is the deviatoric stress tensor and τ_o is the yield stress in pure shear. For such a solid,

$$\underset{\sim}{P}(\underset{\sim}{\sigma}) = \nabla_{\underset{\sim}{\sigma}}\, f(\underset{\sim}{\sigma}) = \underset{\sim}{S} \quad on\ R. \qquad \text{(C.6.24)}$$

All the results and corresponding remarks from (C.6.3)-(C.6.22) hold for this solid with $\underset{\sim}{P}$ replaced by $\underset{\sim}{S}$. In particular, (C.6.16) takes the form (Pan [C.7]):

$$[v_1] = \frac{S_{11}}{2S_{12}}\,[v_2] \quad \text{if} \quad S_{12} \neq 0, \qquad \text{(C.6.25)}$$

and (C.6.18) reduces to

$$W^r = \frac{1}{V}\left(\frac{\tau_o^2}{\sigma_{12}}\right)[v_2] \geq 0. \qquad \text{(C.6.26)}$$

Summary of Results

The results of Sec.(C.6) can now be summarized as follows:

a. For a general anisotropic hardening solid that is also plastically incompressible, the following is true: When the propagating surface Σ does *not* coincide with a neck (full displacement continuity), only a jump in the tangential velocity component (sliding discontinuity) is admissible.

b. If, however, the solid is perfectly plastic, Σ coincides with one characteristic direction ($P_{22}=0$). In addition, full displacement continuity together with plastic incompressibility also give $P_{33}=P_{11}=0$. This states that the direction normal to Σ is *also* a characteristic direction. Unlike plane strain, this occurs under plane stress condition only under exceptional circumstances (Hill [C.3]). In particular, for Huber-von Mises solids this is true when the surface coincides with a plane of maximum shear stress, and the latter is equal in magnitude to the yield stress in pure shear.

c. For a general anisotropic elastic-perfectly plastic solid, when a surface *coincides* with a neck (discontinuity in u_3), both tangential and normal velocities have jumps. This requires that the neck should lie along one characteristic direction. Then the component of the velocity along the other characteristic direction (not generally perpendicular to Σ) is continuous (see Equation (C.6.14)). Thus, necks cannot form if the plastically deforming side of the surface is in an elliptic state of stress.

d. For an elastic perfectly plastic solid, if in addition to (c), $P_{12}=0$, both the characteristics merge along the neck, and this results in a parabolic stress state. Then, the tangential velocity is continuous and *only the normal velocity has a jump.* For the special case of a Huber-von Mises solid, $P_{12}=S_{12}=0$, and the characteristic surface coincides with a principal stress direction.

C.7. REMARKS AND APPLICATIONS.

The jump conditions discussed here have some relevance to the stress and strain fields near the tip of a quasi-statically growing crack in an elastic-plastic solid under generalized plane stress conditions. For instance, in the elastic-perfectly plastic Huber-von Mises material (Rice [C.9]) a "constant stress" (asymptotic) plastic sector cannot occur directly behind a "centered fan" plastic sector because the condition for positive plastic work accumulation (C.6.21) will be violated at the interface. This renders the asymptotic solution for the plane stress stationary crack by Hutchinson [C.10] unacceptable when the crack begins to grow. From the preliminary asymptotic analysis by Rice [C.9], it then follows that only an "elastic unloading" sector can occur behind the centered fan. Hutchinson's stationary crack solution also has a jump in the in-plane stress component between two constant stress sectors. This is also inadmissible when the crack begins to propagate.

No solution for this problem, which satisfies all the conditions set forth in the present work, has yet been constructed. An open question that arises, for which detailed experimental and numerical studies may provide an answer, is whether necking occurs near the growing crack tip. Otherwise, except in special circumstances (e.g., a fan angle of 90°), no strong discontinuities near the growing crack tip can be admitted. In view of the fact that the (fully yielded) stationary crack tip solution [C.10] has a strong discontinuity, one wonders whether the condition of full continuity in both stress and velocity near the propagating crack tip may be too restrictive to satisfy.

C.8. APPENDIX REFERENCES.

C.1. Hill, R. (1952), "On Discontinuous Plastic States with Special Reference to Localized Necking in Thin Sheets," *Journal of Mechanics and Physics of Solids*, Vol. 1, 19-30.

C.2. Hill, R. (1961), "Discontinuity Relations in Mechanics of Solids," in: *Progress in Solid Mechanics* I.N. Sneddon and R. Hill eds., Vol. 2, Ch. 6, pp. 247-276.

C.3. Hill, R. (1983), *The Mathematical Theory of Plasticity,* Clarendon Press, Oxford, Paperback

C.4. Thomas, T.Y., "Extended Compatibility Relations for Study of Surfaces of Discontinuity in Continuum Mechanics," *Journal of Mathematics and Mechanics,* Vol. 6, 311-322.

C.5. Timoshenko, S.P. and Goodier, G.N. (1983), *Theory of Elasticity,* McGraw Hill, p. 31, p. 274.

C.6. Drugan, W.J. and Rice, J.R. (1984), "Restrictions on Quasi-statically Moving Surfaces of Strong Discontinuity in Elastic-Plastic Solids," in *Mechanics of Material Behavior,* G.J. Dvorak and R.T. Shield eds., Elsevier, Amsterdam pp. 59-73.

C.7. Pan, H. (1982), "Some Discussion on Moving Strong Discontinuity under Plane Stress Conditions," *Mech. of Materials,* Vol. 1, 325-329.

C.8. Nadai, A. (1950), *Theory of Flow and Fracture in Solids,* McGraw-Hill, Vol. 1 pp. 319-320.

C.9. Rice, J.R. (1982), "Elastic-Plastic Crack Growth," in: *Mechanics of Solids,* H.G. Hopkins and M.J. Sewell eds., Pergamon Press, Oxford, pp. 539-562.

C.10. Hutchinson, J.W. (1968), "Plastic Stress and Strain Fields at a Cracktip," *Journal of Mechanics and Physics of Solids,* Vol. 16, 337-347.

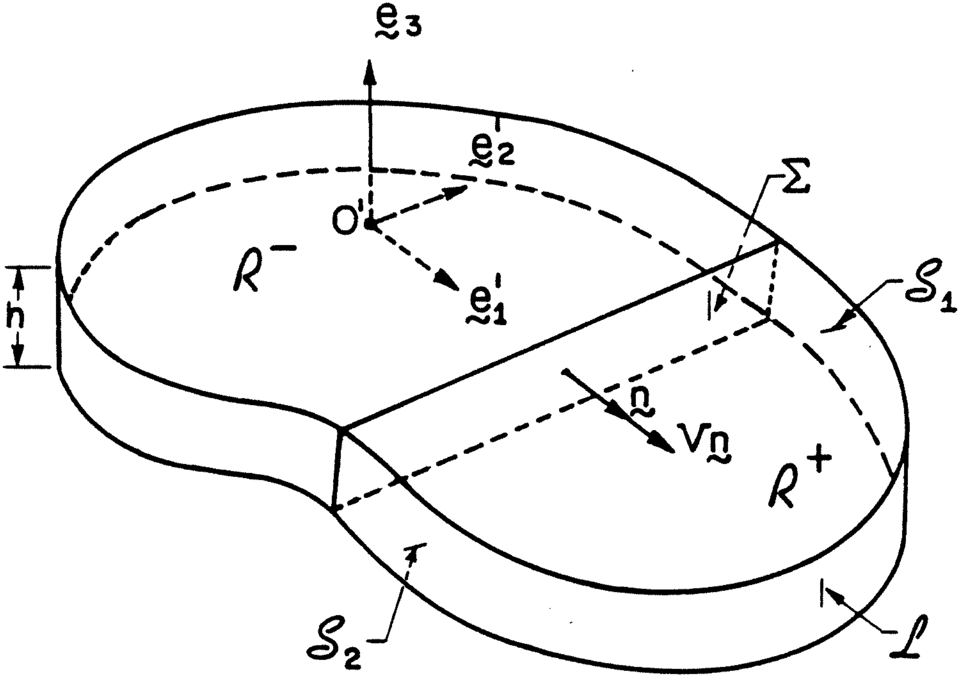

Figure C.1. *Elastic-Plastic body with discontinuity surface* Σ.

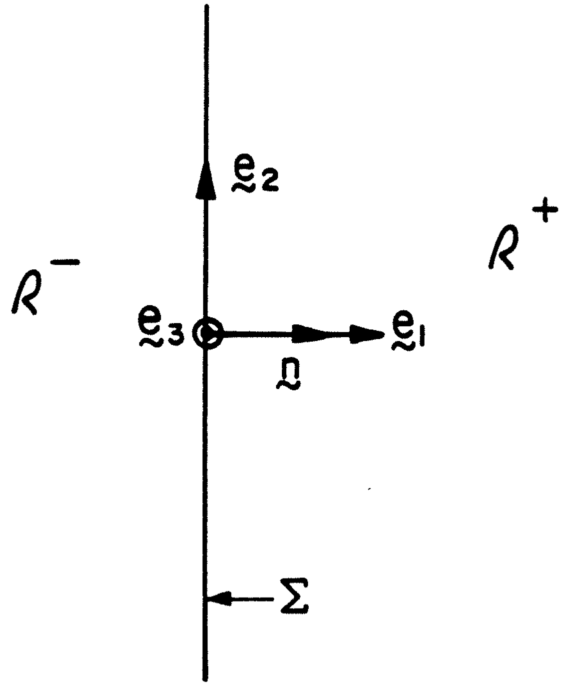

Figure C.2. *Local coordinate system translating with the surface.*

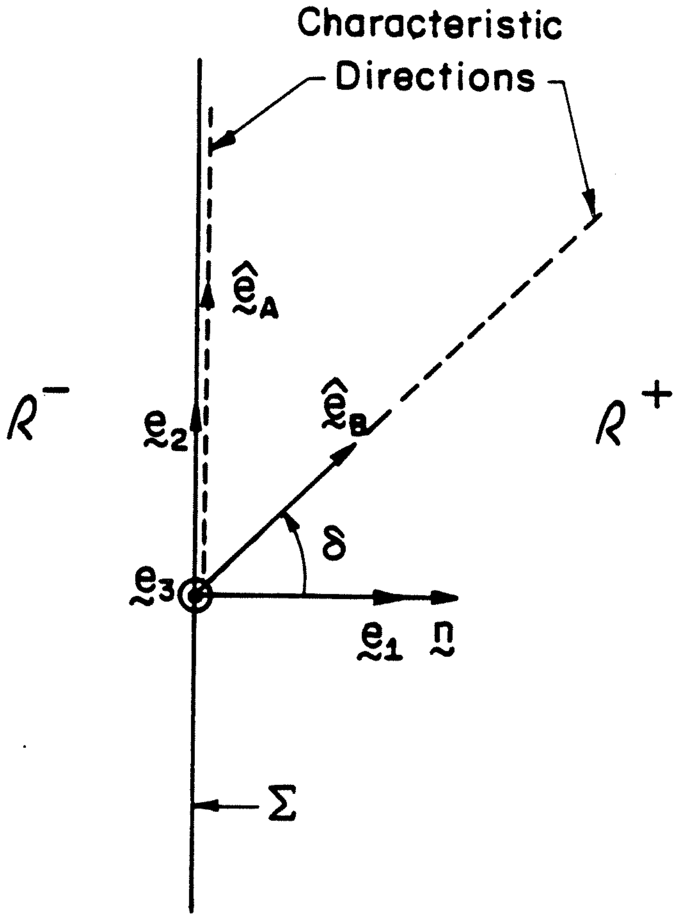

Figure C.3. *Moving discontinuity surface and characteristic directions of the plastically deforming side.*